# Surface plasmon propagation in metal nanowires

Mingxia Song

## To cite this version:

Mingxia Song. Surface plasmon propagation in metal nanowires. Other [cond-mat.other]. Université de Bourgogne, 2012. English. NNT : 2012DIJOS053 . tel-00842236

HAL Id: tel-00842236
https://theses.hal.science/tel-00842236

Submitted on 8 Jul 2013

Université de Bourgogne

Faculté des Sciences

Laboratoire Interdisciplinaire Carnot de Bourgogne

Département Nanosciences

# Surface plasmon propagation in metal nanowires

Thèse présentée à l'Université de Bourgogne pour obtenir
le grade de Docteur (Mention Physique)

par

SONG Mingxia

Soutenue le 13 Novembre 2012 devant la commission d'examen composée de :

| | | | |
|---|---|---|---|
| BERNAL | M.P | Directeur de recherche CNRS, Univ. Franche-Comté | Président |
| PLAIN | J. | Professeur, Univ. de Technologie de Troyes | Rapporteur |
| PEYRADE | D. | Chargé de recherche CNRS, Univ. Grenoble | Rapporteur |
| SAVIOT | L. | Directeur de recherche CNRS, Univ. Bourgogne | Examinateur |
| MARGUERITAT | J. | Chargé de recherche CNRS, Univ. Lyon 1 | Examinateur |
| BOUHELIER | A. | Chargé de recherche CNRS, Univ. Bourgogne | Directeur de thèse |

# Acknowledgement

This thesis and all the research I have done in the past three years could not be done without the help of several individuals.

First of all, I would like to thank my advisor Alexandre Bouhelier who gave me the chance to come to the lab and stimulated my interest in physics. He taught me how to think and instilled in me lots of helpful ideas which guide my research during the three years. He has always shown great enthusiasm for my research and patiently helped me whenever I have problems. He always believed in me and gave me a lot of chance to practice even though I always made things complicate. He guided me and helped me to go through countless difficulties I encountered during my research. I am also thankful for his great help for my living in France.

A special thank goes to Gérard Colas des Francs. He helped me to solve all the theoretical calculation problems that I do not understand during analysing my results and spent a lot of time discussing with me. I express my gratitude to Jean-Claude Weeber for discussing with me about the problems I had during my experiment. I would like to thank Juan-Miguel Arocas and Laurent Markey for their help in solving the technical problems.

I am grateful to Johann Berthelot who always helped me during my research especially for his help on the fabrication of my sample. He has helped me to fix out many software problems. I thank him for spending much time to help me even when he was writing his thesis. I also think Caijin Huang who gave me lots of suggestions when I first came to France. I would like to thank Jérémie Margueritat, Rai Padmnabh, Arnaud Stolz for discussing with me and providing me some helpful ideas. I express my gratitude to Stéphane Derom, Karim Hassan, Thomas Bernardin, Simon Debrand, Serkan Kaya, Antonin Ollagnier and Thibault Brule. They have given me wonderful time during the three years. I will never forget the time we worked together.

A warm thank goes to Elly Lacroute for all the administrative tasks. I appreciate Alain Dereux, Eric Finot and everyone who I worked together with in the group. Without your support, I wouldn't be able to finish my research.

I also thank Erik Dujardin, Jadab Sharma and Aniket Thete from CEMES, Toulouse, France and Douguo Zhang from University of Science and Technology of China for nanowires synthesis.

Many thanks to all of my friends who generously gave their concern and support to me. Finally, I express my gratitude particularly to my family. Their support were always with me during the three years.

# Abstract

Plasmonic circuitry is considered as a promising solution-effective technology for miniaturizing and integrating the next generation of optical nano-devices. The realization of a practical plasmonic circuitry strongly depends on the complete understanding of the propagation properties of two key elements: surface plasmons and electrons. The critical part constituting the plasmonic circuitry is a waveguide which can sustain the two information-carriers simultaneously. Therefore, we present in this thesis the investigations on the propagation of surface plasmons and the co-propagation of surface plasmons and electrons in single crystalline metal nanowires. This thesis is therefore divided into two parts.

In the first part, we investigate surface plasmons propagating in individual thick penta-twinned crystalline silver nanowires using dual-plane leakage radiation microscopy. The effective index and the losses of the mode are determined by measuring the wave vector content of the light emitted in the substrate. Surface plasmon mode is determined by numerical simulations and an analogy is drawn with molecular orbitals compound with similar symmetry. Leaky and bound modes selected by polarization inhomogeneity are demonstrated. We further investigate the effect of wire geometry (length, diameter) on the effective index and propagation losses.

On the basis of the results obtained during the first part, we further investigate the effect of an electron flow on surface plasmon properties. We investigate to what extend surface plasmons and current-carrying electrons interfere in such a shared circuitry. By synchronously recording surface plasmons and electrical output characteristics of single crystalline silver and gold nanowires, we determine the limiting factors hindering the co-propagation of electrical current and surface plasmons in these nanoscale circuits. Analysis of wave vector distributions in Fourier images indicates that the effect of current flow on surface plasmons propagation is reflected by the morphological change during the electromigration process. We further investigate the possible crosstalk between co-propagating electrons and surface plasmons by applying alternating current bias.

**Key words:** Plasmonic circuitry, Surface plasmon, Pentagonal single crystalline nanowire, Effective index, Propagation length, Wave vector, Leaky radiation microscopy, Contacted nanowire, Co-propagation, Electrical failure, Bias modulation, SEM contamination.

# Contents

# Chapter 1

# Introduction

## 1.1 Introductory words about Plasmonics

In this information expansion era, faster information transport and larger information capacity ask for a higher miniaturization and large scale integration of functional devices. Thanks to the development of dedicated fabrication tools, nanoscale electronic devices with critical dimensions are approaching 10 nm length scale. Although great progresses have been made on the dimension of on-chip elements, current electric devices are approaching their fundamental speed and bandwidth limit that cannot keep up with the ever-increasing consumer demand [1, 2]. Using light as the information carrier instead of electrons is believed to be the most promising solution to this problem. Photonic components can be much faster than their electronic counterpart. Photonic crystals have been extensively studied for their ability to control and manipulate photons [3, 4]. Electro-optically tunable photonic crystals show potential applications in modulation and switching in photonic information technology [5, 6, 7, 8, 9]. Optical fibres for instance are routinely used to transmit information with modulation speed well above 40 GHz. Optical components however, are notoriously difficult to scale down due to the diffraction barrier restricting dimensions to half of the effective wavelength [10, 11, 12, 13]. Although information can be transferred at the speed of light, the dimension of integrated photonic components remains orders of magnitude larger than electronic devices. Figure 1.1 shows a graph of operating speed of devices versus their critical dimensions for different technologies extracted from Ref. [2]. The trade off between speed brought by photonic components and the size of typical electronic systems can be mitigated by a paradigm technology called *plasmonics*.

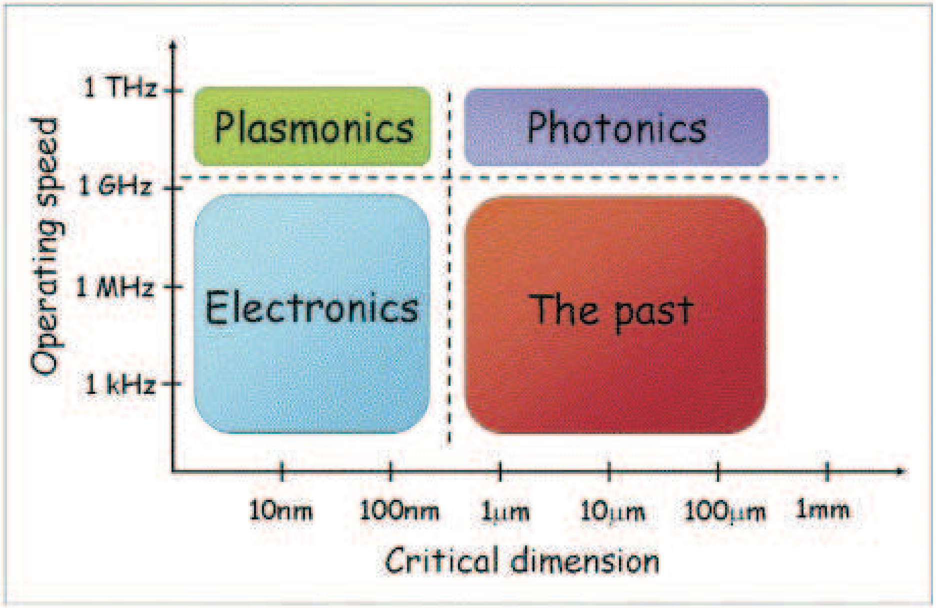

Fig 1.1: Comparison of operating speeds and critical dimensions of different chip-scale device technologies. Image extracted from Ref. [2].

Plasmonics is a technology aiming at engineering material surfaces to control surface plasmons. Surface plasmons are collective electron oscillations that exist at the interface between a dielectric medium and a conductor [14]. When surface plasmons are coupled to photons, they can create electromagnetic waves which propagate along the interface known as surface plasmon-polaritons (SPPs) [15]. The electromagnetic field of SPPs is schematically depicted in Fig. 1.2. The field is highly confined to the near vicinity of the dielectric and metal interface and decays exponentially in the directions perpendicular to the interface [16]. Following the pioneering work of R.H. Ritchie in 1957 [17], the unique properties of surface plasmon polaritons were extensively studied [14, 18, 19, 20, 21]. Especially, as the development and improvement of nanotechnology, the emergence of ”plasmonics” shows tantalizing prospects in optical interconnects [22, 23, 24, 25, 26], data storage [27, 28], field-enhanced spectroscopy [29, 30, 31, 32, 33, 34], microscopy [35, 36], sensors [37, 38, 39], and solar cells [40, 41].

As a subfield of nanophotonics, plasmonics was first put forward in 1999 [42] as an effective mean to route and manipulate light at nanometer length scale exploiting the unique optical properties of metal nano-structures [43, 44]. This combination of SPPs and metal nano-structures enables SPP-based optical components to sustain and guide light signals beyond the limitation imposed by the diffraction barrier. By taking the advantages

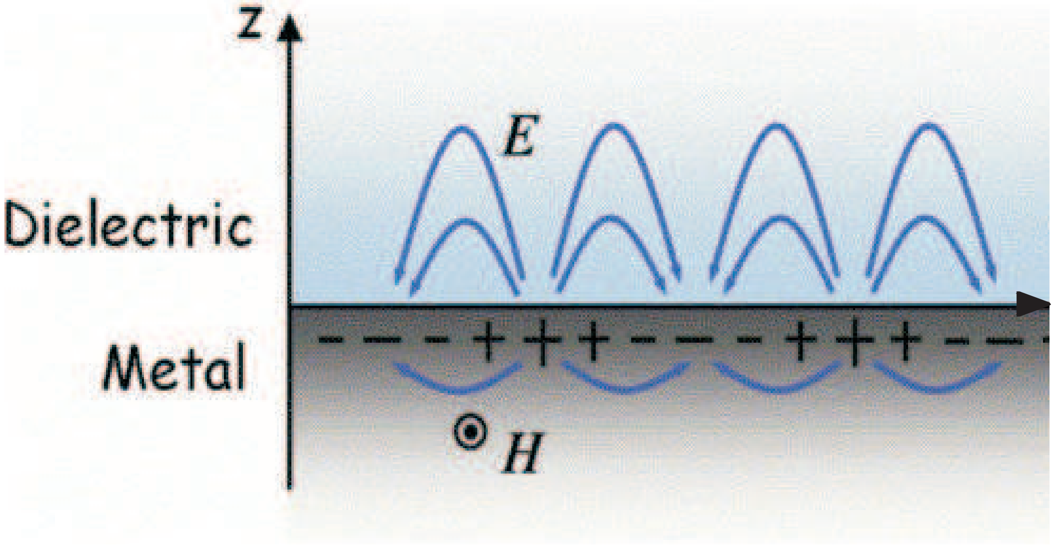

Fig 1.2: Electric field and magnetic field distribution associated with SPPs propagating along the metal and dielectric interface. The electromagnetic field decays exponentially perpendicular to the interface. Image extracted from Ref. [2].

of the polaritonic nature of the plasmon (electrons $\mapsto$ confinement and photons $\mapsto$ speed), SPP-based devices can be drastically miniaturized compared to standard photonic devices. They can sustain a high operating speed surpassing modern electronics thus offering a paradigm shift for the next generation of on-chip technology.

A functional platform would take the form of a complete miniature plasmonic circuitry with both optical and electrical signals being carried without interference [24]. To realize such a circuit, several SPP-based optical components are required: waveguides [45, 46], switches [47], couplers [48] and so on. Surface plasmon waveguides concentrating and guiding light in structures smaller than the diffraction limit are the nanoscale analogue to conventional dielectric fibre and have played a central role among the different plasmonic passive and active elements that were developed so far [11].

## 1.2 SPP propagation in metal waveguide

Various nano-structures have been exploited to confine and propagate SPPs such as thin metal films [49, 50, 51], micrometer-wide stripes [52, 53, 54], nanowires [45, 55, 56], chains or arrays of nanoparticles [11, 57, 58, 59], nanoholes [60, 61], nanogaps [62, 63, 64], nanogrooves and wedges [65, 66], hybrid waveguides [26, 67] and so on. The propagation of surface plasmons was first studied in thin metal films. With the development of scanning near-field optical microscopy, it was soon realized that the propagation of SPPs in thin films was affected by structural defects present at the film surface [68, 69, 70]. Artificially creating these defects at the surface opened the door to what was called "plasmon optics": manipulating a surface plasmon beam very much like standard optical elements are shaping a laser beam.

Spreading of the surface plasmon in the film naturally occurs in both in-plane directions with an extent that depends on the type of excitation, but also on the quality of the film [71]. In order to confine the SPP mode in one direction, the film width was reduced laterally to form stripe metal waveguides. Propagation of the SPP is restricted to the stripe since it does not exist outside the metal. Mode formation in stripes is understood as total internal reflection of the SPP [72] and edge interaction [51]. Stripe waveguides are however suffering from a strong limitation detrimental for realizing dense plasmonic network. As the width of the stripe is reduced to increase lateral confinement, the SPP mode runs into a cutoff and becomes leaky for width $<2$ to 3 $\mu$m [73].

Benefiting from near-field coupling and well defined dipolar surface plasmon resonances [22], Stefan Maier and his co-workers used chains of nanoparticles to increase SPP confinement and overcome the cutoff limit of stripe waveguide [73]. An example of an array of such discrete structures is illustrated in Fig. 1.3(a). However, ohmic and scattering losses are dominant in nanoparticles and the propagation was restricted to a few hundred nanometers [59]. Other plasmon waveguides such as nanoholes (Fig. 1.3(b)), nanogrooves (Fig. 1.3(c)) and nanogaps (Fig. 1.3(d)) can also provide strong localization mechanisms while limiting extrinsic losses such as scattering. Like any other plasmonic waveguides, these approaches are plagued by the trade-off existing between the waveguide size and propagation loss. Because metals at optical or near-infrared wavelengths have a field skin depth comparable to the thickness of the structure, confined modes are associated with large intrinsic losses. The propagation distance is therefore reduced compared to modes spreading more outside the metal. An hybrid waveguide consisting of a silicon waveguide and a silver nanowire [74] in Fig. 1.3(e) was proposed as a solution for this trade-off. These waveguides are usually designed for longer wavelength.

Compared to the available plasmon waveguides, metal nanowires are capable of supporting SPPs propagating along one direction while localizing SPPs in the other two. Unlike metal films and metal stripes, there is no cutoff for the fundamental mode in metal nanowires. Furthermore, the single-crystal nature of chemically synthesized metal nanowires mitigates propagation losses. A good trade-off can thus be obtained between

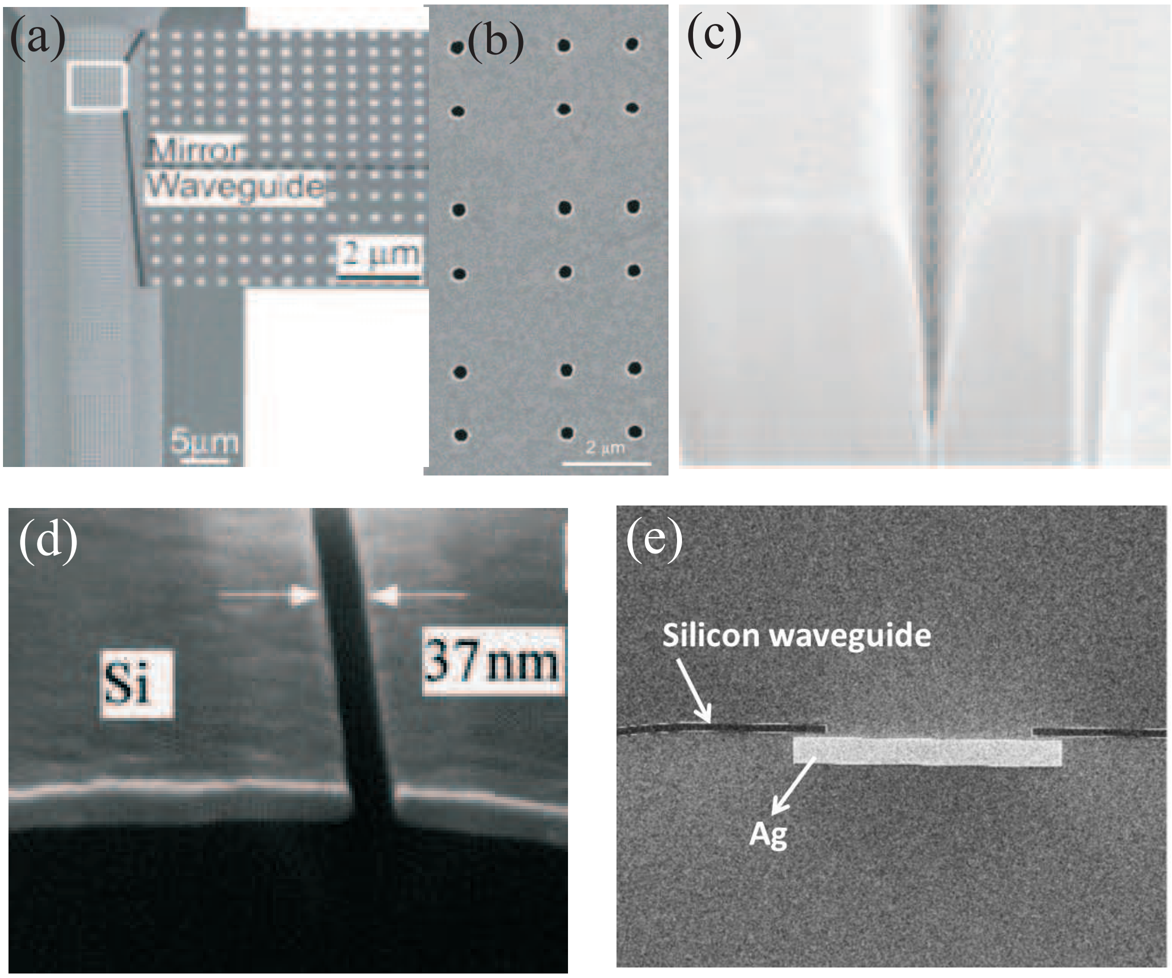

Fig 1.3: Different type of plasmon waveguides: arrays of Au nanoparticles (a), nanoholes (b) ,nanogroove (c), nanogap (d), and an hybrid waveguide consisting of a silicon waveguide and a Ag nanowire (e). Images extracted from [59], [61], [65], [62] and [74], respectively.

waveguide size and plasmon decay length for optimized nanowires.

### 1.2.1 Properties of SPP propagating in metal nanowires

**Dispersion relation in nanowires**

The electromagnetic field of a surface plasmon is the solution of Maxwell's equations in each medium taking into account boundary conditions [14, 15, 75]. The derivation of the SPP dispersion relation in metal film is obtained by considering a system consisting of a dielectric medium with a real and positive dielectric constant $\epsilon_d$ and a metal with complex dielectric constant $\epsilon_m = \epsilon_m^{'} + i\epsilon_m^{''}$. By solving Maxwell's equations and the associated boundary conditions, the dispersion relation of SPP in thin film can be obtained. However, when SPPs propagate in one-dimensional nanowire waveguides, the geometry of the systems imposes a different dispersion.

The derivation of plasmon dispersion in nanowires was first deduced by considering one-dimensional negative dielectric (ND) pin model with cylindrical cross-section [76] shown in Fig. 1.4(a). Since a metal is a negative dielectric in the near-infrared range, the model treats the metal as an optical waveguide. Cylindrical coordinates were chosen in this model. The optical wave was assumed to propagate in the $z$ direction with a phase constant $\beta$ and an angular frequency $\omega$. The lowest order (0th) TM mode was considered. By solving Maxwell's equations, the electric and magnetic field in the two different dielectric medium $\epsilon_1$ and $\epsilon_2$ can be obtained. From the boundary conditions for $E_z$ and $H_\phi$ at $r = a$, where $r$ is the radius direction of the cylindrical coordinates, $\alpha$ is the radius of the core, the characteristic equation of the 0th-order TM mode reads as follow:

$$\frac{\gamma_2 I_1(\gamma_1 a) K_0(\gamma_2 a)}{\gamma_1 I_0(\gamma_1 a) K_1(\gamma_2 a)} = -\frac{\epsilon_2}{\epsilon_1}, \tag{1.1}$$

where $I_j$ and $K_j$ $(j = 1, 2)$ are the $j$th-order modified Bessel functions. $\gamma_j$ is defined as

$$\gamma_j = (\beta^2 - \epsilon_j \mu_0 \omega^2)^{1/2}, \tag{1.2}$$

where $\mu_0$ is the permeability of free space and $\epsilon_j$ is the dielectric constant. In the case of a metal, $\epsilon_1$ can be regarded as the dielectric constant of metal $\epsilon_m$ and $\epsilon_2$ can be regarded as the dielectric constant of surrounding medium $\epsilon_d$.

Following the pioneering work of Takahara, the SPP dispersion in cylindrical nanowires were extensively studied form theoretical considerations [77, 78] and from experimental data [79, 80, 81]. Near-field spectroscopy [79] and far-field extinction spectroscopy [81]

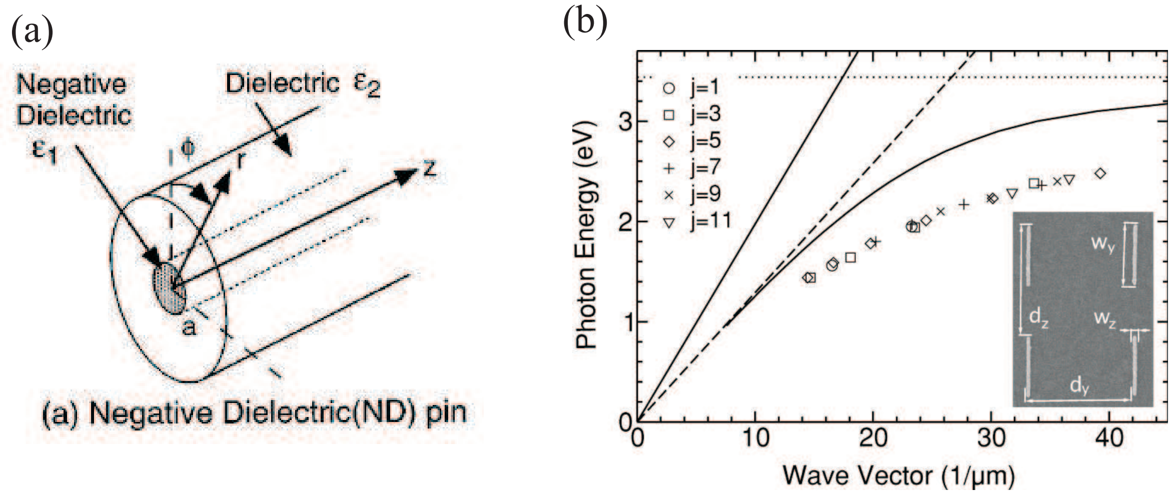

Fig 1.4: (a) Schematic of one dimensional negative dielectric pin model. Image extracted from [76]. (b) SPP dispersion relations for different Ag interfaces. The solid line is light line in vacuum. Dashed line is light line in glass. Solid curve is SPP on silver/glass interface. Dotted line is the limiting frequency $\omega_{SP}$. Symbols are for SPP in Ag nanowires. The wave vector $k = j(\pi/w_y)$, where $j$ is an integer and $j$ values are defined in the legend. $w_y$ is the length of wire. The inset shows the SEM image with the sample geometry. Image extracted from [81].

were used to obtain the dispersion relation of SPPs in metal nanowires. Figure 1.4(b) displays such a dispersion for an array of nanowires measured by extinction spectroscopy [81]. It shows clearly the dispersion differences for light in vacuum, glass and SPP supported by a flat interface and as a mode of a Ag nanowire. At a given frequency, the nanowire SPP has the largest wavevector confirming thus the high degree of optical confinement achieved in these systems.

The SPP dispersion relation is strongly dependent on the size and shape of the nanowires. As the diameter increases, the plasmon resonance frequencies also increases [79]. Nanowires with different cross-sectional shapes have different plasmon resonances. For nanowires with non-regular cross-sections, the electron oscillation can be located along the principle axes or at edges and corners, leading to an additional shape-dependent depolarization and splitting of the surface plasmon resonance into several modes [44]. Figure 1.5 displays the field amplitude distribution for different cross-sectional nanowire shapes. For the non-cylindrical shapes, the field amplitude distributes mainly at corners. These shape-dependent SPP modes are effecting the dispersion relation [82, 83] and will be discussed in more details in the next chapter.

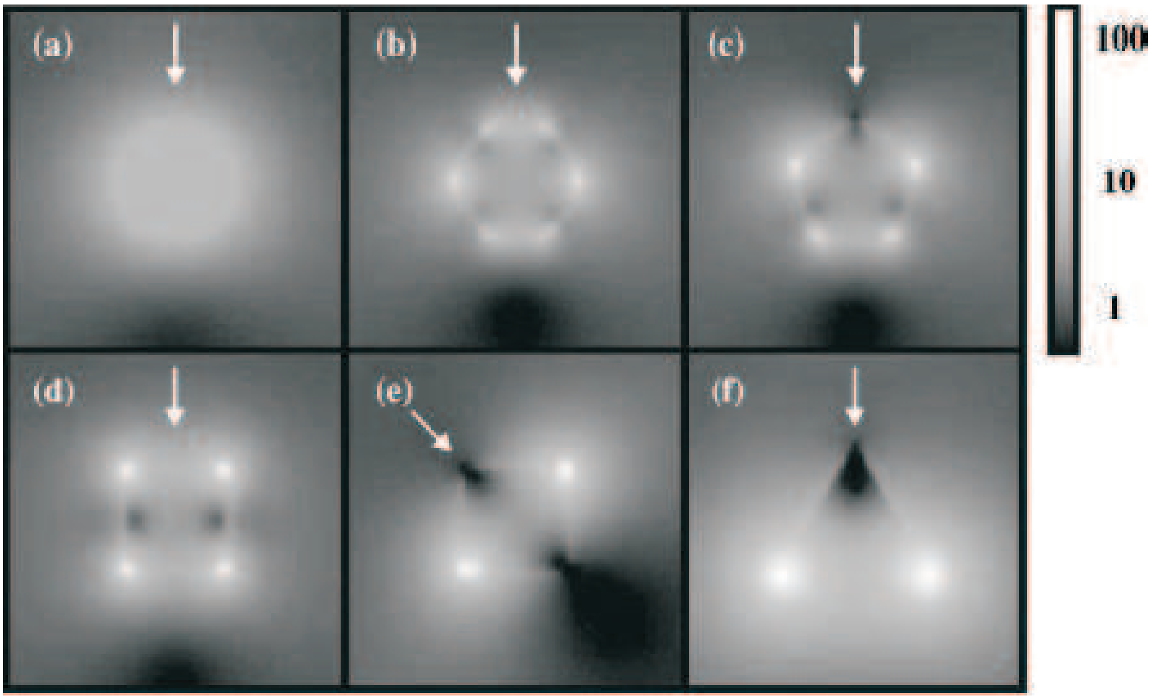

Fig 1.5: Field amplitude distribution for nanowires with different cross-sections at their respective main resonance. (a) circular shape, (b) hexagonal shape, (c) pentagonal shape, (d) and (e) square shape and (f) triangular shape. The diameter of the circular shape is 20 nm. The arrow indicates the propagation direction of the illumination field. Image extracted from [84].

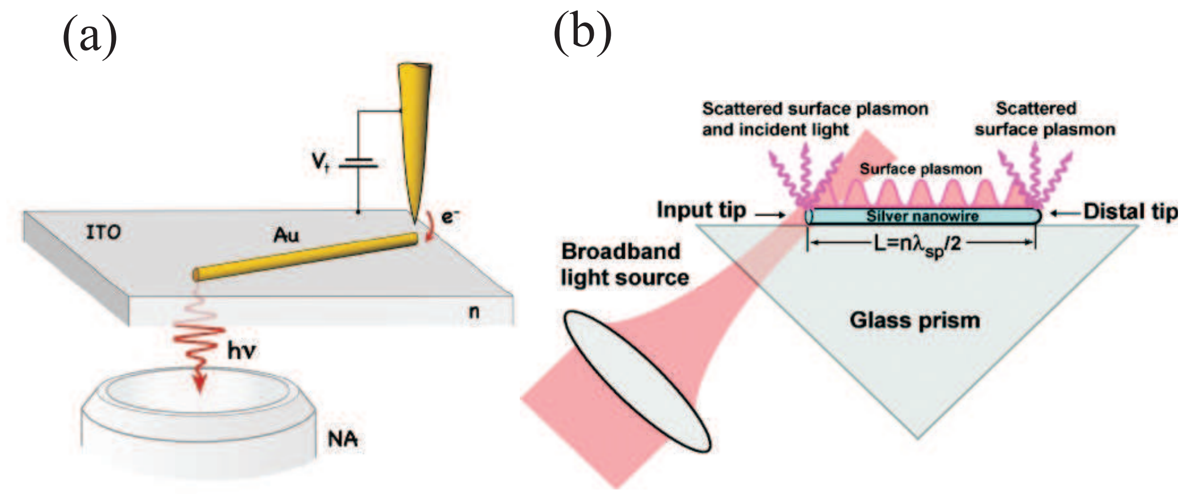

Fig 1.6: Different coupling strategies: (a) Electrical coupling. Image extracted from [85], (b) TIR coupling. Image extracted from [86].

### 1.2.2 Exciting SPP in metal nanowires

#### Coupling strategies

As mentioned above in Fig. 1.4(b), the wavevector of SPPs is larger than that of the light at the same energy. This momentum mismatch means that SPPs cannot be excited directly by light. In order to excite SPPs in nanowires, an extra momentum has to be added to the photons. Therefore, a variety of strategies were developed to launch SPPs in nanowires with different coupling efficiencies.

*Electron excitation*

Electrons penetrating a material can transfer momentum and energy to the solid [14]. This momentum can compensate the momentum difference and excite SPPs. Very recently, electrically excited surface plasmons in gold nanowires was reported by Bharadwaj *et al.* [85]. The schematic of this electrical excitation is shown in Fig. 1.6(a). By employing inelastic electron tunneling between a gold tip and a gold nanowire, localized gap plasmons are excited in the junction and then subsequently couple to propagating plasmons in the gold nanowire. In addition, surface plasmon can be locally excited with an incident swift electrons beam. The radiative signal can be directly detected. The swift electrons excitation provides a unique tool to excite surface plasmon and a synchronous detection with high resolution [87].

*Evanescent coupling*

Compared to electrons, photons are more widely used for coupling SPPs in nanowires. Excitation with photons is easier to implement than electron excitation and can be more efficient. Photons can also provide precise excitation conditions, i.e. monochromatic excitation wavelength for investigating the spectral dependence of SPP properties. Several strategies were implemented to couple photons to SPPs in nanowires. Total internal reflection (TIR) approach, a common technique to launch SPPs in thin films was first used to excite SPPs in nanowires [45, 86, 88, 89]. When light is incident on the metal through glass, SPPs can be excited on the metal/glass interface by evanescent coupling. A conventional Kretschmann-Raether configuration is shown in Fig. 1.6(b). Even though the coupling efficiency could be very high under optimal conditions, the excitation area is typically much greater than the typical surface plasmon propagation. The resulting data are thus the interference between the SPP mode and the incoming radiation.

*Local scattering*

The symmetry breaking introduced by a defect such as wire termination, kinks or an adjacent nanoparticle were used in recent years for coupling light to nanowire plasmons [90]. Excitation at the end of nanowires much similar to the end-fire coupling [93] is probably the simplest approach to excite SPPs in nanowires (Fig. 1.7(a)). Incident light focused on one end of the nanowire is scattered in all directions providing additional wave vectors to match that of the SPP mode. This technique is the preferred strategy for its simplicity. It only requires focusing a laser beam using a high numerical aperture objective [94, 95, 96, 97, 98, 99]. The incident light polarization and the position of focus spot on the nanowire are crucial for optimum coupling. A polarization parallel to the long axis of nanowire can efficiently excite SPPs [86, 88]. However, polarization inhomogeneities in strongly focus spot are adding an extra level of complexity and the coupling become position dependent with respect to the focal fields. This will be discussed in greater depth in the following chapter. Direct illumination on a nanowire kink can also excite SPPs [90, 96] as illustrated in Fig. 1.7(b). The working principle is the same as the termination coupling.

*Fluorescence coupling*

Semiconductor nanoparticles and single photon emitters such as quantum dots and fluorescent molecules provide an alternative route to transfer energy to a nanowire SPP. These nanoparticles are usually artificially attached on the surface of nanowires [91, 100,

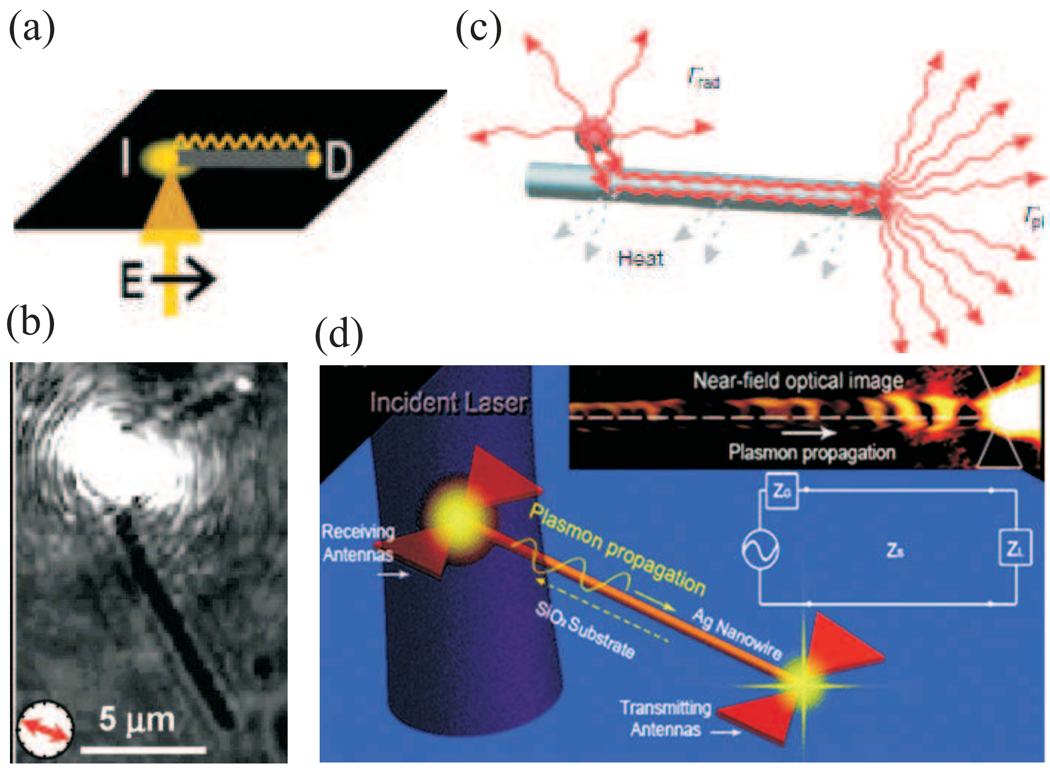

Fig 1.7: Different coupling strategies: (a) Nanowire termination coupling, (b) nanowire kink coupling, (c) single photon source coupling, (d) bow-tie nanoantenna-nanowire coupling. Image extracted from [88], [90], [91] [92], respectively.

101, 102, 103]. In Fig. 1.7(c), a quantum dot serving as an optical emitter can either spontaneously emit into free space or into the guided surface plasmons of the nanowire [91]. Majority of the spontaneous radiation can be captured by the nanowire because of an increased local density of photonic states brought by the SPP mode. This excitation can occur anywhere the nanoparticle is placed, but the distance between the emitter and the nanowire determines the coupling efficiency. SPPs propagating in nanowires can couple back to the nearby emitters. This reversible coupling brings many exciting prospects in surface enhanced Raman scattering (SERS) and surface enhanced fluorescence by taking advantages of the large amplification of the field due to the propagating plasmon.

*Coupling by optical antennas*

Metal nanostructures serving as optical antennas have been predicted recently to efficiently couple photons to SPPs. Structures like bow-tie antennas are promoting a strong coupling of light to SPPs in nanowires [92, 104] (Fig. 1.7(d)). This method is based on a significantly confined electric field inside the nanoantenna which can efficiently couple light to SPPs in adjacent nanowires. The efficiency strongly depends on laser excitation (resonant excitation), the arm length of the bow-tie antenna and also the length of nanowire.

*Waveguide excitation*

In the aim of realizing integrated optical devices functionalities, a variety of in-plane plasmon coupling were recently developed. Basically, in most of these approaches SPPs or photons are coupled from one waveguide to another. Figure 1.8 shows several structures adapted for waveguide-to-waveguide transfer. SPPs can funnel from one structure to the other by joining nanowires end to end [105, 109]. A butt-coupling technique is shown in Fig. 1.8(a). In this approach dielectric fibre (silica fibres and silica nanowires), Ag nanowire (ZnO nanowire) and ZnO nanowire (Ag nanowire) are contacted end to end. The dielectric fiber couples photons to SPPs which after propagation along the Ag nanowire can excite the other type of nanowire, *e.g.* ZnO waveguides [110]. In Ref. [111], body-of revolution finite-difference time-domain (FDTD) calculations were performed to trace the propagation of optical signal along different waveguides: nanowire and dielectric fibre. The conversion efficiency $\eta$ was determined by computing the ratio between the transmitted power in the guided mode right after the nanowire-fibre interface and the incident power at the position right before it. By appropriately choosing the radius and material of the nanowire and the fibre, a high coupling efficiency above 95% can be

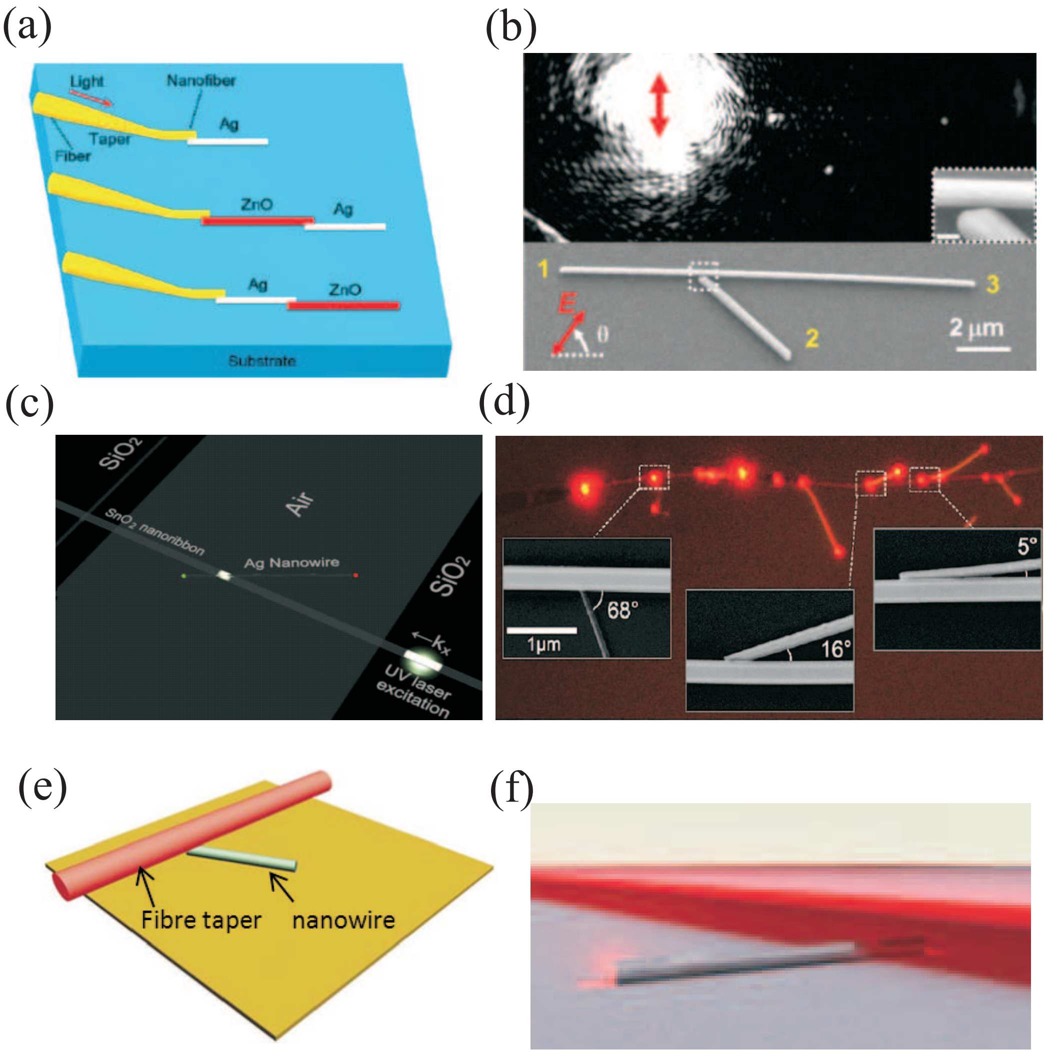

Fig 1.8: Different coupling strategies: (a) butt coupling, (b) branched nanowire coupling, (c) nanoribbon coupling, (d) metal oxide nanowires coupling, (e) optical fibre taper side coupling, (f) polymer waveguide-nanowire coupling. Image extracted from [105], [106], [107], [105], [108] and [26], respectively.

obtained. This structure is akin to the series resistance in conventional electric circuits. This in-plane coupling scheme provides a significant progress towards the integration of photonic and plasmonic elements on the same chip. However, due to the losses that occur while SPP propagating in the first waveguide and passing through the junction, the coupling efficiency for the second waveguide is relatively low.

Instead of contacting waveguides end to end, which requires a precise alignment procedure, SPPs can be launched into metal nanowires by simply contacting a nanowire to a main waveguide at an arbitrary position and orientation. If several nanowires contact the waveguide at different positions, SPPs propagating in the main waveguide can be distributed into several branches simultaneously. Recent investigations illustrated in Fig. 1.8 demonstrated that metal nanowires [106], metal oxide nanoribbons [107] and nanowires [105], tapered optical fibres [108] and polymer waveguides [26] can be employed to couple SPPs into several nanowires simultaneously. The coupling efficiency strongly depends on the position of the branches and their angular orientation with respect to the main waveguide [105]. In these configurations, one excitation input can lead to several outputs. By controlling the polarization, phase and frequency of the input field, a signal can be guided to a specific output. These waveguide to waveguide coupling configurations show the enormous potential for the development of nanocouplers, nanorouters, nanosplitters and interferometric logic functionalities [112].

### 1.2.3 Detecting propagating SPP in nanowires

#### Imaging techniques

The properties of SPPs are intimately related to their field distribution on the metal surface. Therefore, knowledge of this field arrangement is vital for understanding how surface plasmons are waveguided along metal nanowires. Since SPPs are generally strongly confined at the metal surface, their detection mainly relies on near-field techniques and other indirect measurement typically based on field enhancement mechanisms. Scanning near-field optical microscopy (SNOM) [88, 92, 113, 114, 115], photon scanning tunnelling microscopy (PSTM) [116], photoemission electron microscopy (PEEM) [117] which is based on a multi-photon ionization of the electrons and the recently emerged scanning transmission electron microscopy (STEM) combined with electron energy-loss spectroscopy (EELS) [118, 119, 120] have been successfully used to detect and map the field distribution of SPPs. Near-field microscopy is a proximal probe technique capable of retrieving locally the SPP field directly over the metal surface [23, 75, 121]. Figure 1.9(a) displays a

PSTM image of the surface plasmon field developing along a metal nanowire. The white curve on the left bottom shows the cross-cut along the dotted line [88]. The resolution of near field image is beyond the diffraction limit of light [122]. However, it is limited by the quality of the proximal probe used in a given experiment.

Surface enhanced florescence and surface enhanced Raman scattering (SERS) [126, 127, 128] can provide an indirect mapping of SPPs. Plasmon propagation along nanowires can be visualized by covering the structure by a layer of fluorescence molecules [16, 123, 129, 130, 131] (Fig. 1.9(b)) or by decorating the nanowire surface with quantum dots [103, 112, 132, 133]. Fluorescence imaging is very fast and sensitive, especially it is useful for imaging the plasmon local field distribution on larger scale [134]. However the resolution remains limited by the diffraction and the photostability of the fluorescence reporters.

Photochemical imaging has also been exploited for the mapping of optical near-field of nanostructures. This imaging relies on the local photoisomerization combining with a measure of a surface deformation by atomic force microscopy (AFM) [135]. Optical near-field of silver nanorods were imaged using this technique in Ref. [124]. Silver nanorods were embedding in photoresponsive azo-polymer which is known for the cis-trans isomerization and wormlike transport of the polymer under illumination [124]. After exposure, optically induced topography was characterized in situ by atomic force microscopy. Figure 1.9(c) displays the photoinduced topography after 20 min exposure. The white circles at the extremities indicate the formation of protrusion due to the longitudinal components of the electric field on several rods. In addition, photochemical imaging was also used to image the nonresonant field on a metal/dielectric interface on gold nanorods [136]. Photochemical imaging is very sensitive to both field gradient and polarization and thus, can provide complete vectorial description of the near-field which can't be achieved by other imaging techniques. However, the wavelength sensitivity of the chemical formulation is restricting investigation to a short-wavelength range in the visible.

Another indirect indication of a plasmon propagating in a nanowire was established by an electrical detection [137, 125]. Electrical detection of SPPs in nanowires in Ref. [125] is based on the SPPs coupling to a Ge nanowire field-effect transistor (Fig. 1.9(d)). When SPPs propagate to the silver-Ge junction, they are converted to electron-hole pairs and detected as a photocurrent. On the other hand, when electrical current and SPPs syn-

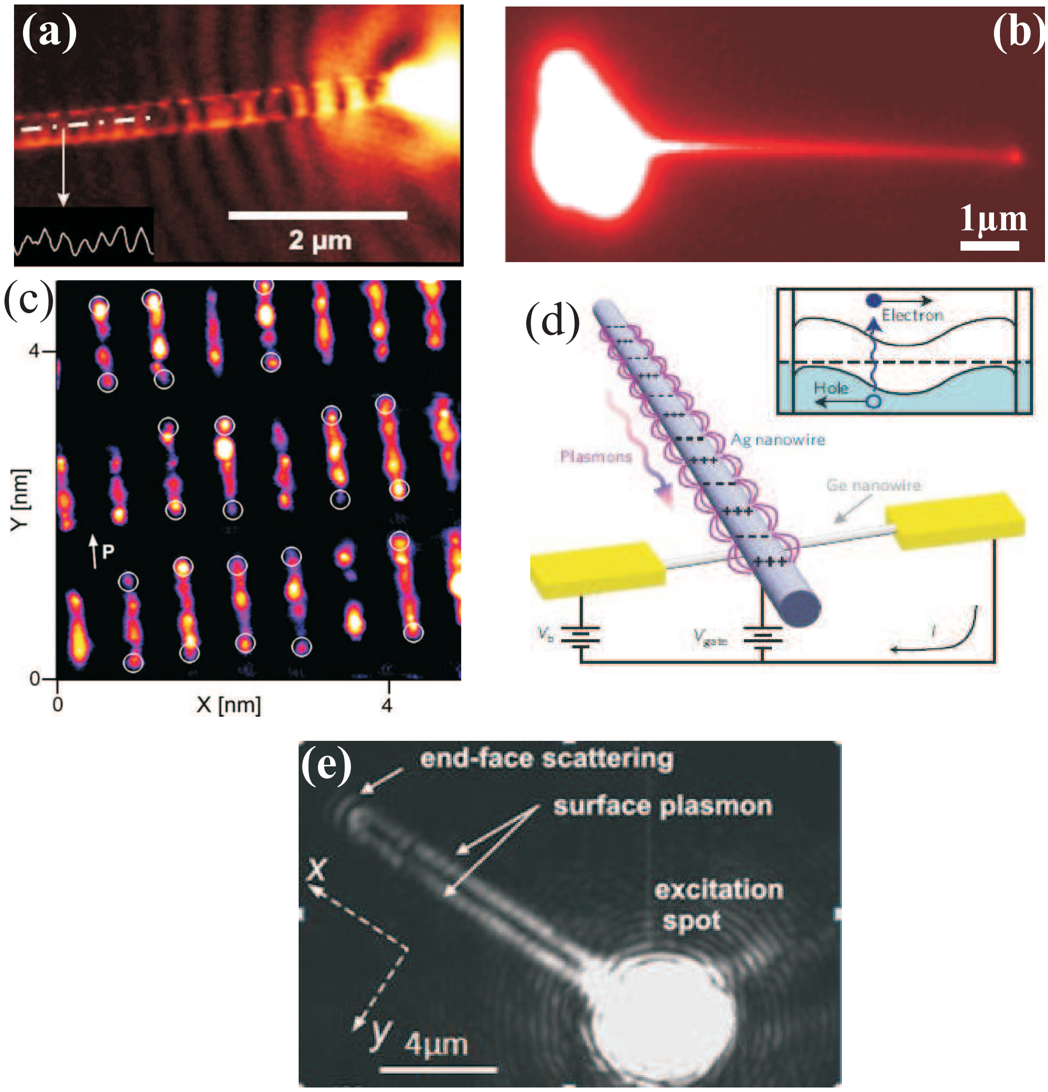

Fig 1.9: Images of SPPs propagating along nanowires using different detection techniques: (a) PSTM image. The white curve on the left bottom shows the cross-cut along the dotted line. (b) Two-photon fluorescence image. (c) AFM characterization of photoinduced topography after 20 min exposure of a silver nanorod coated with photoresponsive polymer DR1MA/MMA. The photochemical imaging of longitudinal components of the electric field on several rods is outlined by the white circles. (d) Schematic diagram of electrical detection with a nanowire field-effect transistor. (e) Leakage radiation microscopy image. The SPP mode is regarded as two bright lines on the two sides of the wire. Image extracted from [88], [123], [124], [125], [83], respectively.

chronously transported in the nanowire waveguide, they could also be detected using electrical detection. The synchronous transport of electrons and surface plasmons will be discussed deeply in chapter 3. Electrical detection can be integrated directly into plasmonic circuits which may provide a way to realize a complete plasmo-electronic nanocircuit [1]. However, a direct visualisation of plasmon propagation in the nanowire using far-field technique is required most of the time.

In principle, because the SPPs field is confined to the surface it cannot be mapped directly using conventional far-field technique. One possibility using far-field technique is to detect the scattering light produced by SPPs out-coupled at the discontinuity of the nanowire, e.g. its distal end. Information about SPPs are then derived from this scattering event and used to analyse the distribution and the propagation properties of SPPs. When SPPs are excited in an asymmetric environment such as glass/metal/air multilayer, plasmon may couple out and transform their energy to photons in the dielectric medium with higher refractive index, e.g. glass. This intrinsic loss is called leakage radiation (LR). Detecting this leakage radiation enables a direct quantitative imaging and analysis of SPP propagation [138]. Leakage radiation microscopy (LRM) is a microscopy based on the collection of this radiation damping. Since the characteristic radiated inclination angle $\theta_{SP}$ of LR with respect to the normal of the interface is larger than the critical angle of the substrate/air interface (usually glass/air) [113, 139], the detection requires an oil-immersion lens for index-matching purpose. Figure 1.9(e) displays a leakage radiation image of a nanowire excited at one end by a focused laser beam emitting at $\lambda$= 800 nm. The propagation of the SPP mode along the wire is readily seen taking as two luminous lines located at either side of the nanowire [83]. Since LRM is based on the collection of leakage radiation, the bound SPP modes are not accessible. However, as a far-field direct detection of SPP spatial intensity, LRM is relatively simple to implement and is versatile compared with other detection techniques [140].

### Propagation loss

Relying on various detections discussed above, the propagation properties were deeply studied. The propagation length $L_{SPP}$ is defined as the distance at which the SPP intensity has decayed by a factor of $1/e$ [75]. For metals in the visible and the near-infrared range, the dielectric constant is a complex number leading to a complex SPP wave vector: $k_{SPP} = k'_{SPP} + ik''_{SPP}$. The propagation length is therefore written as $L_{SPP} = 1/2k''_{SPP}$.

When a SPP propagates along a nanowire, it may lose energy through two channels: intrinsic channel (nonradiative losses) and extrinsic channel (radiative losses). The non-radiative losses are due to the absorption of the energy in the metal which depends on the dielectric function at the oscillation frequency of SPPs [107]. The radiative losses are attributed to the leakage radiation into the substrate and back-coupling of SPPs into photons such as the scattering due to the roughness, defects on the nanowires (end-face scattering).

The determination of propagation length is usually based on the detection of radiative losses losses either using near-field imaging combined with far-field emission spectroscopy [86, 88, 141, 142, 143] or indirect mapping such as the fluorescence imaging [123]. Figure 1.10(a) shows the scattered light spectra that was taken at the distal end of a 18.6 $\mu$m long Ag nanowire with 120 nm of diameter. The scattering off the wire is clearly observed in the near-field image shown in Fig. 1.9(a). The modulation depth $\Delta I/I_{min}$ in the spectra is given by the intensity related parameters: propagation loss A and end face reflectivity R. By measuring the modulation depth $\Delta I/I_{min}$ of several nanowires, the propagation loss A and reflectivity R can be deduced. According to the relation $A = e^{-l/L_{SPP}}$ ($l$ is the nanowire length), the SPP propagation length $L_{SPP}$ (∼10.1±0.4$\mu$m) can be obtained [88]. This determination of propagation length is based on the Fabry-Pérot resonance. Since in the case of thin nanowires, the bound SPP mode is the dominant mode. SPPs propagate to the distal end of the wire and then are reflected back displaying well-defined Fabry-Pérot resonance in spectroscopic measurement. However, in the case of thick nanowires, the leaky mode is the dominant mode. Light emission at the end is efficiently scattered out and the reflection coefficient vanishes. Light emission becomes unidirectional and Fabry-Pérot resonances are washed out [144]. The unidirectional light emission was recently investigated by Timur Shegai and his co-workers [145]. The effect of geometrical properties of thick nanowires on the SPPs propagation is poorly understood and will be discussed in depth in the next chapter.

The propagation length measured from indirect imaging of fluorescence is based on the the ability of propagating SPPs to excite the fluorescence of dye molecule located at close proximity of the nanowire surface [123]. Figure 1.10(b) shows two-photon fluorescence intensity distribution which decays exponentially along a Ag nanowire. Since for two-photon fluorescence, the decay length is half of the propagation length. According to the relation:

$$I_{fluor} \sim (I_{SPP})^2 = I_0 e^{-2x/L_{SPP}}, \tag{1.3}$$

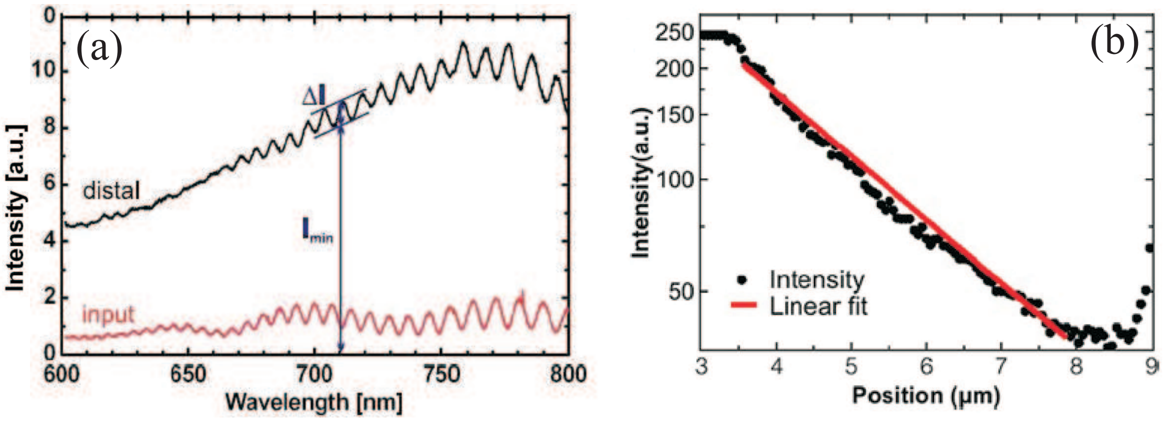

Fig 1.10: (a) Scattered light spectra taken from the end facet scattering light of a 18.6 $\mu$m long nanowire with diameter 120 nm. The arrows define ΔI and Δ $I_{min}$. Images extracted from [88]. (b) Two-photon fluorescence intensity distribution of a Ag nanowire. Points are experimental data; red line is exponential fit (linear fit on logarithmic scale). Images extracted from [123].

the propagation length is readily determined. For silver nanowires with diameter 70 nm, propagation lengths ranging from 11 to 17.5 $\mu$m were measured.

The effect of nanowire geometry and external factors such as excitation wavelength and substrate on propagation losses has been intensively studied. In a recent study, the effect of excitation wavelength and nanowire diameter on the bending loss was determined [146]. The measured bending loss for varying bend radii is displayed in Fig. 1.11. The disappearance of emission light at the end of the bent wire in the dark-field optical images in Fig. 1.11(b) indicates that bending loss scales with the radius. The plotted bending loss in Fig. 1.11(c) exhibits an exponential attenuation trend with increasing bending radius and achieves 11 dB when the radius decreases to 5 $\mu$m [146]. The quantitative and qualitative investigations of bending loss in metal nanowire are important for the practical application of SPP-based devices in photonic and plasmonic circuits.

SPPs propagation at telecommunication wavelength and related propagation loss were demonstrated in multiple instances [99, 114, 147, 148, 149] indicating that the frequency-dependent nonradiative loss is smaller at longer wavelength.

Since leakage radiation is also a main part of the radiation loss, the effect of substrate on the propagation loss has become an area of interest. The effect of different substrates such as ITO/glass, quartz and $MgF_2$ were investigated [99, 150]. Higher refractive index provides a higher damping of the SPP. Furthermore, the separation distance $g$ between nanowire and substrate was also studied [151, 152]. It was argued that when the separation

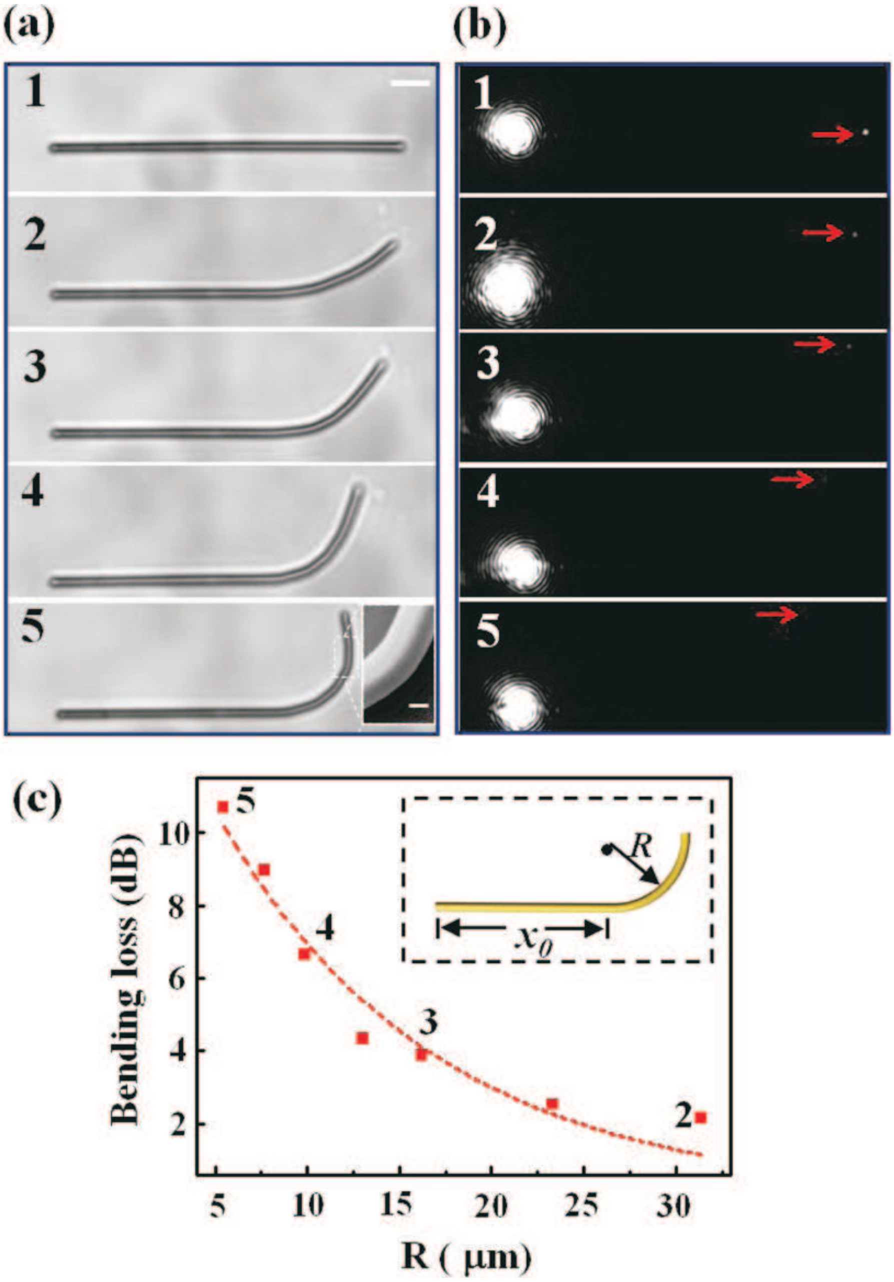

Fig 1.11: Measured bending loss for varying bending radii. (a) Images 1-5 are selected bright-field optical images demonstrating the bending process of the Ag nanowire with diameter of 750 nm, length of 45 $\mu$m, and bending radii of $\infty$, 32, 16, 9, and 5 $\mu$m, respectively. The inset is the SEM image of the curved section with scale bar of 350 nm. (b) The emitted light at the bent end of Ag nanowire which was excited at 785 nm are indicated by the red arrows. The scale bar is 5 $\mu$m in both (a) and (b). (c) Pure bending loss as a function of bending radius. The red curved line is the exponential fit to the bending loss in the Ag nanowire at certain bending radius. Inset: geometry of the bent wire. The length of the straight section is $x_0$, and the bending radius is R. Images extracted from [146].

distance is below a certain value, *i.e.* $g$ =50 nm, the absorption loss decreases with increasing distance. When the distance is above that value, the absorption loss suddenly increases due to the coupling to the dissipative travelling wave in the substrate. When the distance continues to increase to above 200 nm, the role of substrate can be neglected [152]. The results indicate that for an efficient detection, $g$ should be larger than 200 nm or smaller than 10 nm. These investigations could help to choose the proper configuration for designing optimal waveguides in optical circuits.

### Propagation loss compensation

To have a longer propagation length, propagation losses need to be reduced. For the purpose of reducing roughness-induced scattering loss, chemically synthesized single crystalline nanowires with smooth surface are usually preferred. They can significantly reduce the radiative loss compared to metal nanowires fabricated by electron-beam lithography which introduces grain boundaries and structural defects [26, 88, 150]. Among all the metal nanowires, silver is the most preferred material since it has the lowest loss [23, 25, 153].

In order to reduce the detrimental effect of surface plasmon damping in a plasmonic circuitry, proposals for compensating losses by incorporating optical gain into plasmonic systems have been reported. Grandidier *et al.* demonstrated an increase of propagation length by doping a dielectric-loaded surface plasmon polariton waveguides (DLSPPW) with quantum dots nanocrystals undergoing stimulated emission of plasmons [148]. Other assisted propagation exploiting optically pumped polymer doped with erbium ions [147] or dye [154] have successfully obtained an increased propagation length. From the practical point of view, these concepts face material limitations such as fatigue, optical stability, and operation temperature. Some strategies have emerged to minimize the requirement for compensation of losses. Handapangoda and his co-workers proposed using composite nanowire waveguides consisting of a metal nanowire and an optically-pumped dielectric cladding [155]. This method appears to be simpler, but reducing propagation losses by proper selection of the geometrical parameters of the nanowires themselves remains the most straightforward way.

## 1.3 Functionalities of nanowires

As a fundamental building block for developing a subwavelength optical circuitry, metallic nanowires have been thoroughly investigated as a basis for active plasmonic devices.

Nanowire-based waveguide with different termination shapes can serve as a polarization rotator [153]. The polarization of light emitted by end-face SPP scattering was affected by the geometry of termination. By changing the end shape of the nanowire through precise chemistry, polarization could either be maintained or rotated [153]. Furthermore, the angular distribution of the scattered SPP indicated that nanowire waveguides could serve as a broadband antenna [45, 98, 145]. Diameter, excitation wavelength, and material dependent unidirectional light emission were found in Ref. [45, 145]. A bimetallic wire with a sharp Au/Ag heterojunction displays unidirectionality with respect to plasmon propagation across the heterojunction.

Network of nanowires is typically offering a complex control of SPP routing. Crossed nanowire structures composed of a main nanowire and one or several branches were employed for different functionalities. The branched nanowire can serve as a second output of plasmon which functions as a router and multiplexer [106] or serves as an input to launch another plasmon which may function as a modulator [156] (Fig. (Fig. 1.12(a) and (b)). The realization of different outputs in Fig. 1.8(b) relies on the control of polarization of the input beam. In Fig. 1.12(a), the branched nanowire serves as an additional input. If the two input channels have the same polarization, different emission intensities at the network output were obtained due to the phase difference between the two paths. By changing the relative phase or the polarization angle of the two input signals, the signal emission at the output can be modulated [156]. More complicated configuration using a two inputs/two outputs nanowire network was reported very recently. In Fig. 1.12(b), the network is composed of two inputs $I_1$, $I_2$ and two outputs $O_1$, $O_2$. Images from $i$ to $v$ describe the SPP-coupled fluorescence of quantum dots placed at the two outputs. By changing the polarization and phase of the two input beams, the two output intensities can change in an alternate manner [112]. This strongly depends on the near-field intensity of the branched wire and main wire junction. The physical mechanism underlying these functionalities is the interference of plasmons launched at different positions of this network. The interference of the two plasmons affects the near-field distribution and consequently the output intensity. This kind of multi-input and multi-output nanowire network can be used to realize interferometric logic function.

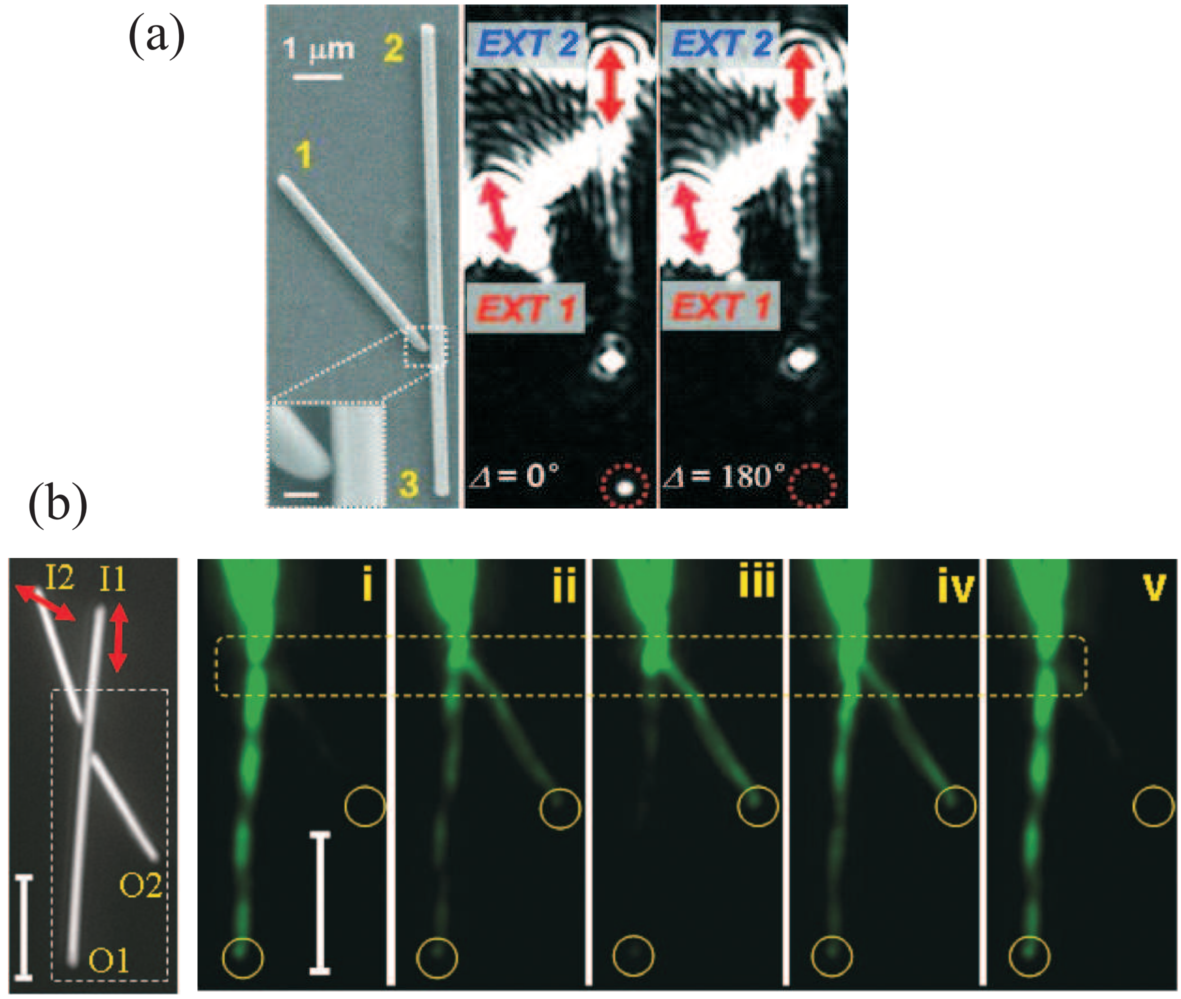

Fig 1.12: (a) A branched nanowire structure serves as a plasmon modulator. The branch nanowire serves as another input for launching the second plasmon. The arrows show the excitation polarization. Images extracted from [156]. (b)Modulation and routing of light in a two inputs/two outputs nanowire network. Images $i - v$ are the quantum dot emission images of one interference cycle. Images extracted from [112].

## 1.4 Research motivations

As briefly discussed in the few pages above, the unique properties of SPPs is attracting a considerable interest to a wide spectrum of scientists. Plasmonic circuits may offer the potential to carry photonic signals encoded on the form of surface plasmons, but also electronic signals in the same metal waveguide. In this context, metallic nanowires are promising candidates for their large potential of integration. The basic and fundamental properties of SPPs propagation (dispersion relation, propagation losses, coupling and emission) are relatively well understood. Specific structures have been designed for the realization of different functional components. Although much efforts were made experimentally and theoretically, the technology still faces several practical challenges, notably concerning its interfacing with an electronic control layer. The realization of SPP-based subwavelength optical circuits strongly depends on resolving several pressing issues: the efficient coupling to nanoscale waveguides, the effective detection and the implementation of functional components within the limitations imposed by inevitable SPP propagation losses [1]. Another consideration that should be noted is that plasmonic waveguides are directly mounted on chips. This requires a simple, effective and scalable architecture. According to the vast majorities of research work and properties highlighted above, SPP waveguides based on metal nanowires are no doubt the most simplest structures. SPPs propagation in nanowires can be excited by simply focusing a laser beam on one end facet and redirected to other directions or coupled to other components. Since geometrical considerations are strongly affecting the coupling efficiency and propagation properties, better performance can be obtained by optimally selecting geometrical parameters. This is based on the complete understanding of the characteristics of SPPs in nanowires with different geometries which remains unexplored so far. The last but not the least is that metal waveguides will carry not only plasmons but also electrons. When SPPs and electrons are transported in a waveguide simultaneously, the interplay between them is a crucial issue that needs an in-depth investigation. However, to our knowledge, few investigations have addressed this critical and non-negligible issue.

This manuscript is divided into two major parts: in the first part, we investigate the SPPs propagation properties in individual penta-twinned crystalline silver nanowires by using dual-plane leakage radiation microscopy. The corner modes supported by pentagonal silver nanowire will be studied. Polarization inhomogeneity selecting leaky mode and bound modes will be demonstrated. The effective index and the losses of the mode propagating in this structure will be determined. The effect of wire geometry (length, diameter) and substrate on the effective index and propagation loss will be investigated. Numerical simulations will be introduced to confirm the results.

In the second part, measurements will be carried out on electrically contacted nanowires and the simultaneous transport of SPPs and electrons in nanowires will be recorded. We will investigate to what extend these two information channels interfere in a crystalline silver nanowire and estimate the limiting operating conditions. Some conclusive remarks and perspectives will be given at the end of this thesis.

# Chapter 2

# Details of SPP propagation in crystalline silver nanowires

## 2.1 Research motivations

As already discussed in the introductory chapter, metallic nanowires offer potential for high miniaturization and integration of on-chip optical interconnects. This simple one dimensional structure with two sharp ends provides an easy and effective way to couple light into nanowire in the form of surface plasmons. The properties of SPPs propagation vary with geometrical parameters defining a given nanowire. Therefore, an in-depth study of the details of SPPs propagation in these systems is essential to exploit SPP-based optical components.

To fully understand SPP propagation, imaging techniques are necessary to probe directly or indirectly the plasmonic electromagnetic field distribution. As introduced in last chapter and because of the strong confinement of the SPP mode, the observation of plasmon propagation requires either near-field imaging [79, 88], photoemission electron microscopy (PEEM) [117], or indirect mapping of polymer fluorescence [129, 131]. By analyzing the associated spectra and images, SPP propagation properties such as propagation losses can be deduced.

Although these technically challenging techniques are useful for imaging SPP field distribution, they are well-suited for strongly bound modes in thin nanowires with diameter $D < 100$ nm or highly damped SPPs characterized by short propagation lengths. When longer propagation lengths are required as in optical interconnects, we propose an alternative approach, namely dual-plane leakage radiation microscopy, to directly measure the effective indices of the relevant modes propagating in thicker silver nanowires. Leakage radiation imaging can not only image direct space information but also its wave vector content [113, 138, 139]. A direct measurement of the propagation constant, inaccessible with other techniques, is critically important to fully understand the details of SPPs propagation in these one-dimensional metal waveguides.

In this chapter, we aim to investigate the fundamental propagation properties of SPPs in Ag nanowires exploiting convenient and effective excitation and detection strategies. Chemically synthesized crystalline Ag nanowires are usually preferred since they present lower Joule losses compared to lithographed amorphous structures obtained by metal evaporation [88]. Although these chemically synthesized metal nanowires naturally crystallize with five-fold symmetry [95], their supported plasmon modes are always discussed assuming a circular cross section [76, 157, 158]. We will show in the following that the wire morphology is affecting the SPP parameters, and a precise knowledge of the nanowire is required to fully understand plasmon propagation.

## 2.2 Experimental

### 2.2.1 Nanowire synthesis

The nanowires used in this study were provided by our collaborators Jadab Sharma and Erik Dujardin at CEMES, Toulouse.

Silver nanowires were synthesized by a modified protocol based on the polyol process [159]. In general, the polyol method produces nanowires with diameters below 100 nm. The fundamental SPP mode of thin nanowire is tightly bound to its surface and is thus too restrictive for our leakage radiation microscopy. Therefore, some adjustments of the synthesis protocol were implemented to increase the nanowire diameter [160]. The modified synthesized protocol is as follows: A solution of 1 mM $H_2PtCl_6$ in 5 mL of ethylene glycol was refluxed for 1 h at 150°C and constant stirring in a 100 mL three-necked round bottom flask. Once the Pt seed particles were formed, two solutions of 5 mL of $AgNO_3$ (76.5 mM) and 5 mL of polyvinylpyrrolidone (PVP, $MW = 55000$, 0.2 g) in ethylene glycol were added slowly and simultaneously to the reaction flask using two separate dropping funnels. Temperature and stirring rate were adjusted to 165°C and 600 rpm, respectively, prior to the addition of silver salt and polymer. Reaction was continued for 1 h after the addition and followed by cooling to room temperature. The reaction was performed under argon flow throughout the reaction to avoid oxide formation. The Ag

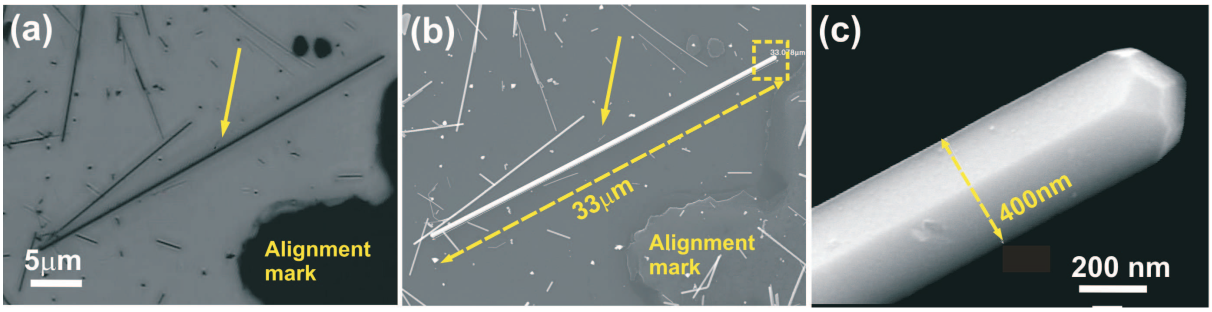

Fig 2.1: Nanowires characterized by bright-field optical and scanning electron microscopies (SEM). (a) Bright-field image of a selected 33 $\mu$m long nanowire with a width of 400 nm (arrow). (b) SEM image of the same nanowire. (c) High-resolution SEM image of the nanowire termination. The pentagonal cross section is readily visible.

nanowires were separated from other particle by-products by a careful centrifugation after adding an excess amount of acetone. This purification step was repeated three times, and nanowires were finally dispersed in 30 mL of ethanol and stored in a refrigerator for future use.

In all of our optical experiments, crystalline Ag nanowires were deposited by a drop-casting method on glass substrates bearing a grid landmark pattern. The nanowires were then imaged and located by a conventional optical transmission microscope. Scanning electron microscopy (SEM) was subsequently used to precisely measure the geometrical dimensions of the nanowires. SEM was carried out on a JEOL 6500 at an acceleration voltage of 20 kV. The SEM imaging was performed after plasmon characterization in order to limit the deposition of carbon contamination on the crystalline nanowires (the effect of carbon contamination on plasmonic nanostructure is discussed in the Annex). Figure 2.1(a) displays an image of a selected nanowire (arrow) placed next to an alignment mark. Fig. 2.1(b) is a SEM image of the same nanowire observed in Fig. 2.1(a). The length of this nanowire is 33 $\mu$m. A close up view of its right extremity is displayed in Fig. 2.1(c) emphasizing the pentagonal profile of the synthesized crystalline nanowires. For the sake of simplicity, we define the diagonal dimension of the pentagon as the diameter $D$ of the nanowire.

### 2.2.2 Leakage radiation microscopy

Leakage radiation microscopy is relying on a radiation-loss mechanism of the SPP mode occurring when a thick nanowire is deposited on a glass surface. The presence of the

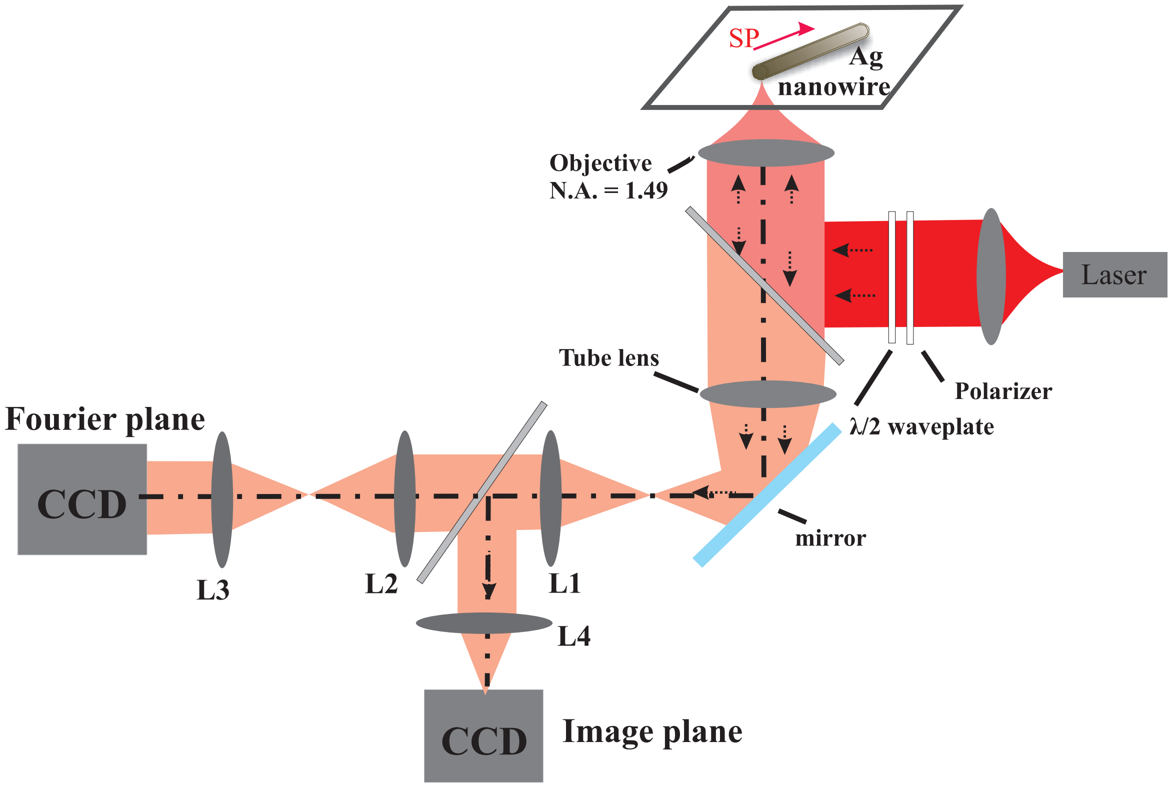

Fig 2.2: Setup of leakage radiation microscopy of surface plasmon mode propagating in the nanowire. A laser beam is focused at one end of the nanowire by a high numerical aperture objective. Scattering at the extremity insures the excitation of a SPP mode in the nanowire. The radiation losses of SPP coupled in the substrate are collected by the same objective and are recorded in secondary image and Fourier planes. Relay lengths L1, L2, L3 and L4 with focal length 100 mm, 100 mm, 150 mm and 125 mm, respectively adjusted at the exit port of the microscope provide a set of imaging planes conjugated either with the field plane (object) or with the aperture plane (Fourier) of the microscope.

underlying high-index medium fulfils the phase-matching condition for a decoupling of low-effective index SPP modes into photons that are radiating in the substrate. The principles of leakage detection of surface plasmons are described in Fig. 2.2. The leakage microscope was retrofitted on a Nikon TE2000 inverted microscope. A 532 nm green laser and a tunable CW Ti:sapphire (675-1100 nm) laser were used for SPP excitation at different wavelengths. The laser beam was coupled into the epi-port of the microscope with a diameter completely filling the entrance pupil of a high numerical aperture oil-immersion objective (100×, $NA = 1.49$, Plan-Apo). The laser beam was then focused on a diffraction-limited spot at one end of a nanowire. The polarization state of the excitation was controlled by a combination of a polarizer and a half-wave plate. The images were acquired without any aperture or field stops. A combination of relay lenses L1, L2, L3, L4 with focal length 100 mm, 100 mm, 150 mm and 125 mm respectively adjusted at the exit port of the microscope provide a set of imaging planes conjugated either with the field plane (object) or with the aperture plane (Fourier) of the microscope. Light scattered at the end of the nanowire and leakage radiation of the plasmon mode during propagation are collected by the same objective lens and imaged on two CCD cameras (Luca from Andor and Orca from Hamamatsu), respectively, conjugated with the image and Fourier planes of the microscope. Collection of these leakages with a high numerical aperture oil-immersion objective [138, 161] and subsequent recording of the image and Fourier conjugated planes of the microscope provide information about the SPP intensity [162] and wave vector distributions, respectively [163, 164].

Concerning the wave vector distribution in the Fourier plane, the relay lens L3 in Fig. 2.2 acts as a Fourier transformer [165, 166]. As we illustrated in Fig. 2.3, the rays emanating from the front focal plane of a converging lens are collected by the lens and brought to convergence at its back focal plane, the so-called Fourier plane. The electric field distribution across the object is Fourier transformed by the lens into a far field Fraunhofer diffraction pattern [165]. All the diffracted waves maintain their phase relationships travelling essential equal optical path lengths to the transform plane. Therefore if a screen or a CCD camera is placed at the Fourier plane, the angular distribution of the electric field in far field could be seen or imaged. This provide a unique experimental tool to access the distribution of wave-vector contained in a leakage radiation image.

Imaging with an aplanatic, infinity-corrected objective, the angular distribution is projected into an intensity distribution distributed around the optical axis in the back focal plane of the objective [167]. A linear relationship exists between the sine of the angle of emission $\theta$ emanating from object and the distance $\rho$ in the Fourier plane from

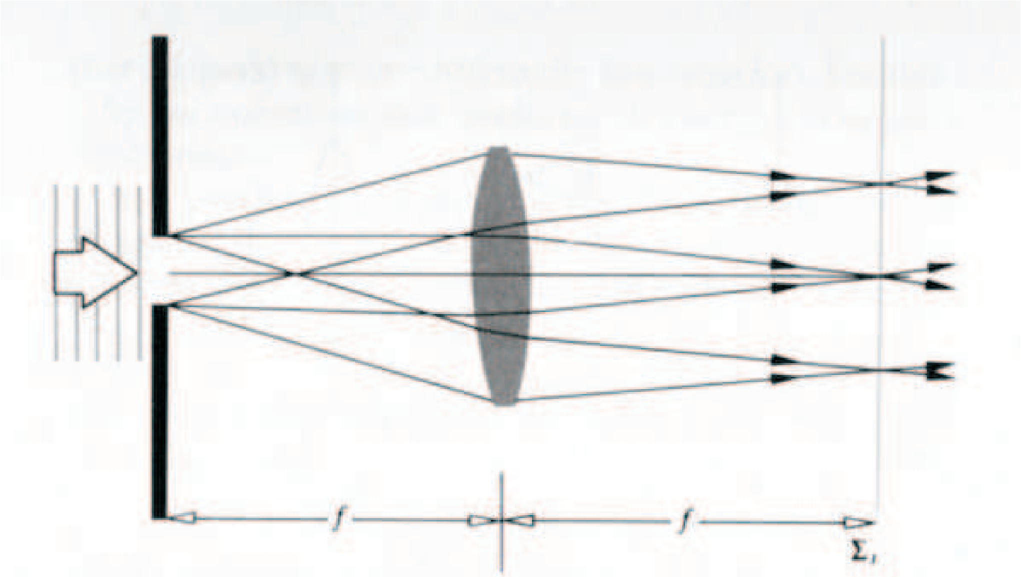

Fig 2.3: The light diffracted by an aperture at the front (or object) focal point of a lens converges to form the far-field diffraction pattern at the back focal point of the lens. Images extracted from Ref [165].

the optical axis:

$$\rho = f n \sin\theta, \tag{2.1}$$

where $f$ is the focal length of the objective and $n$ is the refractive index of the immersion medium. $nsin\theta$ or equivalently the effective numerical aperture or in-plane wave vector $k_{//}$ are proportional to the distance $\rho$. Therefore, the angular distribution is converted into an intensity distribution over the Fourier plane [167] which results in a direct measurement of the wave vector distribution. Thus, by imaging the leakage radiation at the Fourier plane, the wave vector distribution of the surface plasmon could be obtained.

The calibration of the Fourier plane was obtained by combining the known value of the numerical aperture of the objective and the critical angle at the glass/air interface. The Fourier plane shown in Fig. 2.4 was produced by focusing the laser beam on bare glass substrate. The white line crosses the center at the optical axis (point $O$) and intersects with the two edges of the bright annulus at four points: $A$, $B$, $C$, $D$ in Fig. 2.4(a). The annulus is the result of total internal reflection at the glass/air interface. The inner circle of the annulus corresponds to the critical angle $N_{crit}$=1.0, so we define the value $B$ and $C$ along the diameter as $N_B$= -1.0 and $N_C$= 1.0, respectively and the center $N_O$=0.

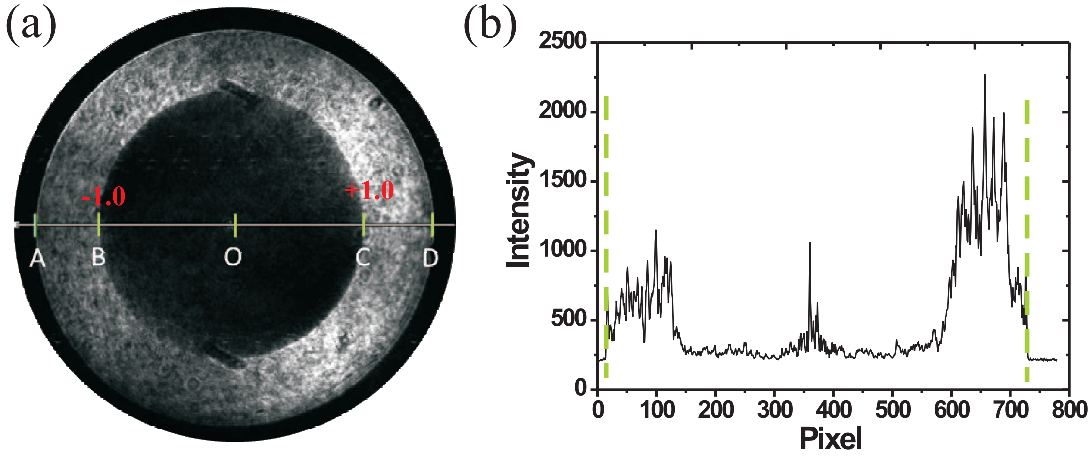

Fig 2.4: (a) Calibrating a Fourier plane. The line crosses the outer and inner edges of the annulus and the center at $A$, $B$, $O$, $C$ and $D$. The value at $C$ and $B$ corresponds to the critical angle $N_{crit}$=1.0. (b) The profile of the line in (a). The two vertical green lines indicate the pixel position of $A$ and $D$ defining the objective's numerical aperture.

The intensity profile of the Fourier plane is shown in Fig. 2.4(b) and is represented as a function of the number of pixels measured on the CCD chip. The two green vertical lines indicate pixels corresponding to position $A$ and $D$ on the outer edge of the annulus in Fig. 2.4(a). These two points are indicating the magnitude of the detectable wave vector $N_{eff}^{max}$ and are depending on the numerical aperture of the objective used. By moving the green vertical line in the profile, pixels corresponding to the center $P_O$ and the four points $P_A$, $P_B$, $P_C$ and $P_D$ were obtained.

Because defining the pixel of the circle center precisely is difficult, we use the ratio between the outer and inner diameter to calculate $N_{eff}^{max}$, then

$$N_{eff}^{max} = \frac{P_D - P_A}{P_C - P_B}. \tag{2.2}$$

The relay lenses are adjusted to obtain $N_{eff}^{max}$=1.49 corresponding to the known numerical aperture of the objective.

## 2.3 Results and discussions

### 2.3.1 Imaging SPP intensity and wave vector distributions

Wide-field optical imaging and a piezoelectric translation stage were used to position a nanowire extremity within the diffraction-limited focus of the inverted microscope. By optically exciting the Ag nanowire at one extremity with the focal spot, a bright emission spot is usually observed at the distal end indicating that light transport along the nanowire is taking place [45].

For thin nanowires, the effective index of the SPP mode is higher than the index of the substrate and light emission is only observed through a scattering process mediated by the end facets. Figure 2.5(a) shows the intensity distribution of a thin nanowire with diameter 90 nm. The image represents the intensity distribution measured by a CCD placed in the image plane of the microscope. The focal spot, exciting one end of the wire, appears as a saturated region in the image. Only a bright emission at the end of the wire is indeed observed.

For thicker wires however, the visualization of the SPP propagation becomes visible because the wave vector of the mode is contained inside the light cone of the substrate. Figure 2.5(b) displays this situation for a $L$=10 $\mu$m long wire with a diameter of $D$=320 nm. Leakage radiations of the surface plasmon mode propagating along the wire are visible in the form of two luminous lines located on either side of the structure. These lines are reminiscent of the intensity distribution at the edges of the pentagonal nanowire. The observation of these two parallel lines strongly relies on the precise adjustment of the objective correction collar. Interference fringes observed along the length of the nanowire are attributed to the imaging artifact due to the rotationally symmetric nature of the lenses. Similar fringes can be seen at the outer ring of the laser spot. The reference frame along the nanowire is defined as the $x$-axis. The profile of the cross-cut of the nanowire in Fig. 2.5(c) quantitatively shows the intensity distribution along the wire. The red dashed curve is the exponential fit yielding a propagation of $L_{SPP}$=3.0 $\mu$m. Comparing with the other imaging techniques introduced in chapter 1, our imaging technique can provide a direct view of intensity distribution and direct SPP decay length measurement for thicker nanowires. The SPP propagation length deduced from the exponential fitting of the image plane strongly depends on the fitting parameters and the level of noise and artefact contained in the image. Therefore, for all the nanowires measured in our experiments, the propagation lengths were deduced from Fourier plane analysis which yields

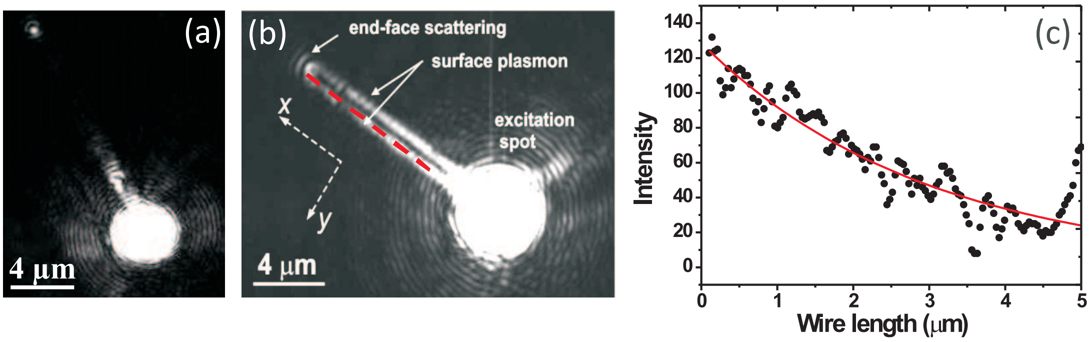

Fig 2.5: Intensity distribution of SPP mode supported by a thin and a thick nanowire. The excitation spot appears as a saturated area. (a) For a thin nanowire, only a bright light emission spot is observed at the end of the wire. (b) For a thick nanowire, the SPP mode along the wire and its scattering at the extremity are readily seen. The reference frame is taken along the nanowire ($x$-axis). (c) The intensity profile along the nanowire. The red curve is an exponential fit giving a propagation length $L_{SPP}$ =3.0 $\mu$m.

more consistent estimations of $L_{SPP}$.

A typical Fourier-plane image is displayed in Fig. 2.6. It represents the projected angular distribution on the plane of the interface. The SPP mode is recognized as a relatively bright line crossing the plane at $k_x/k_o = 1.05$, where $k_0 = 2\pi/\lambda$. The wave vector content along the perpendicular $k_y/k_o$ axis completely fills the detection window indicating a strong confinement along the $y$-direction expected due to the nature of this one-dimensional mode. Waves propagating in directions with angles beyond the critical angle of total internal reflection (forbidden-light region) are reflected and can't be observed in far field optics [168]. Two wave vector components out of the three have to be imaginary. Diffraction of SPP mode propagation along $x$ increases the incident spread of momentum along the $k_y/k_o$ axis [164]. The position of the bright line relative to the numerical aperture of the objective (1.49) and critical angle at $N_{crit} = 1.0$ is recognized as the effective index of the SPP mode $N_{eff}$ while the full-width at half-maximum (FWHM) of the line encodes the SPP losses and propagation length. No symmetric line at $-k_x/k_0$ = -1.05 indicative of a reflected mode at the end face was observed. The simulations in Ref. [144] suggests that when surface plasmons propagate in thicker nanowires, efficient scattering of the plasmon mode at the distal end is typical for nanowires with diameter greater than ~300 nm. This implies that the reflectivity is negligible. Figure 2.6 also shows a cross section of the Fourier plane along the $+k_x/k_0$ (red dots) is the free-space wave-vector. The distribution

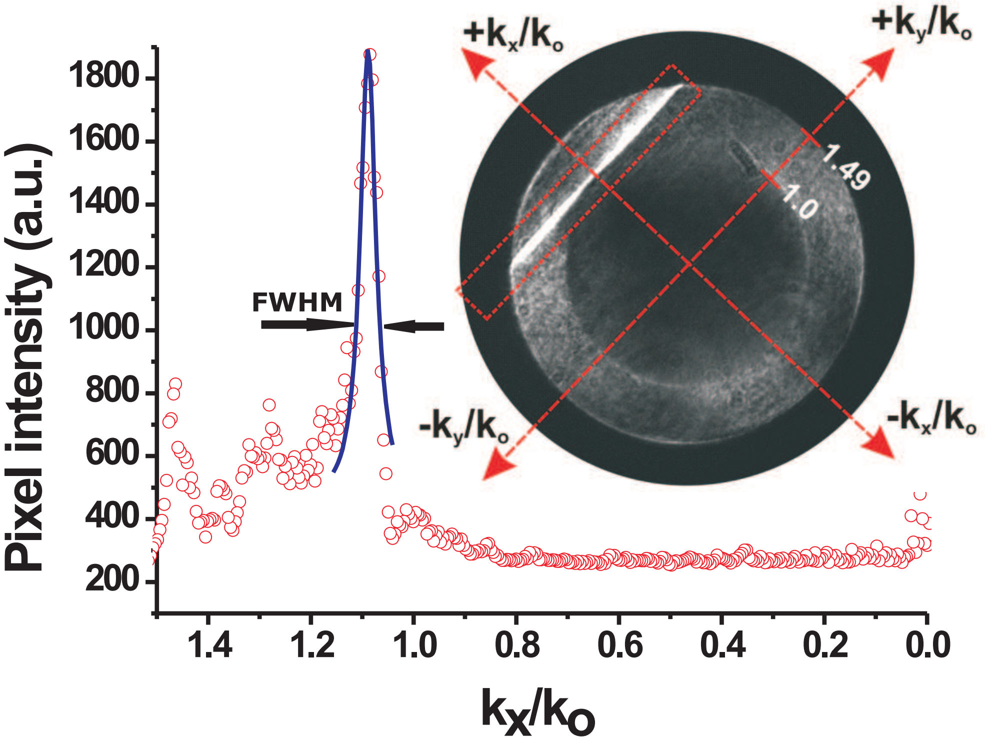

Fig 2.6: Wave vector distribution obtained by Fourier imaging. The SPP mode is recognized as a bright line at a constant $k_x/k_o$ value, here 1.05 (box). $N_{eff}^{max} = 1.49$ and $N_c = 1.0$ are given by the numerical aperture of the objective and the critical angle, respectively. A cross section along the $k_x/k_o$ axis is also displayed (red dots). The blue solid line is a Lorentzian fit to the data used to extract effective index of the SPP mode and its decay length.

around the bright line is accurately described by a Lorentzian curve [169] (blue solid line). It centres on the wave vector of the mode $N_{eff} = k_{SPP}$ and with a FWHM which is proportional to the propagation loss. The excited SPP mode in Fig. 2.6 exhibits a constant but unexpectedly low index at $N_{eff}$ =1.05, with a FWHM of 0.04 giving a propagation length of 3.2 $\mu$m according to the relation [148]:

$$L_{SPP} = 1/(k_o \times FWHM) \tag{2.3}$$

This propagation length is similar to the value deduced from the image plane in Fig. 2.5.

The nanowire described in Fig. 2.5 and Fig. 2.6 were both excited at wavelength 800 nm for a linear polarization oriented along the nanowire. Figure 2.7(a) and (b) display the wave-vector distribution in the Fourier images of the same nanowire at the same excitation position with a polarization parallel and perpendicular to the nanowire, respectively. We can see that when the excitation polarization is perpendicular to the nanowire, there is no signature of a plasmon mode in the Fourier plane. We recorded Fourier images as a a function of polarization orientation from 0° to 180° every 20°. The polarization along the nanowire is defined as 0°. The background corrected SPP intensity for each polarization is plotted in Fig. 2.7(c). The intensity is taken as the total count of the area of interest inside of the red box in Fig. 2.7(a). Since there is no SPP mode appearing on the Fourier plane at the excitation polarization perpendicular to the nanowire, it is taken as the background. The intensity curve shows a sinusoidal evolution with minimum intensity at 90° and maximum at 0°.

### 2.3.2 Selecting SPP modes by polarization inhomogeneity

In our measurements, an efficient coupling of surface plasmon was achieved by precisely focusing the laser beam on the end of a nanowire with a polarization usually aligned along the nanowire (Fig. 2.7(c)). However, we also found that depending on the precise alignement of the nanowire in the focus, the nature of the excited SPP mode, bound or leaky, could be precisely selected. Figure 2.8 shows leakage radiation images of the same nanowire excited with a linear polarization along the main axis at two slightly different locations within the focus. In Fig. 2.8(a), the light is predominantly coupled to a leaky SPP mode whereas in Fig. 2.8(b), only a signal scattered at the extremity is recorded suggesting the excitation of bound mode with an effective index $N_{eff}$ >N.A. The corresponding Fourier image in Fig. 2.9(a) displays a bright bar indicating the excitation

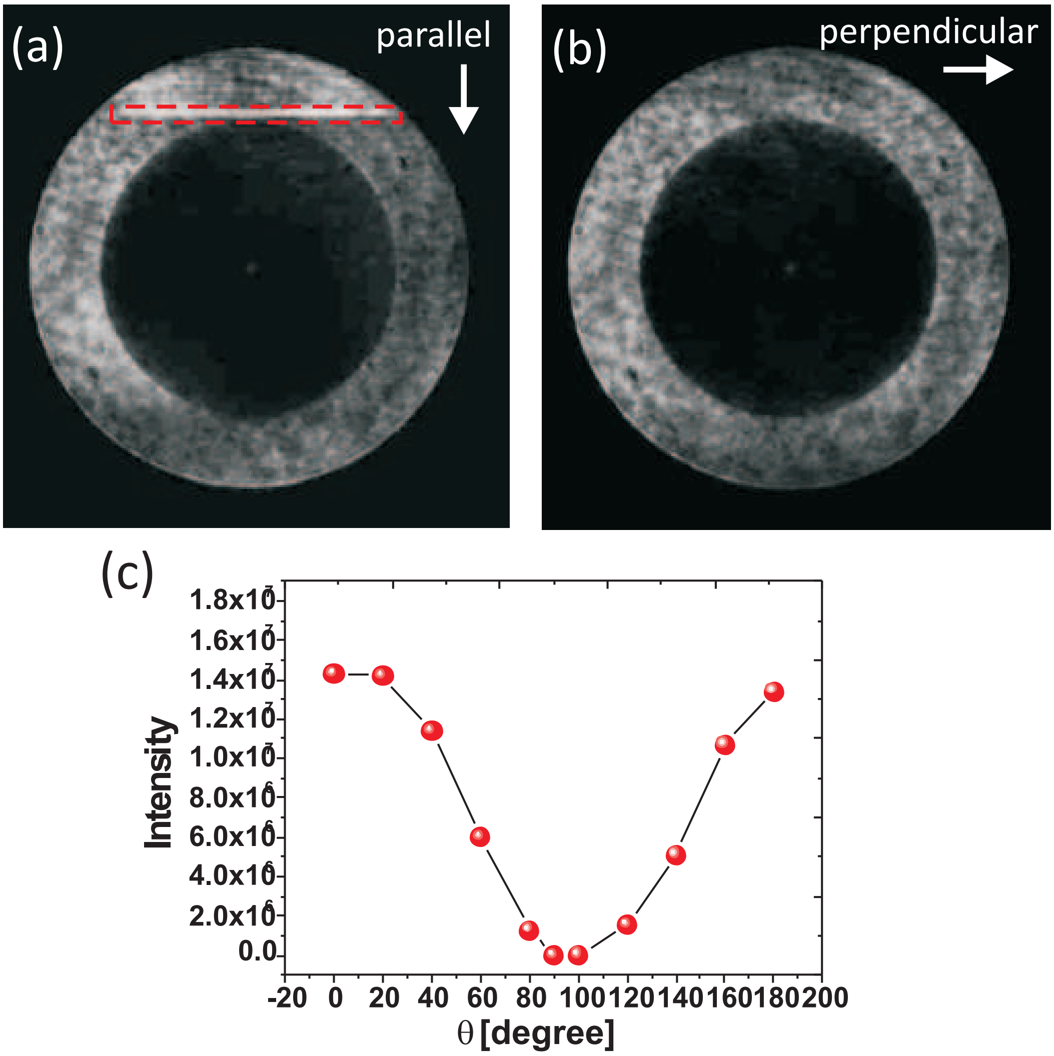

Fig 2.7: Wave vector intensity distribution obtained by Fourier imaging of a nanowire for an linear polarization parallel (a) and perpendicular (b) to the long axis of the wire. (c) Background corrected intensity of SPP on Fourier plane for different excitation polarizations from 0° to 180°. It shows a sinusoidal shape with intensity minimum at 90° and maximum at 0°. 0° is defined as the polarization along the long axis of the nanowire. The red box shows the area of interest used to determine the intensity.

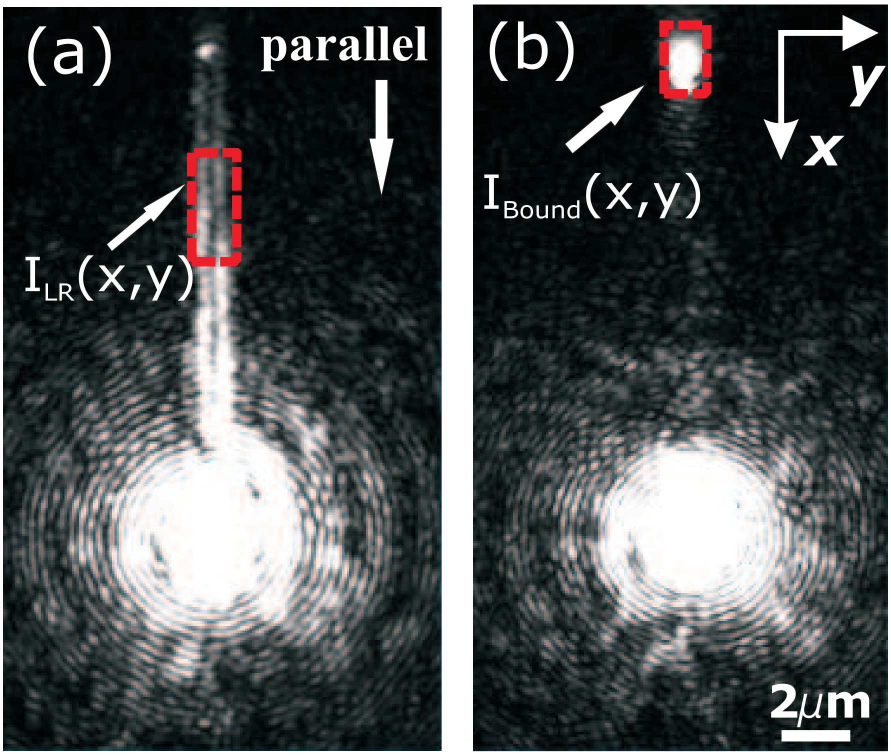

Fig 2.8: Leakage radiation images of a Ag nanowire excited with polarization along the nanowire. Depending on the precise position of the coupling extremity inside the focal spot, leaky mode (a) or bound mode (b) can be selectively excited. The intensity of the two modes was extracted from the red boxes.

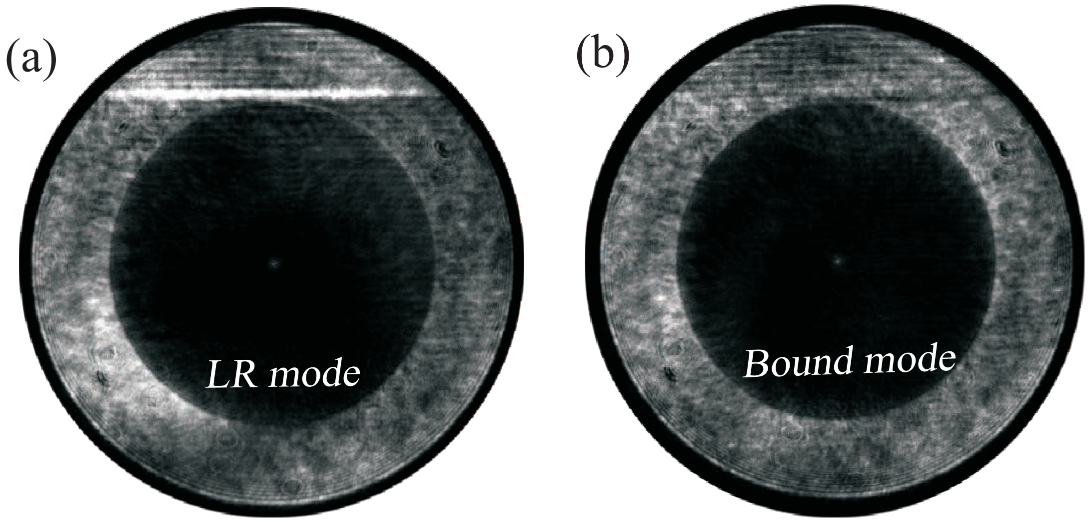

Fig 2.9: Fourier images of the leaky mode (a) and bound mode (b). When the bound mode is excited, there is no information of surface plasmon mode detectable in the Fourier plane image.

of leaky mode while for the bound mode, there is expectedly no information detectable in the Fourier image (Fig. 2.9(b)).

We hypothesize that the excitation of the two modes are selected by the polarization inhomogeneity playing inside a tightly focused beam. To test this assumption, we laterally scanned the nanowire through the focus laser beam for two orthogonal polarizations.

First, the position of nanowire was manually adjusted with respect to the laser focus spot to have an efficient excitation of the leaky mode with a polarization oriented along the nanowire. This position was then taken as the center of the scanning area. The 3D confocal image in Fig. 2.10(a) shows the Rayleigh scattering issued from the nanowire with a scanning size of 25 $\mu$m along the long axis of the nanowire. This image represents the laser signal backscattered at the interface and detected by an avalanche photodiode (APD) placed at a conjugated image plane (confocal). In the absence of a nanowire, the count rate measured by the APD is equivalent to the integrated intensity recorded in the Fourier plane of Fig. 2.4. Figure 2.10(b) shows a 5$\mu$m$\times$5$\mu$m zoom in at the termination

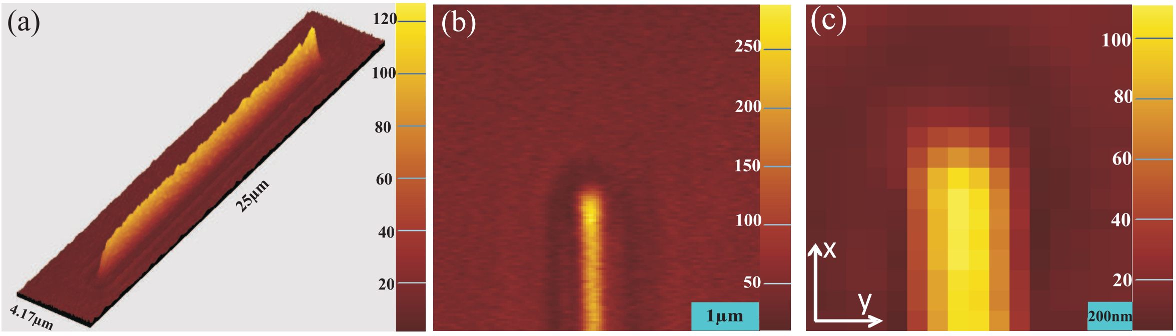

Fig 2.10: Confocal image of a Ag nanowire with different scanning size: (a) 3D image with a scan range of 25 $\mu$m×4.17 $\mu$m, (b) 5 $\mu$m×5 $\mu$m and (c) 1.5 $\mu$m×1.5 $\mu$m. The fast scanning direction is along $y$ axis. $\lambda$=810 nm.

of the nanowire. Then we scanned the end of the wire with small area of 1.5 $\mu$m×1.5 $\mu$m consisting of 16×16 pixels shown in Fig. 2.10(c). The fast scanning direction is along $y$ axis.

The CCD cameras were then synchronized to the scanner with a hand-shaking protocol so that an image plane and an Fourier plane were simultaneously acquired for each pixel of Fig. 2.10(c). A series of 16×16 images similar to Fig. 2.8 and Fig. 2.9 were thus obtained and analyzed.

By extracting the SPP intensity along the nanowire or at its extremity as illustrated by the red boxes in Fig. 2.8, excitation maps for the leaky mode and bound modes can be reconstructed. The excitation maps of the two modes for a polarization perpendicular to the nanowire are shown in Fig. 2.11. The leaky mode is preferentially excited following a four lobe pattern while the bound mode is essentially excited by two areas in the focal spot. There is very little spatial overlap between the two reconstructed maps suggesting that modes can be efficiently selected by the position of the extremity inside the focal region.

Interestingly, the excitation maps are resembling of the intensity distribution of individual field components inside a tightly focused laser beam in the focus plane ($z$=0). The calculated intensity distributions of an $y$-polarized focused beam (polarization perpendicular to the wire) and its individual field components $|E_x|^2$, $|E_y|^2$, $|E_z|^2$ are displayed in Fig. 2.12. The field maps were calculated by scanning a dipole oriented along the $x$, $y$, or $z$ axis at a wavelength of 800 nm and objective with N.A.=1.49. The size of the calculated window is the same as the the scan size in Fig. 2.10(c). The $|E_y|^2$ field

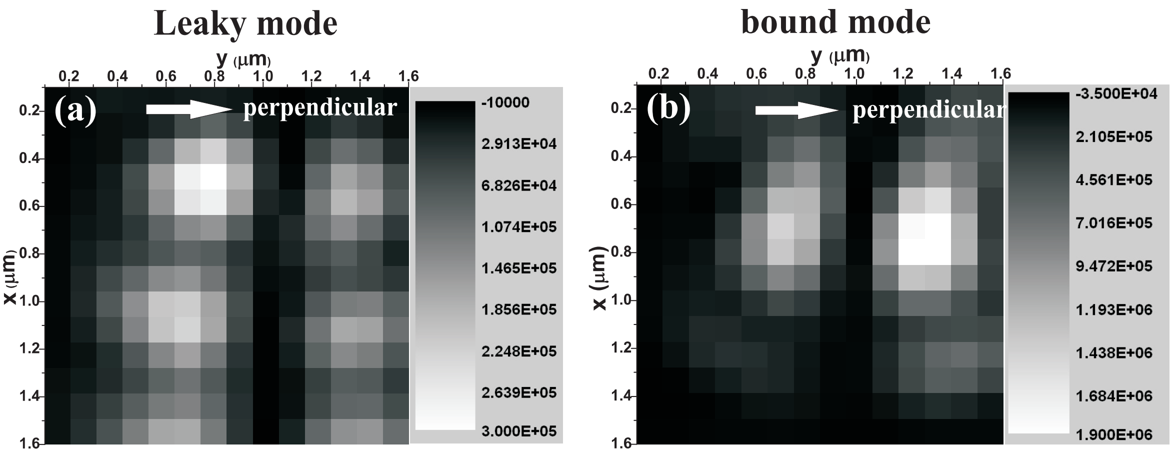

Fig 2.11: Reconstructed excitation maps for (a) leaky mode and (b) bound mode for polarization perpendicular to the wire. The intensity was extracted the red boxes shown in Fig. 2.8.

component which locates at the polarization direction possesses the maximum field intensity $\sim 5\times10^8$. Then maximum intensity ratio between the $|E_y|^2$ component and $|E_x|^2$ component is approximately 30 while the ratio between $|E_y|^2$ and $|E_z|^2$ is approximately 10.

The four lopes of the leaky mode in Fig. 2.11(a) are very similar to the intensity distribution of $|E_x|^2$ field component. In these regions of the focus, the field is depolarized from the main polarization, and for this particular case is aligned along the nanowire. The two lobes in Fig. 2.11(b) shows similarity with the intensity distribution of $|E_z|^2$ field component. The resemblance between the reconstructed excitation maps and the polarization inhomogeneity of the focal fields strongly suggest that the modes existing in a nanowire can be selected by different field components. The fields aligned along the nanowire are preferentially coupled to the leaky mode while out-of-plane field components are required to excite bound modes. This antisymmetric polarization nature of surface plasmon mode was also investigated in Ref. [82]. Bound surface plasmon modes in nanowire were excited by adiabatic mode transformation along a Au strip. The plasmon mode at the glass/air interface was first excited through a hold array made in the Au film using 1550 nm light. Surface plasmon propagating along the tapered stripe at the glass/gold interface can couple to the bound nanowire. The evanescent SPP field is probed above the sample with a phase-sensitive near-field microscope. The collected signal is interferometrically mixed with a reference signal [170]. Thus, the detected complex signal consisting of both the local field amplitude and the phase which is a projection of

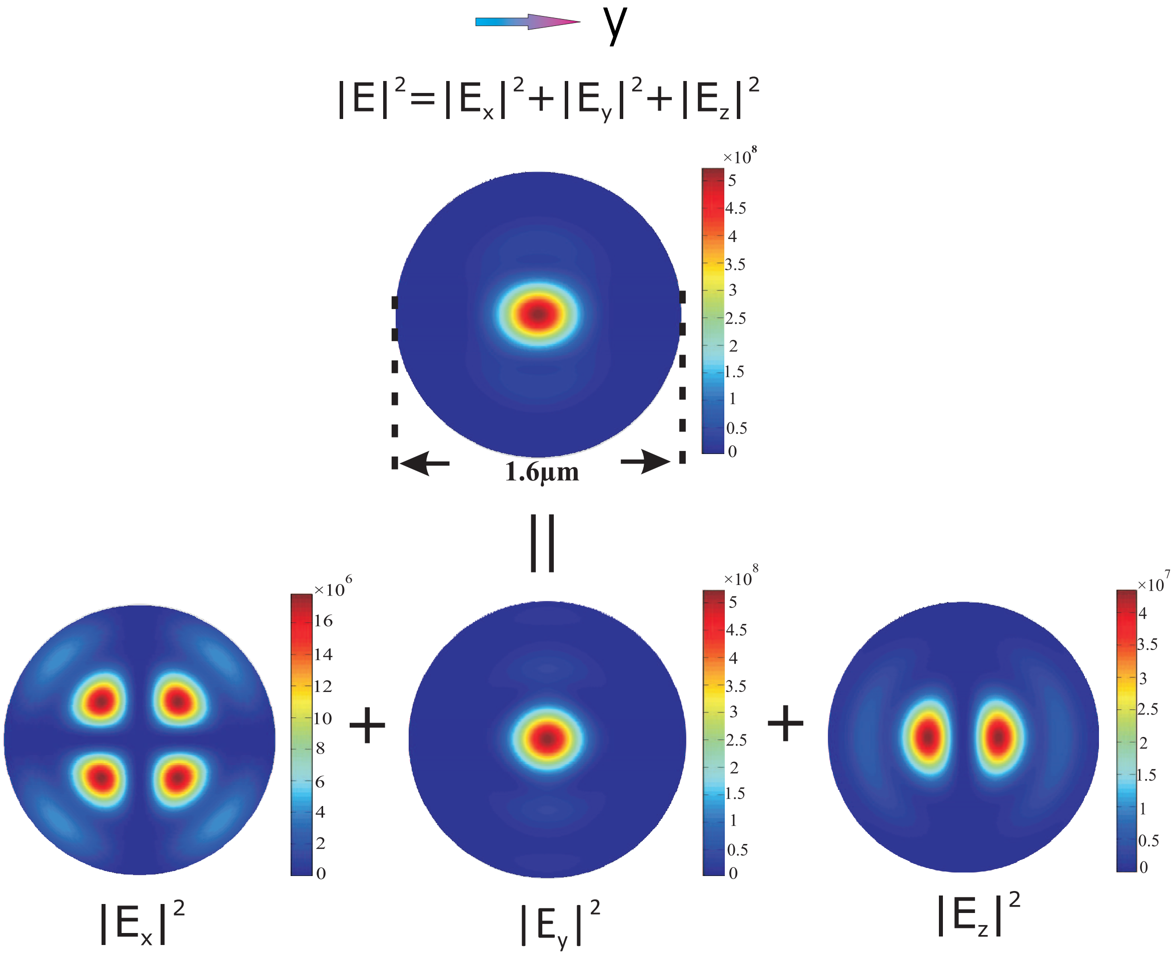

Fig 2.12: Polarization components inside a tightly focused $y$-polarized beam. The intensity distributions of individual field component $|E_x|^2$, $|E_y|^2$, $|E_z|^2$ in the focal plane were computed by exciting an $(x, y, z)$ oriented dipole at a glass/air interface at $\lambda$ =800 nm.

the vectorial near field on the polarization state of the reference beam. The contribution of $x$ and $y$ near-field components of the orthogonal polarizations coupled in the probe fiber to the detected signal can be found by selecting the polarization of the reference beam in the signal transport direction. Their results suggest that the in-plane optical field component along the nanowire provides the dominant contribution to the propagating plasmon mode which agrees well with our observations. However comparing to the technique used in Ref. [82], our approach is much easier to perform and more selective for the different plasmon modes.

### 2.3.3 Wave vector analysis

**Effective index**

The wave vector distributions of the measured nanowires were analyzed from the recorded Fourier plane images (Fig. 2.6). By using a Lorentzian fitting of the Fourier plane along the $+k_x/k_0$ for all the wires excited at 800 nm (total of 40), we obtained the distribution of effective indices shown in Fig. 2.13 in the detection range from 1.0 to 1.49. We can see that for this excitation, the effective indices mainly distribute between 1.04 and 1.08.

The measured effective index is very close to the value of the critical angle 1.0. However, the effective index of Ag nanowires with diameter range from 50 nm to 300 nm on silica substrate reported in Ref. [152] is above 1.4 which is much higher than our measured value.

Therefore, we numerically investigated these unexpected low values of the effective index. Since the high-resolution SEM image in Fig. 2.1 exhibits a pentagonal cross section of the nanowires, numerical simulations were carried out by considering a pentagonal shape to follow the experimental conditions. The different modes existing in a pentagonal Ag nanowire were computed using COMSOL Multiphysics (RF module) and were cross-checked with a home-made mode solver based on Green's dyad computation [169, 171]. The later can easily treat leaky modes in the presence of a substrate.

We first considered infinitely long (2D) metallic nanowires with a pentagonal cross section of various diameters embedded in a homogeneous background of optical index $n$ =1.25 that roughly mimics the glass ($n$=1.5)/air ($n$=1) interface. COMSOL Multiphysics software is based on finite element method so that both the nanowire and its surroundings need to be discretized. We used a circular computational window (between 1.5 and 10 $\mu$m) large enough to ensure convergence within a reasonable computing time and imposed perfect electric conductor conditions at its boundary. The whole geometry

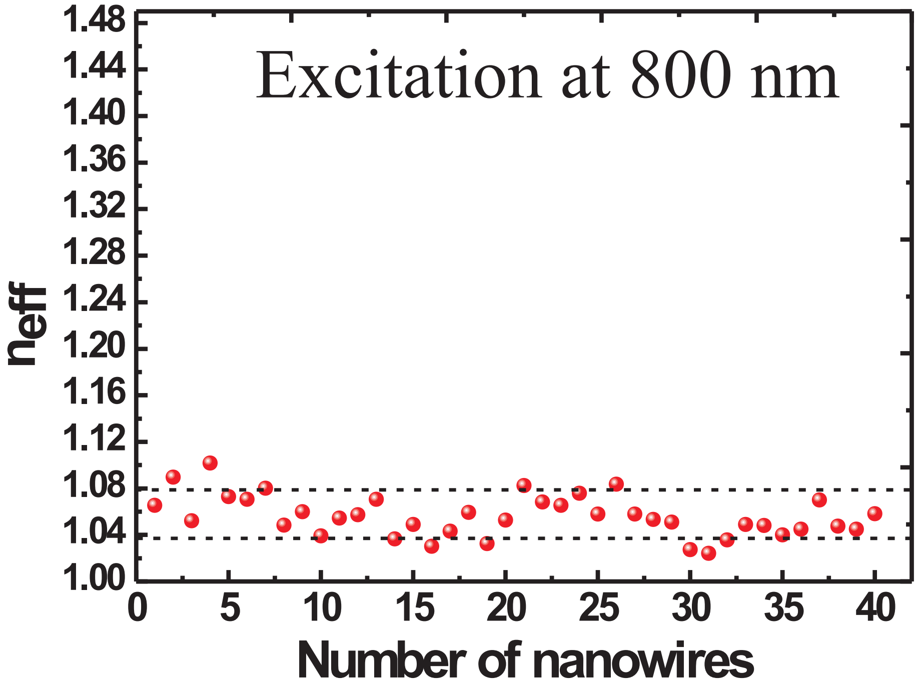

Fig 2.13: Distribution of measured effective index for 40 nanowires excited at 800 nm in the $N_{eff}$ range from 1.0 to 1.49.

(nanowire and surroundings) was discretized using between 20000 and 60000 triangular meshes.

For the home-made mode solver based on 2D Green's dyad computation, it only necessitates discretization of the metallic wire so that the infinitely extended surrounding is naturally taken into account. We used rectangular meshes and cross-checked the obtained effective indices with the values obtained using COMSOL software. The two mode solvers give access to a complex effective index of the guided mode, $N_{eff} = N^{'}_{eff} + iN^{''}_{eff}$.

Pentagonal nanowires support five modes resulting from a coupling of corner modes which were simulated by using an excitation wavelength $\lambda$ =800 nm and a silver optical index $n_{Ag} = 0.0362 + i5.4$. The intensity profile of an isolated silver corner with angle 108° is displayed in Fig. 2.14(a). The effective index of this corner mode is 1.303. The field is maximum at the crest of the corner. The guided modes of a pentagonal nanowire can be described as a linear combination of five corners modes. The intensity distribution of the calculated guided modes for a nanowire with diameter 1.25 $\mu$m are shown in Fig. 2.14(b). The fundamental mode shown at the bottom of Fig. 2.14(b) with effective index (1.316) has the same intensity distribution of its five corners. The other four modes with different intensity distribution are separated into two groups of degenerated modes with effective index 1.306 and 1.277, respectively. The five modes display a $D_{5h}$ symmetry.

Interestingly, the guided modes displayed in Fig. 2.14(b) are strictly analogous to the molecular orbitals of another $D_{5h}$ system, the cyclopentadienyl molecule. When the five corners combine to form a pentagonal section, this interaction creates mode symmetries in analogy with the molecular orbitals. The molecular orbitals of the $\pi$-bonds of cyclopentadienyl, deduced from simple Huckel theory, are shown in Fig. 2.15. Following the conventional representation of molecular orbitals, the weight and relative signs of the atomic orbital in the representation are depicted by the circle area and color (white = positive, black = negative), respectively; $\alpha$ is the energy of an isolated atomic orbital and $\beta$ refers to the coupling strength between orbitals of two adjacent carbon atoms. $a^{''}_2$ and $e^{''}_1$, $e^{''}_2$ are the corresponding Mulliken's symbols, where $a$ represents the symmetric solution with respect to a rotation around the principal rotational axis (one dimensional representation), $e$ represents degenerate mode (two dimensional representations), prime (') and double prime (") represent the symmetric and antisymmetric mode with respect to a mirror plane horizontal to the principal rotational axis. By analogy with the intensity distribution in Fig. 2.14(b) and the molecular orbital configuration, the symmetry groups were assigned to the plasmon modes.

The dispersion curves of the five bound modes as a function of the nanowire diameter

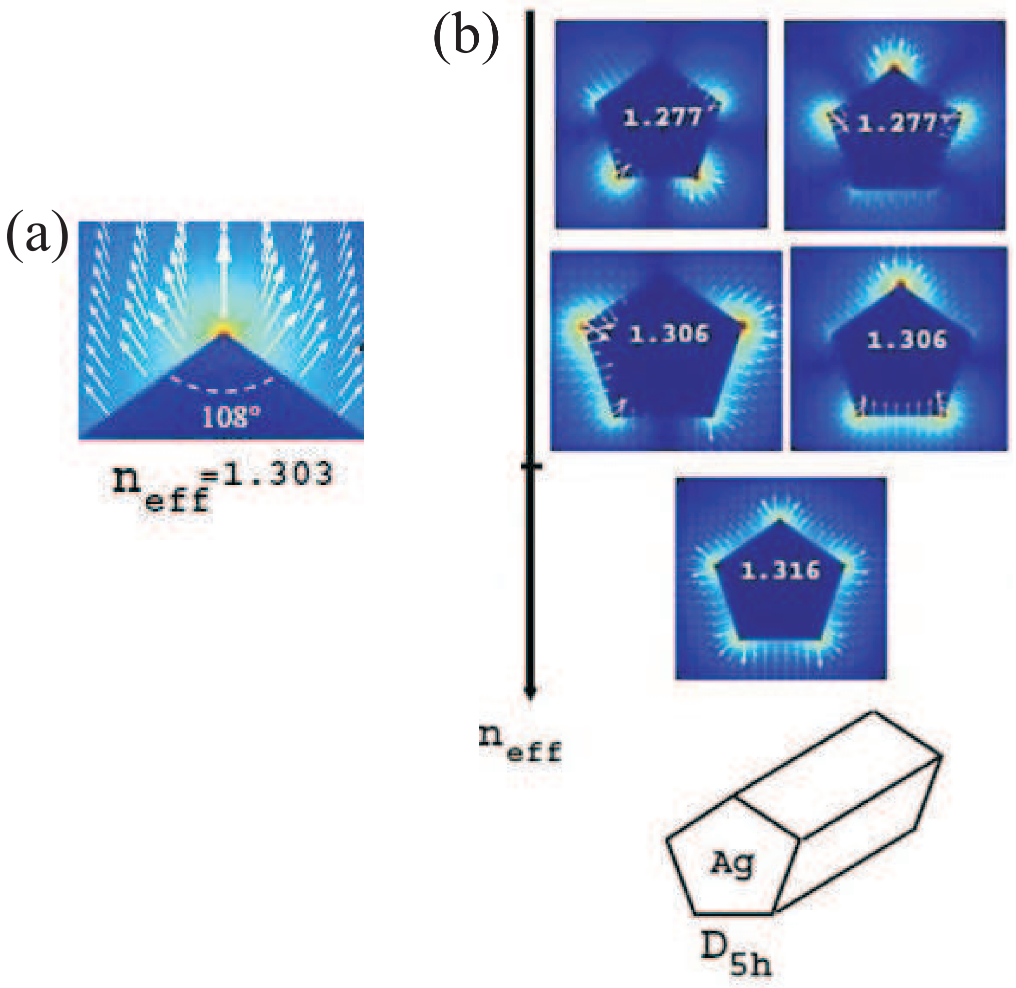

Fig 2.14: (a) Calculated intensity profile of an isolated silver corner. (b) Five modes formed by a linear combination of the five corner modes: fundamental mode and two groups of degenerated modes. The five modes display an $D_{5h}$ symmetry. The wire diameter is 1.25 $\mu$m embedded in a medium of optical index $n$ =1.25.

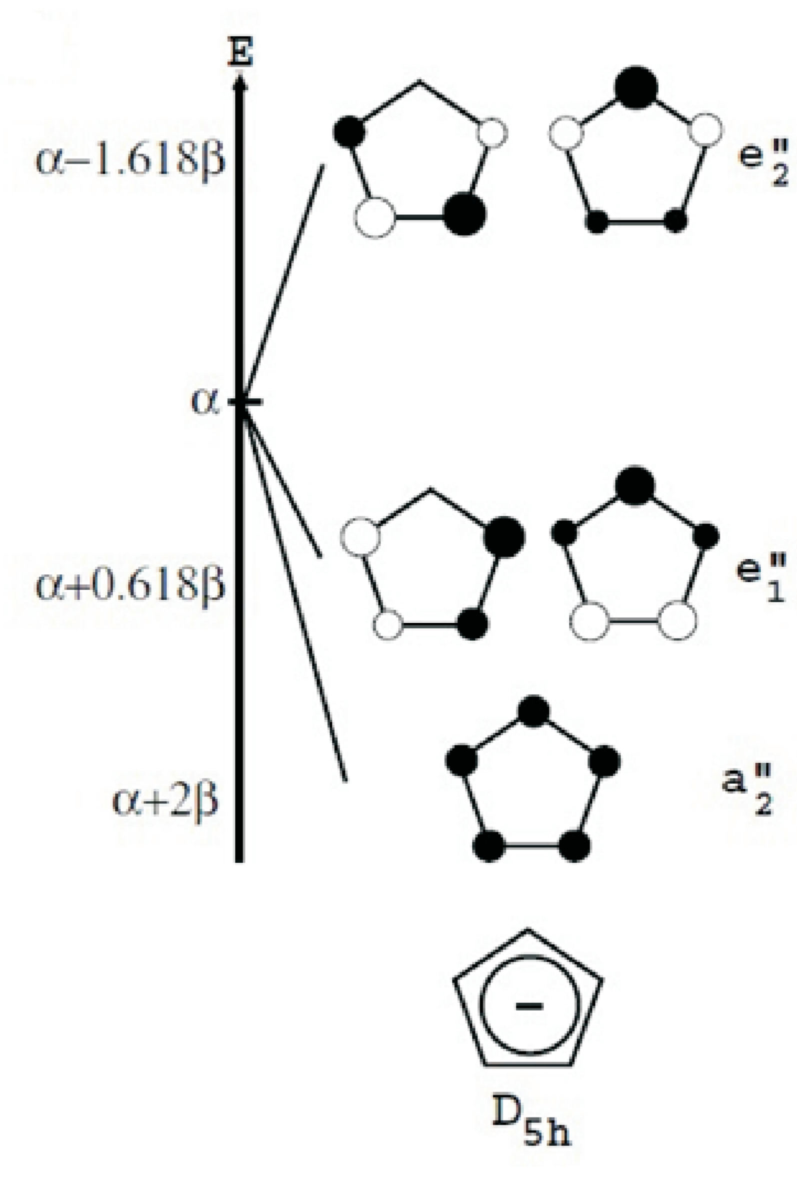

Fig 2.15: Schematic of the orbital configuration of a molecule displaying a $D_{5h}$ symmetry. The weight and relative signs of the atomic orbital are depicted by the circle area and color (white = positive, black = negative); $\alpha$ is the energy of an isolated atomic $\pi$ orbital and $\beta$ (<0) refers to the coupling strength between orbitals of two adjacent carbons. $e_2^{''}$, $e_1^{''}$ and $a_2^{''}$ are the corresponding Mulliken's symbols.

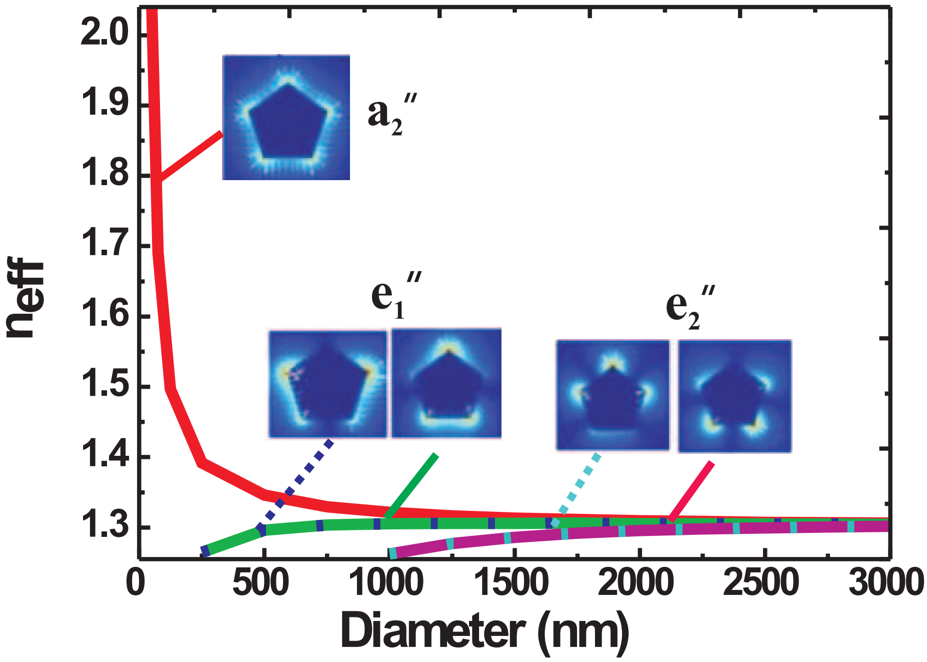

Fig 2.16: Dispersion of the effective index of the identified modes as a function of nanowire diameter. The fundamental mode diverges for thin nanowires. The higher-order modes exhibit a cutoff behaviour when their effective indices approach the refractive index of the surrounding medium (1.25).

are displayed in Fig. 2.16. We can see that the radial fundamental mode has no cut-off. This is similar to the fundamental $TM_0$ mode of a circular metallic nanowire featuring a divergent effective index for low diameters. The four other guided modes separates in two groups of degenerated modes $e_2^{''}$ and $e_1^{''}$ characterized by low effective indices close to the surrounding medium (1.25). These modes run into cut-off at a diameter of about 850 nm and 150 nm, respectively. Due to their large cut-off diameter, the two degenerated highest modes $e_2^{''}$ are not of interest for the diameter experimentally investigated and will not be considered further.

The experimental values of the effective index of the SPP mode ($N_{eff} \sim 1.05$) are significantly lower than the effective indices calculated for a homogeneous medium. For a nanowire with diameter 250 nm in homogeneous background, the effective index of

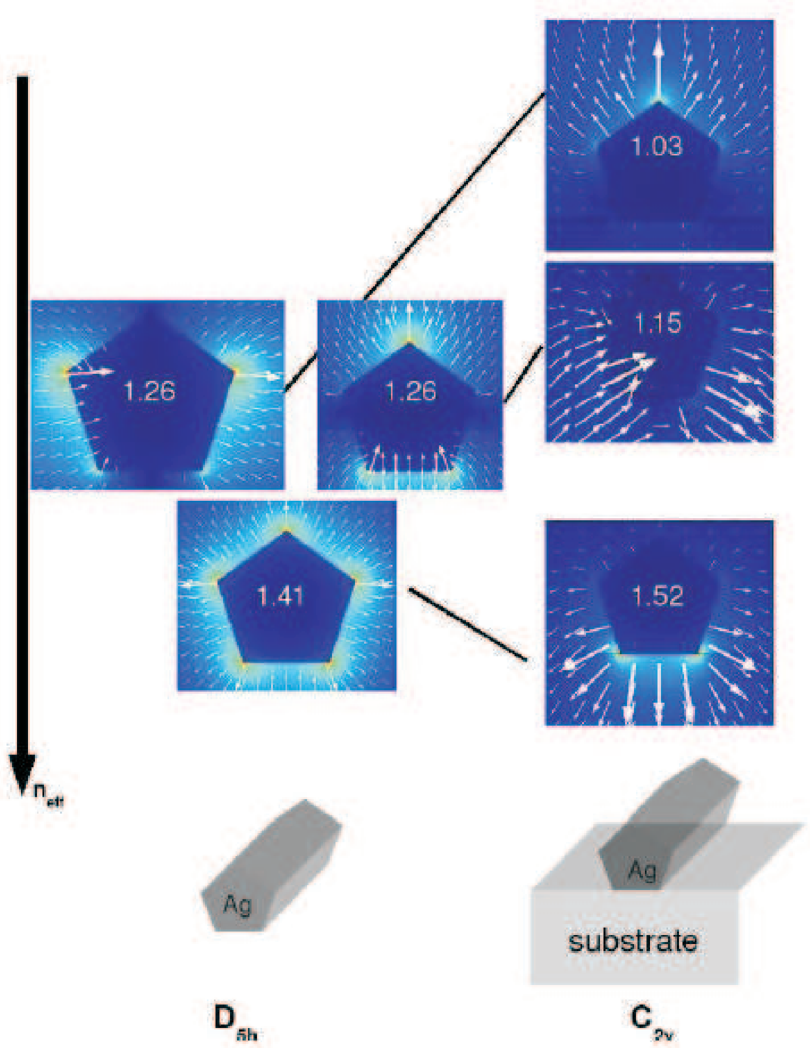

Fig 2.17: Effect of the substrate on the intensity distribution and effective indices of the SPP guided modes supported by a pentagonal silver nanowire. The group symmetry is reduced from $D_{5h}$ to $C_{2v}$ so the two degenerated modes at $N_{eff}$ =1.26 are evolving into two distinct modes at $N_{eff}$ =1.03 and 1.15. The intensity level for the $N_{eff}$ =1.15 mode is significantly weaker than the more pronounced $N_{eff}$ =1.03 mode, suggesting that this mode is inactive. The nanowire diameter is 200 nm.

fundamental mode is 1.39 while for the other two degenerated modes it is at 1.26. In order to account quantitatively for this observation, we introduce the glass substrate in our model. To closely follow the experimental geometry and limit numerical difficulties, the pentagon corners were rounded with a radius of curvature of 5 nm. Although time-consuming, Green's dyad method easily takes into account leaky modes existing in this configuration. On the contrary, investigating leaky modes using COMSOL software is a difficult task since a perfectly matched layer (PML) was included to avoid field reflections at the computational window boundaries. Therefore, we used the Green's dyad method to evaluate the effective indices of leaky modes for typical nanowire diameter and then determined the optimal PML parameters (thickness and position) required in COMSOL software to ensure convergence. The sample symmetry is then reduced from $D_{5h}$ to $C_{2v}$, and the modes are no longer degenerated as shown in Fig. 2.17.

The fundamental mode remains a bound mode ($N_{eff} > 1.5$), with the field confined in the high index medium (substrate). The two other modes at $N_{eff} = 1.03$ and $N_{eff} = 1.15$ become leaky into the substrate ($N_{eff} < 1.5$) and could therefore be detected using our leakage radiation microscope setup. However, in all of the nanowires that were excited at 800 nm, we have only detected the low effective index mode and were not able to measure the mode expected at $N_{eff}$ =1.15. We attribute this to a low excitation cross section since this mode appears to be extremely weak in the numerical simulations.

The calculated effective index $N_{eff}$ of plasmon mode was compared with our experimental data. For the sake of comparison, $N_{eff}$ of six nanowires with similar lengths (4.8 $\mu$m$< L <$ 5.5 $\mu$m) were plotted as a function of diameter in Fig. 2.18(a). Within the considered diameter range 100 nm $< D <$250 nm, the dispersion is almost flat at $N_{eff}$ around 1.05. The FWHM of the mode, which is proportional to the calculated imaginary part $N''_{eff}$ encoded in the error bar is almost constant. The calculated data (open circles) confirm that the effective index is not significantly affected by the diameter of the nanowire in the considered range. A small discrepancy between the experimental and calculated data remains and can be attributed to the dielectric constant used, the presence of the PVP polymer on the surface of the nanowire, and experimental errors in calibrating Fourier planes.

The effect of nanowire length on the effective index was also investigated. For the sake of comparison, a restricted range of wire diameter comprised between 147 nm and 159 nm is selected. In Fig. 2.18(b), $N_{eff}$ value and FWHM are plotted for different nanowire lengths. The effective index is almost constant within the considered length range. In contrast, the mode FWHM represented by the error bars is reduced when the length of

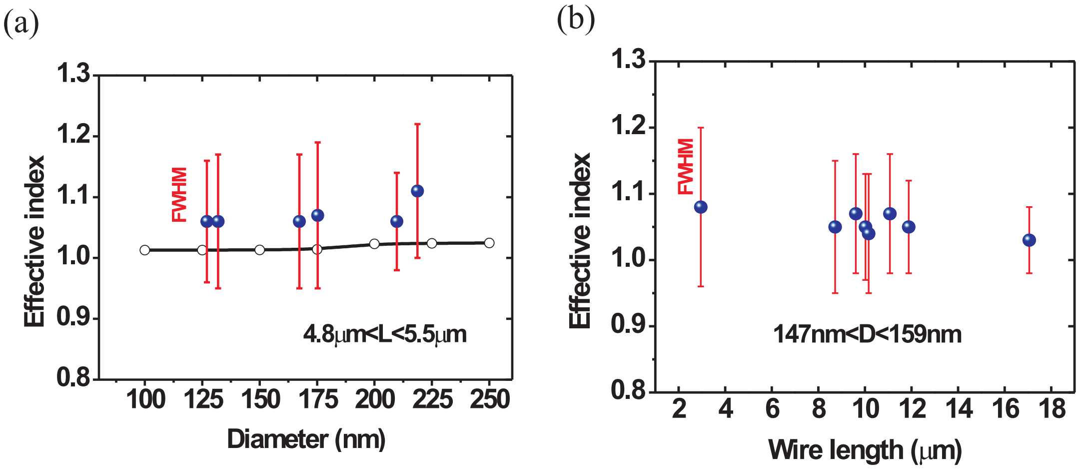

Fig 2.18: (a) Comparison of $N_{eff}$ between the experimental and calculated data for wires with diameters in the range of 100 nm< $D$ < 250 nm . The experimental data points are shown with filled circles and calculated data are with open circles. (b) Effective index as function of length. The data points are for nanowires with a restricted range of diameters 147 nm < $D$ <159 nm. The error bars represents the FWHM of the line measured in the Fourier plane or equivalently $N''_{eff}$.

the wire is increased. Compare to the effective index in Fig. 2.18(a), the effective indices in both figures are almost around the same value 1.05. Therefore, we can conclude that the effect of wire length on the effective index can be ignored. The measured effective index is in good agreement with the calculated mode.

### Propagation length

Figure 2.18(b) indicates that the length of the nanowire is affecting the SPP decay length. Since the SPP is efficiently scattered at the nanowire distal tip as shown in Fig. 2.5, the effect of the nanowire length on the FWHM of the mode measured in the Fourier plane should be considered. The propagation length of the SPP mode can be directly inferred from the measure of the FWHM using the relation in equation 2.3. The inferred propagation length from Fig. 2.18(a) and Fig. 2.18(b) are shown in Fig. 2.19(a) and Fig. 2.19(b), respectively. The propagation length in Fig. 2.19(a) is almost constant with the increase diameter in our considered range while in Fig. 2.18(b), it shows apparent increase with wire length. Distal face scattering is therefore playing a determinant role by introducing an additional decay mechanism, predominant for short nanowires.

The calculated dispersion of the propagation length $L_{spp}$ of the identified modes for nanowires in homogeneous background is shown in Fig. 2.20(a). Close to their cut-off

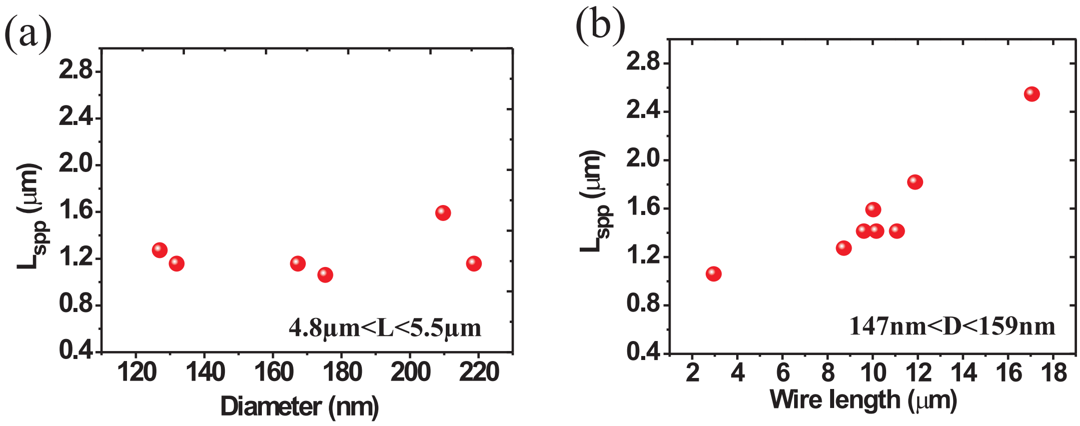

Fig 2.19: Propagation length as a function of diameter (a) and length (b) inferred from Fig. 2.18(a) and Fig. 2.18(b), respectively. The error bars are contained within the size of the dots.

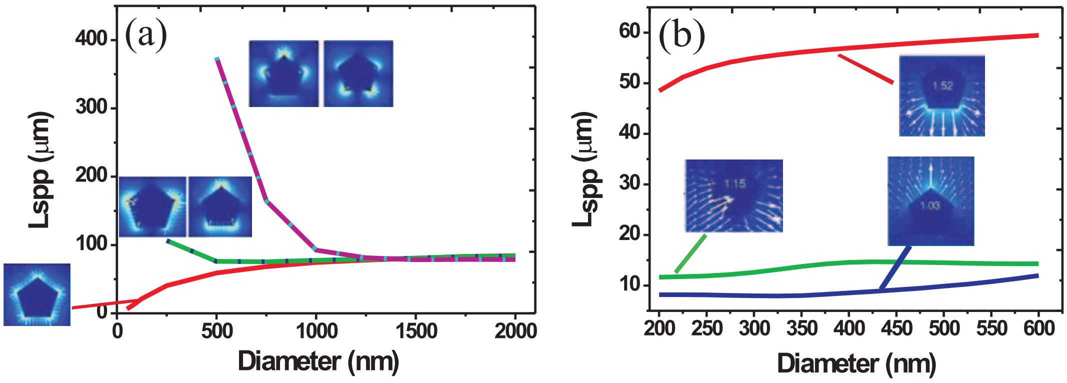

Fig 2.20: Calculated propagation length as a function of wire diameter. (a) Nanowire in a homogeneous background. The fundamental mode exhibits a high damping for small diameters due to its diverging effective index. (b) Nanowire on a substrate. The introduce of substrate strongly modifies the propagation length of the two degenerated modes.

conditions, these modes have a significant longer propagation length because their field spread more in the medium and are thus less plagued by Joules losses. Exciting SPP mode under this condition might be suitable for short-scale optical interconnects at the expense of tight confinement. When the substrate is introduced in the calculation, the propagation length of fundamental mode is only slightly modified as shown in Fig. 2.20(b). Take a 200 nm diameter nanowire as an example, it increases from $L_{spp}$ =34 $\mu$m in a homogeneous background of optical index $n$ =1.25 to $L_{spp}$ =48 $\mu$m for a glass/air interface. However, in addition to the degeneracy lift, the presence of the substrate strongly modifies the propagation of higher-order modes. For a 200 nm nanowire $L_{spp}$ is reduced from 209 $\mu$m to $L_{spp}$ =11.6 $\mu$m ($N_{eff}$ =1.15) or $L_{spp}$ =5.3 $\mu$m ($N_{eff}$ =1.03). The presence of the substrate introduces a new decay channel through radiation leakage, impacting thus the propagation length. In the experiment, a nanowire with diameter 209 nm, length 5 $\mu$m has a propagation length $L_{spp}$ = 1.6 $\mu$m ($N_{eff}$ =1.06). It is significantly shorter than the calculated value. Since the SPP propagation is length dependent, the difference between the finite nanowire length in the experiment and the infinitely long structure assumed in the numerical simulation may explain the experimentally shorter $L_{spp}$. Additionally, the reasons evoked for explaining the discrepancy of effective indices will also contribute to shorten the propagation length.

### 2.3.4 Different wavelength excitations

To investigate the effect of excitation wavelength on the effective indices and propagation lengths, nanowires were also excited at 532 nm. The effective indices are compared with that of SPP mode at 800 nm excitation. The histograms of effective indices at the two excitation wavelength are shown in Fig. 2.21. The effective index for an excitation at $\lambda$=532 nm mainly distributes between 1.11 and 1.13, values higher than the effective indices measured at $\lambda$=800 nm. This can be explained by the bending of the SPP dispersion relation toward higher wave vectors for increasing excitation frequencies [81]. An increased excitation wavelength leads to a smaller SPP wave vector and thus a lower effective index.

The effect of nanowire diameter and length on the effective index is described in Fig. 2.22. Likewise, for the sake of comparison, effective indices of nanowires with similar lengths (3.1 $\mu$m < $L$ <3.8 $\mu$m) were plotted as a function of diameter in Fig. 2.22(a). The effect of nanowire length was plotted in Fig. 2.22(b) by selecting nanowires with similar diameter (155 nm < $D$ <194 nm). In both graphs, the effective indices are almost

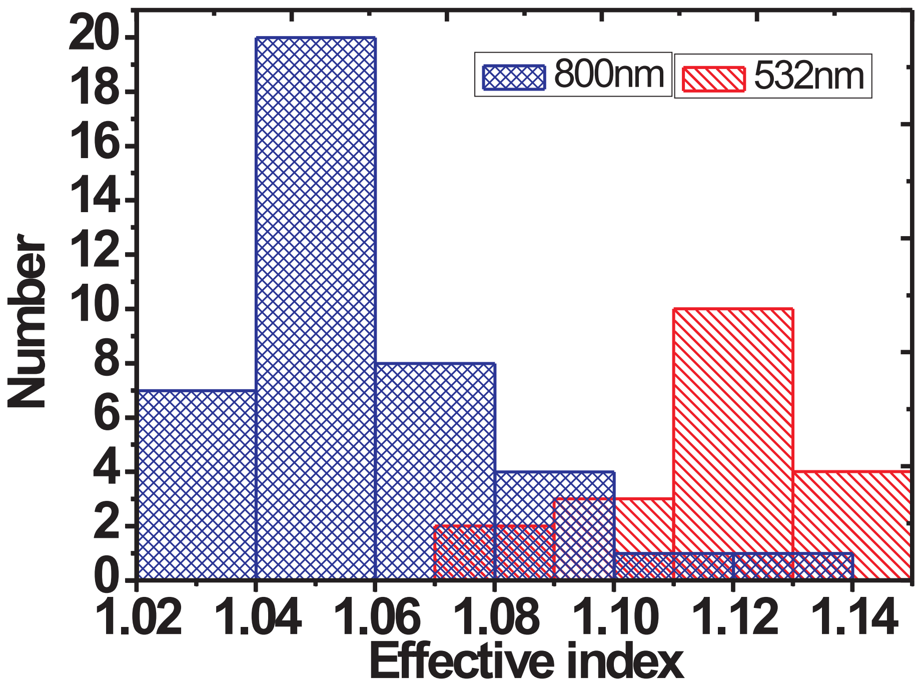

Fig 2.21: Histogram of effective index for a 532 nm excitation (red), and a 800 nm excitation (blue).

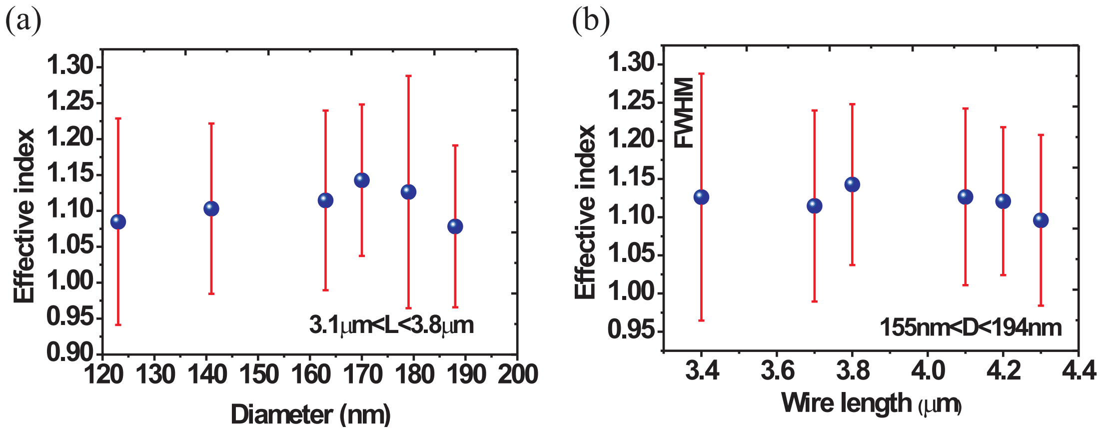

Fig 2.22: (a) Dispersion curve of the detected mode with nanowire excited at 532 nm. The effective index and FWHM were extracted from Fourier images for nanowires with similar length 3.1$\mu$m $< L <$3.8$\mu$m. The FWHM is encoded in the error bars. (b) Effective index as function of length for nanowires with a restricted range of diameter 155 nm $< D <$194 nm.

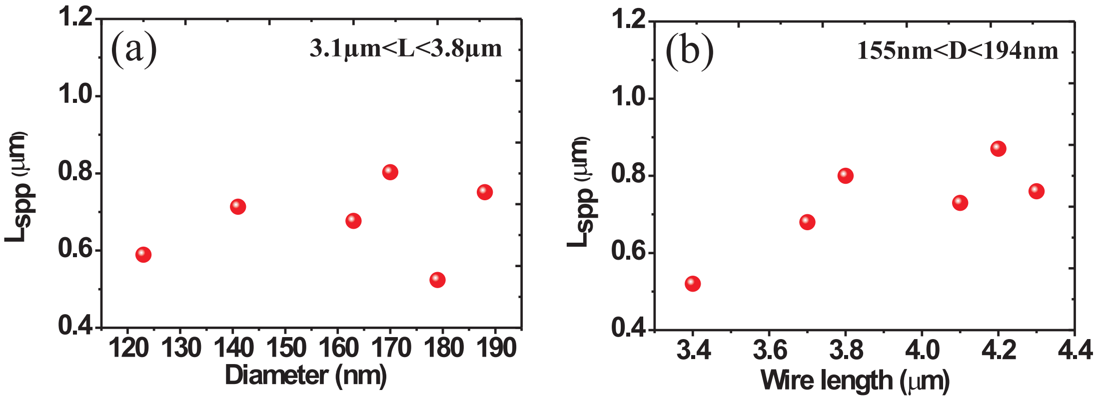

Fig 2.23: Inferred propagation length of the SPP mode from Fig. 2.22 as a function of (a) diameter and (b) length. $\lambda$=532 nm.

constant. Propagation length inferred from the FWHM is shown in Fig. 2.23. It indicates that the propagation length is not significantly affected by the wire diameter however, it shows an increase of $L_{spp}$ as the wire length is increasing. This confirms the conclusions deduced from nanowires excited at 800 nm.

The effect of nanowire geometry on the effective index and propagation length for excitations at 532 nm and 800 nm are consistent. However, comparing the propagation length at both wavelengths suggests that an infrared excitation should be favoured for transmitting signals in this system. A 3.4 $\mu$m long nanowire excited at 800 nm features a $L_{SPP}$=1.16 $\mu$m. This value drops down to 0.52 $\mu$m at 532 nm excitation.

In view of the different propagation properties for excitation at 800 nm and 532 nm, we investigated the SPP propagation properties for a large range of excitation wavelength range from 760 nm to 940 nm. The different excitation wavelengths were obtained by tuning 3900S CW Tunable Ti:Sapphire Laser. The effective index dispersion is shown in Fig. 2.24(a). It confirms that the $N_{eff}$ decreases for infrared excitation. This effective index dispersion as a function of wavelength was also observed in Ref [172]. The corresponding propagation lengths are displayed in Fig. 2.24(b). It shows a slight increase with wavelength. However the increase of excitation wavelength is usually followed by a decrease of a field confinement detrimental for ultimate integration [114].

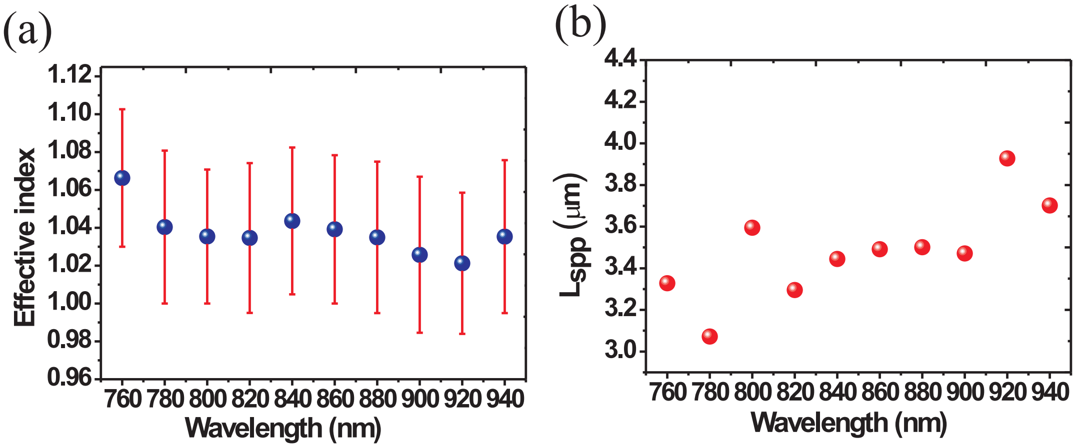

Fig 2.24: (a) Effective index as a function of excitation wavelength. The excitation wavelength is from 760 nm to 940 nm. (b) Inferred propagation length from the FWHM in (a) for different wavelength.

## 2.4 Conclusion

Plasmonic waveguides,a key components in nano-scale optical devices, are currently of intensive interests. The thorough understanding of SPP propagation properties relies on our ability to image their electromagnetic field distribution. In this chapter, we have developed an imaging technique capable of visualizing directly the propagation of surface plasmons in thicker nanowires by detecting their leakage radiation. SPP propagation in chemically synthesized pentagonal crystalline silver nanowires were excited at different wavelengths. By measuring the lateral and angular intensity distributions of the leakage, we have determined the effective indices of plasmon modes at around 1.05 for the nanowires with diameters comprised between 120 nm and 380 nm. Numerical simulations were performed to explain the unexpected low values of the effective index. By analogy with molecular orbitals of similar symmetry, the plasmon modes were determined and are in good agreement with the observed values provided that the effect of the substrate is taken into account. We found that polarization inhomogeneity can be a useful mean to preferentially coupled light either in leaky modes or in bound modes. Optical field components oriented along the wire are coupled to the leaky mode while out-of-plane field components provide the dominant contribution to excite bound modes.

We further investigated the effect of nanowire geometry (diameter, length) and excitation wavelength on the effective index and propagation loss. We found that the effective index are almost constant in our considered range of parameters while propagation length is affected by the nanowire length. Note that our measurements were restricted to nanowires with diameters above 120 nm.

From this chapter, we have a thorough understanding of the surface plasmon propagation properties in chemically synthesized pentagonal crystalline silver nanowires. It is helpful to exploit the SPP-based optical devices. However, in a plasmonic metal circuit, electrons and surface plasmon may be transported synchronously in the same physical link raising questions about the sustainability of the platform. How does the two information channel propagate on the same physical link? Is there any interference between these two information channels? Is there any limitation for co-propagating electrons and surface plasmon in a nanowire waveguide? On the basis of this chapter, we will investigate the properties of this co-propagation and try to provide answers to these questions in the following chapter.

# Chapter 3

# Co-propagation of electrons and plasmons in crystalline nanowires

## 3.1 Research motivations

Driven by the smaller, faster and more efficient on-chip devices, plasmonic circuitry possessing the huge capacity of photonics and the miniaturization of electronics. This unique potentiality has attracted tremendous interests [1, 13, 15, 23]. It is a unique platform capable for simultaneously sustaining an optical signal encoded in the form of surface plasmon and an electrical current. Figure 3.1 shows a schematic of a metallic nanowire where current-carrying electrons and surface plasmon are simultaneously guided in the same structure.

As discussed in the introduction chapter, signals transported in such a plasmonic circuity would need to be modulated [156] or rerouted to different optical channels [99, 106, 149]. This requires several optical components for signal-processing functionalities [112]. External commands such as thermo- [173], electro- [174] and magneto- [175] optical effects are considered for active and dynamic purpose. In thermo-optical devices, nanowires are not only used as waveguides but also as heating elements [55]. Current passing through the metal can efficiently heat the waveguide. Surface plasmon modulation relies on the temperature-induced change in the refractive index of the material in the region where the SPP mode is developing [55, 173].

Despite advances on control of surface plasmon field, these effects are inherently weak and SPP propagation is limited by the inevitable absorption loss. Integration of the platform with an electronic layer has remained elusive and confined to a thermo-optical con-

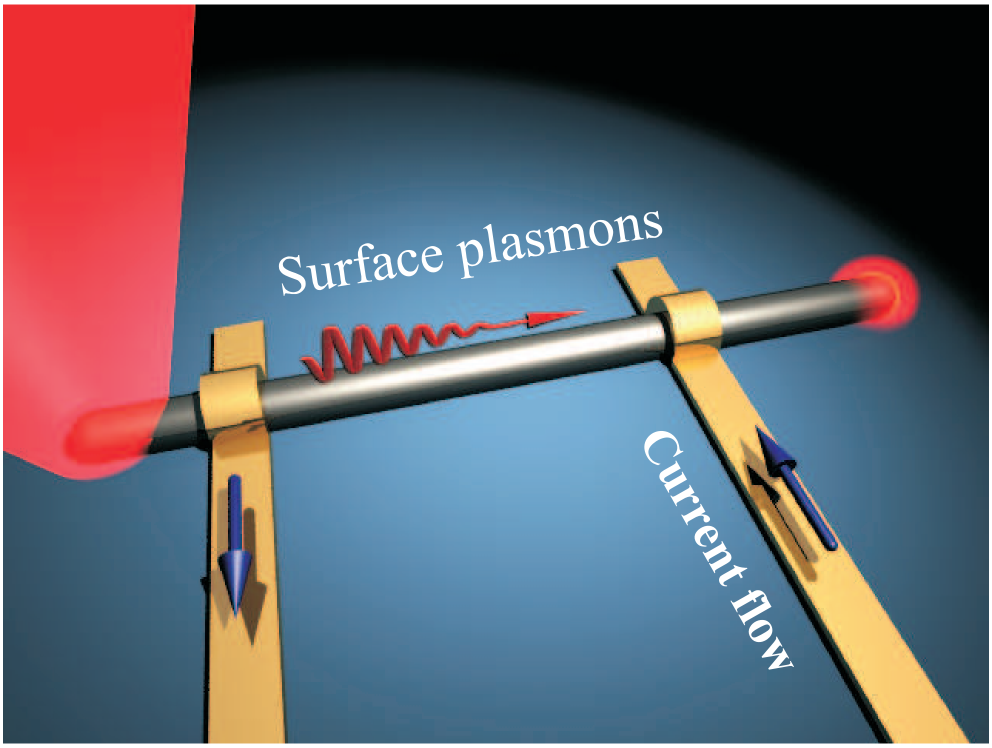

Fig 3.1: Schematic view of electrons and surface plasmons transported in the same nanowire waveguide.

trol. Possible hindering of these enhanced plasmonic performances under direct-current (DC) biasing operation is therefore of central interest to assess the capability of a plasmonic circuitry to simultaneously sustain surface plasmon propagation and electrical current.

In this chapter, we investigate the effect of electron flow on surface plasmon properties when these two information channels are transported synchronously in single crystalline metal nanowires. By recording surface plasmon characteristics as a function of the electrical environment, limiting factors affecting co-propagation in metal nanowires are experimentally determined. Tentative measurement on modulations on electron flow provides a way to investigate interference between current-carrying electrons and surface plasmons.

## 3.2 Experimental

### 3.2.1 Sample preparation

#### Nanowire synthesis

Pentagonal-twinned silver and gold nanowires were synthesized following two different protocols. Different from the synthesis of nanowires we used in chapter 2, silver nanowires used here were synthesized using wet chemical method without seed. It follows the protocol in Ref. [176]. The nanowire diameter becomes thicker with the increase of reaction time. By controlling the reaction time, silver nanowires with section width comprised between 300 nm and 600 nm were produced. The silver nanowires were synthesized by our collaborator Douguo ZHANG at University of Science and Technology of China, Hefei, China. Au nanowires were synthesized using nitrate ion assisted conventional synthesis [177]. It is based on the a three-step seeding approach. Due to the different protocol, gold nanowires with section width between 70 nm and 120 nm were produced. The gold nanowires used in our measurement were synthesized by our collaborators Aniket Thete and Erik Dujardin at CEMES, Toulouse.

#### Contacted electrodes fabrication

Nanowires contacted with Au electrodes were fabricated using two-step electron beam lithography. The first part of the procedure closely follows the protocol outlined in chapter 2. A solution containing nanowires was drop-casted on the glass substrate pre-patterned with grid landmarks. Figure 3.2(a) displays SEM images of grid landmark. The four

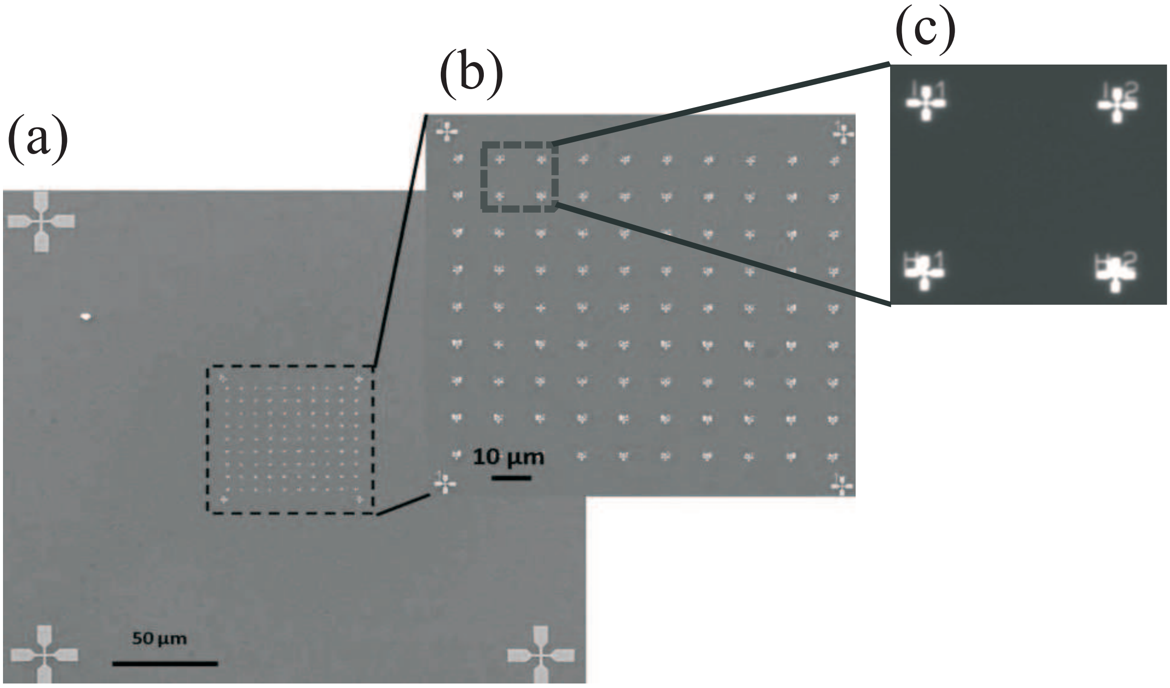

Fig 3.2: (a) SEM image of the grid landmark structure. (b) Enlarged image of the structure inside the black dashed box. (c) Close-view of the smallest repositioning structures. A single mark consists of a cross, a letter and a number.

corner microscopic marks are used for coarse alignment during the second lithography. An enlarged view inside the black dashed box is shown in Fig. 3.2(b). There are another four microscopic marks at the corners which can be used for a second, more precise, alignment. The smallest marks consisting of letters, numbers and crosses in Fig. 3.2(c) are used not only to locate the nanowires but also for the third and final alignment.

The grid landmarks were employed to precisely coordinate the nanowire position by optical microscopy. Gold electrodes connecting the extremities of the nanowires were subsequently fabricated in a second step of e-beam lithography. A 70 nm-thick gold layer was evaporated to form the leads. Because the thickness of the electrodes is smaller than the radius of the nanowires, Au evaporation was performed at a $\sim 50°$ azimuthal angle to insure the electrical continuity between the electrodes and the nanowires.

Optical images (reflection) of silver and gold nanowires contacted with Au electrodes are shown in Fig. 3.3. The silver nanowire with 400 nm in diameter and 19 $\mu$m in length in Fig. 3.3(a) is much longer and thicker than the gold nanowire which has 110 nm in diameter and 6.2 $\mu$m in length in Fig. 3.3(b). The Au electrodes was evaporated with

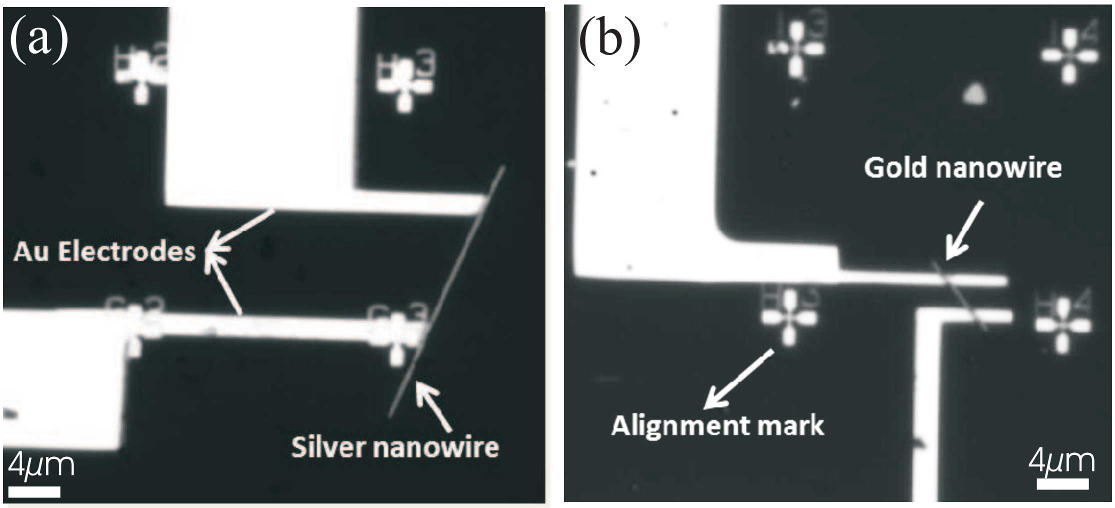

Fig 3.3: Optical images of (a) silver nanowire and (b) gold nanowire contacted with Au electrodes on a glass substrate patterned with alignment marks. Silver nanowire is 400 nm in diameter and 19 $\mu$m in length. The gold nanowire is 110 nm in diameter and 6.2 $\mu$m in length.

$\sim 50°$ from the left side. Since the Ag nanowire is much thicker compared to the thickness of the electrodes, the part of Au electrodes evaporated on the right side of the nanowire are not contacted with the wire and fell off during the lift-off. However, the thickness of gold nanowire is similar to that of the electrodes, hence the evaporated Au electrodes are contacting the Au nanowire on both sides. The small marks introduced in Fig. 3.2(c) are readily seen.

### 3.2.2 Measurement setup

In our measurement, co-propagating electrons and surface plasmons were recorded synchronously. Figure 3.4 schematically described the principle of our measurement. Nanowires contacted with Au electrodes were optically excited at $\lambda$=810 nm. The surface plasmon characteristics were detected using the same leakage radiation microscopy introduced in chapter 2. The microscopic electrodes were electrically operated with a set of probe stations mounted with tungsten tips (radius $\sim$100$\mu$m). DC bias was slowly applied on the nanowires at a rate 30 mV/s by a regulated low voltage power supply (Keithley 4200-SCS Semiconductor analyzer) while surface plasmons were propagating in the nanowire. Current flow was recorded directly by the semi-conductor analyzer. The two charge-coupled

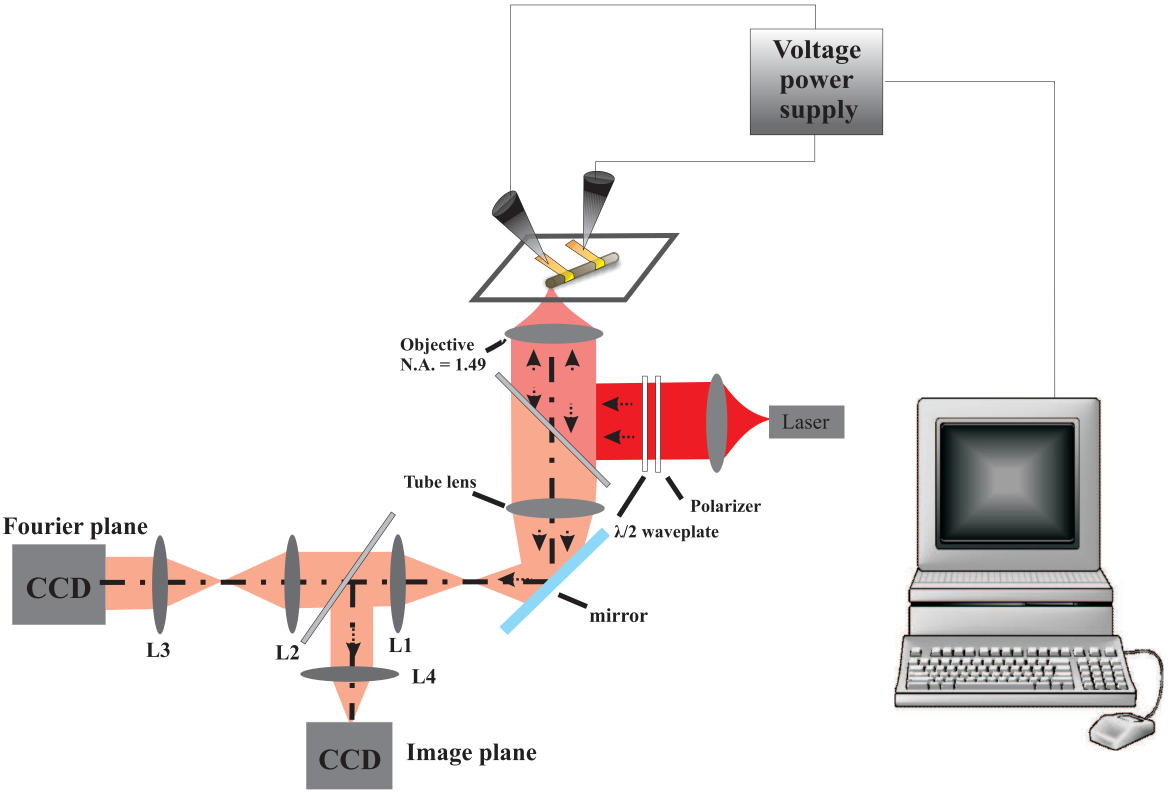

Fig 3.4: Schematic view of the synchronous recording of surface plasmon and current/voltage characteristics. The nanowire is electrically biased by a regulated voltage power supply (Keithley 4200-SCS) and the current is recorded directly with Keithley 4200-SCS. The imaging of surface plasmon is the same as in chapter 2.

device (CCD) cameras placed at the conjugated image and Fourier planes were set to acquire images every 1 s and were synchronized with the start of the bias.

## 3.3 Results and discussions

### 3.3.1 Electrical characteristics

#### Electrical characteristics of Ag nanowires

Two representative electrical output characteristics of contacted Ag nanowires are displayed in Fig. 3.5 during an initial bias sweep. Current flowing in the nanowire is typically low across a large range of bias until 0.8 V in Fig. 3.5(a) and 0.9 V in Fig. 3.5(b) and occurs by increasing steps. The number of steps was depending on specific nanowires, but

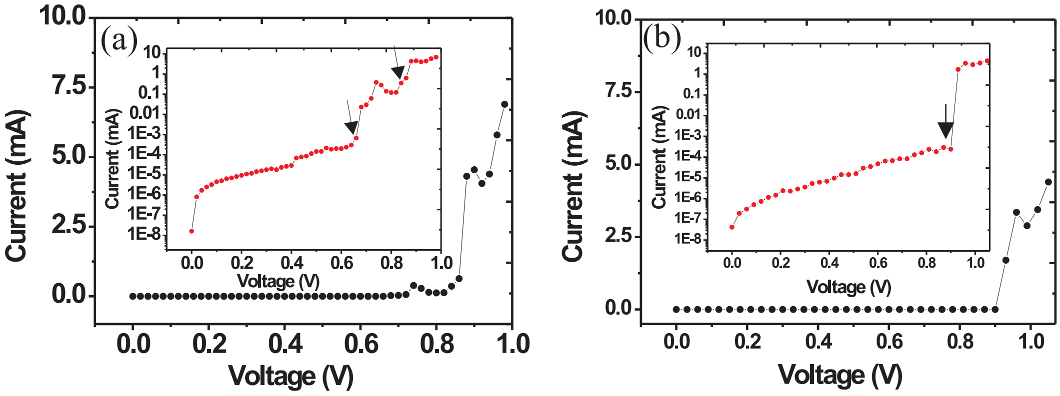

Fig 3.5: (a) and (b) Electrical characteristic of two contacted Ag nanowires during an initial bias sweep. The current flowing through the nanowires occurs by steps and is very low until 0.8 V. Insets: curves displayed in semi-logarithmic scale. The black arrows indicate the current bursts.

we never observed more than 3 current bursts on a given characteristics. The occurrence of the steps is better illustrated by the arrows in the semi-logarithmic plots shown in the insets. Interestingly, the evolution of the current between the steps is exponentially depending on the bias voltage (linear relationship in the semi-logarithmic plots). This is rather unexpected for a Au/Ag ohmic contact. For all the nanowires investigated, the position of the first current step was approximately occurring at a well-defined threshold. Figure 3.6 shows an histogram of this first burst of current following the exponential rise of the current for 16 nanowires. For the majority of the nanowires, the burst of electron flow was measured at $\sim 1 \times 10^{-5}$ mA. The figure also shows the histogram of the last step in the current-to-voltage characteristics. Its position is also distributed in a relatively well-defined current value at ~0.5 mA.

The narrow ranges reported in Fig. 3.6 suggest a common origin to the non-monotonous response, probably originating from the initially poor electrical connection between the nanowire and the leads.

A transmission electron micrograph (TEM) shows a ~3.5 nm thick surfactant layer on the surface of a Ag nanowire in Fig. 3.7(a). The chemistry employed to synthesize the nanowires uses an excess of Polyvinylpyrrolidone (PVP) surfactant that is bound to the surface of the nanowire. This organic layer acts as a dielectric barrier preventing current to flow between the electrodes and the nanowire, explaining the tunnel-like electron transport between current bursts. These events in Fig. 3.5 occur at threshold voltages and current

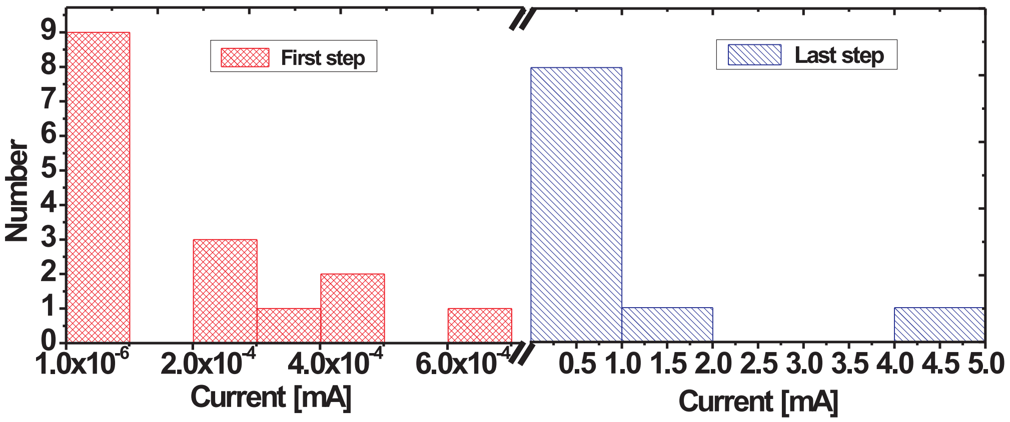

Fig 3.6: Histograms representing the values of the initial and final current steps measured in the current-to-voltage characteristics.

densities that are large enough to physically destroy the surfactant layer. For current above 5 to 10 mA, the typical resistance is below 100 Ω indicating a metallic electrical contact. This is demonstrated in Fig. 3.7(b) where the current/voltage characteristic was measured again during a subsequent bias sweep following the initial run for the same nanowire discussed in Fig. 3.5(a). A monotonous rise of the current with increasing voltage is observed. For low voltage, the current/voltage characteristic follows a linear trend (dashed line) with a slope of 25 Ω corresponding to the total resistance of the contacts.

After 0.3 V, the trend becomes nonlinear with an increasing resistance of the nanowire with voltage. This variation of resistance can be attributed to the temperature rise caused by the current flow and the onset of morphological changes induced by an electromigration process. The positive temperature coefficient of the resistance $\alpha_R$ results in an increase resistance with current flow [178, 179]. Additionally, the variation of cross-section by electromigration and the increase of local temperature caused by morphological change can also lead to an increased resistance [180, 181].

### Electrical characteristics of Au nanowires

For Au nanowires, the current/voltage characteristic was often the type displayed in Fig. 3.8(a) during the initial bias sweep. This can be explained from the TEM image

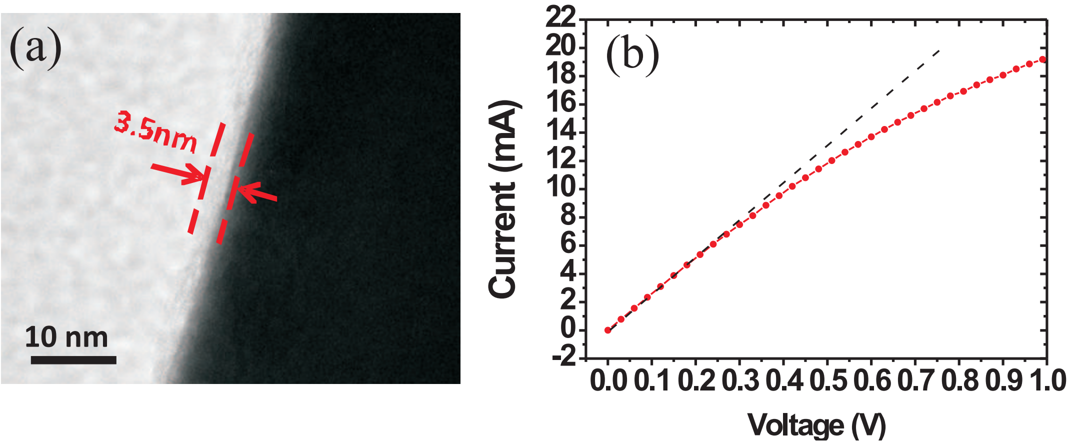

Fig 3.7: (a) TEM image of the PVP surfactant layer (~3.5 nm) encapsulating a Ag nanowire. (b) Electrical characteristic of the same Ag nanowire in Fig. 3.5(a) during a subsequent bias sweep. The curve shows a monotonous evolution of the current departing from an ohmic behaviour after 0.3 V due to a temperature-dependent resistance.

of Au nanowire in Fig. 3.8(b) showing an uncompleted covering of the surfactant on the surface of Au nanowires. The red dashed lines mark the area without surfactant covering. The uncompleted covering is leading a ohmic electrical connection between the Au nanowire and the electrodes. For low voltage the electrical characteristics is similar to Ag nanowire; the current follows a linear trend (dashed line) with a slope of 24 Ω corresponding to the total resistance of the contacts. The resistance is similar to that of Ag nanowire in Fig. 3.7(b). The trend becomes nonlinear with an increasing resistance of the nanowire with voltage after 0.25 V which is slightly lower than Ag nanowire (~0.3 V) in Fig. 3.7(b).

### 3.3.2 Surface plasmon propagation in contacted nanowires

We now turn our attention to the properties of surface plasmons propagating in these contacted nanowires. Measurements with leakage radiation microscopy provide a direct visualisation of plasmon propagation in the nanowire while parameters like effective index of the guided surface plasmon mode and overall losses were estimated from Fourier plane analysis.

A representative leakage radiation image of an electrically contacted Ag nanowire in our measurement is displayed in Fig. 3.9(a). Ag nanowire with section width 500 nm was

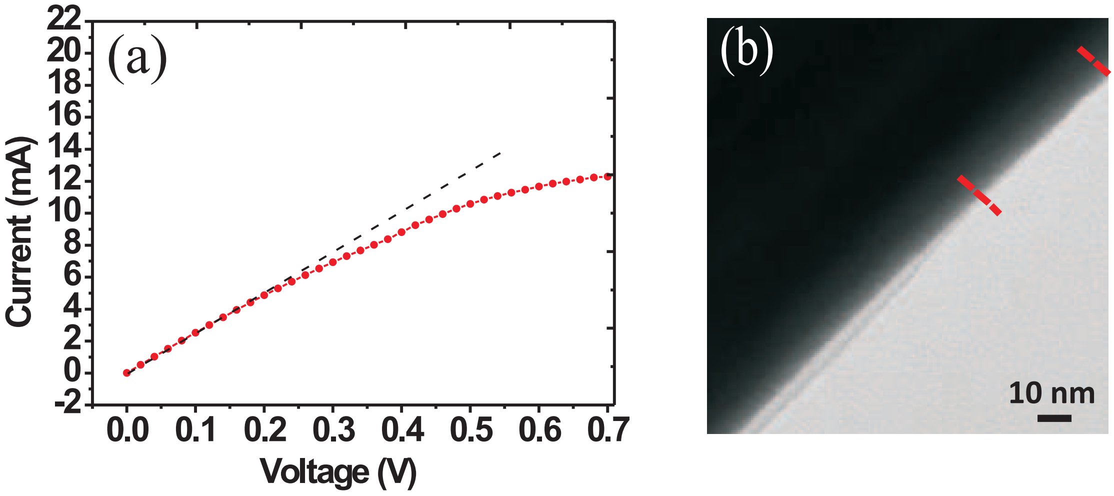

Fig 3.8: (a) Electrical characteristic of Au nanowire. The monotonous evolution of the current is departing from an ohmic behaviour after 0.25 V. (b) TEM image of Au nanowire shows an uneven distribution of PVP surfactant on the nanowire surface.

excited with a linear polarization oriented along the nanowire. The electrodes are readily visible in this image. The excitation spot overlapping the lower extremity of the nanowire defines the origin of the reference Cartesian frame $(x, y)$. The surface plasmon developing along the nanowire is readily observed in this configuration. At the distal end, the surface plasmon is scattered off the waveguide. Similar image was recorded for Au nanowires in Fig. 3.9(b). However, the intensity distribution of surface plasmon is hardly seen in the image plane of the Au nanowire. The attenuation of surface plasmon propagation in Au nanowires combined with a reduced coupling efficiency resulting from a smaller diameter implied working with shorter nanowires and electrode separation compared to Ag nanowires. Images obtained for Au nanowires were therefore more difficult to analyze.

From Fig. 3.9(a) there is no evidence that the leaky plasmon propagating along the uncoated section of the wire is significantly altered by the presence of the two 2 $\mu$m-wide electrodes. At the electrode positions, the field distribution of the mode is modified by the additional 70 nm-thick gold layer on top of the Ag nanowire and no longer leaks in the substrate. However, leakages resume on the uncoated sections of the nanowire indicating that the mode is retained along the pristine nanowire. This is confirmed by Fourier analysis of the wave vector distribution displayed in Fig. 3.10. The surface plasmon mode is recognized as the unique bright line at an effective index $N_{eff} = +k_x/k_0$ =1.056 (arrows),

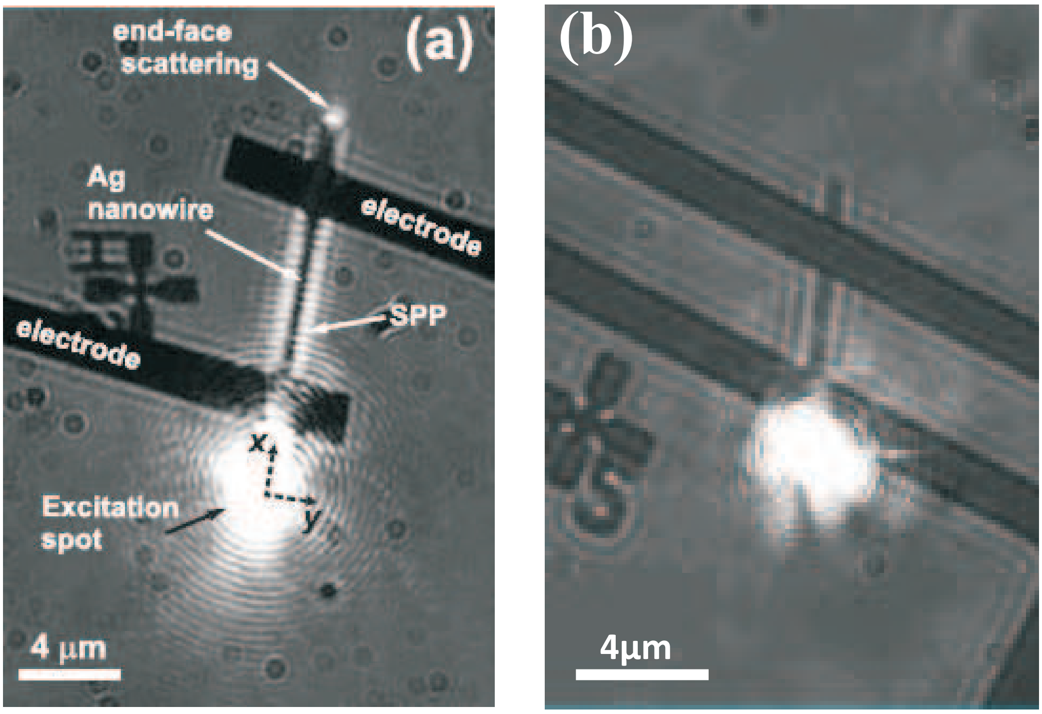

Fig 3.9: Leakage radiation image of a surface plasmon propagating in an electrically contacted Ag nanowire (a) and Au nanowire (b). The excitation laser spot polarized along the nanowire is adjusted with the lower extremity. Surface plasmon propagating along the Ag nanowire is readily seen while SPPs in Au nanowire are typically more difficult to investigate.

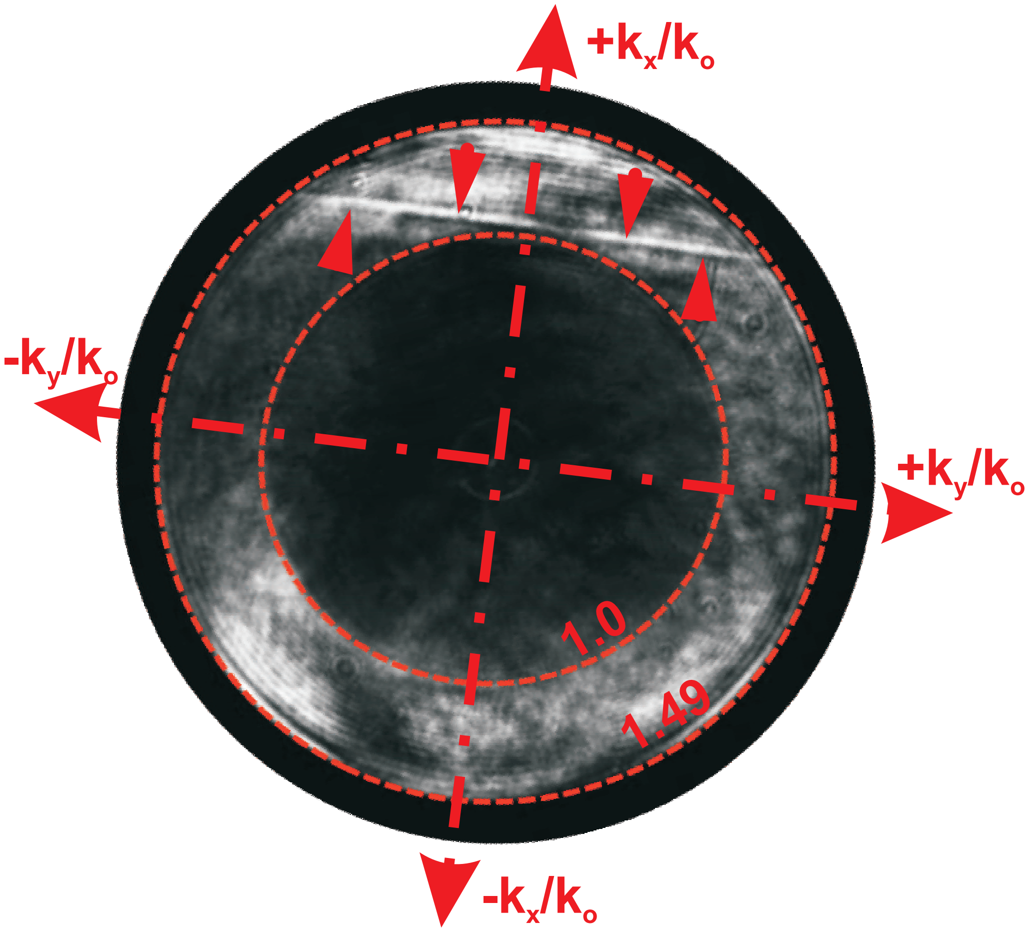

Fig 3.10: Wave vector distribution obtained by Fourier-plane imaging. The surface plasmon mode in the contacted nanowire is recognized as a bright line at a $N_{eff} = +k_x/k_0 = 1.05$ (arrows). $k_x/k_0$ =1.49 and $k_x/k_0$ =1.0 are given by the numerical aperture of the objective and the critical angle at the glass/air interface, respectively.

where $k_x/k_0$ is the reciprocal axis with $k_0 = 2\pi/\lambda$ is the free-space wave vector. The imaginary part of the complex effective index accounts for the width of the line and the measured value at half-maximum (FWHM = 0.09) is somewhat slightly smaller to unconnected nanowires measured in the previous chapter (FWHM = 0.04). We hypothesized that a significant field overlap exists between the modes sustained at the electrode-coated sections and the uncovered sections of the nanowire thus promoting energy transfer between the modes [182, 183]. This is conceptually equivalent to a hybrid coupling strategies developed in Ref. [105].

### 3.3.3 Co-propagation of electrons and surface plasmons

Surface plasmon propagation along the nanowires was simultaneously recorded in this dual-plane imaging mode while synchronously sweeping the DC bias with 30 mV steps. Figure 3.11(a) displays an optical transmission image of a contacted Ag nanowire with diameter 410 nm and length 26.7 $\mu$m. The current/voltage output characteristics is reported in Fig. 3.11(b). For each voltage/current values, a direct space image and its corresponding Fourier content were recorded. We choose three voltage/current values indicated by the black arrows that are corresponding to the beginning of the bias sweep (i), during the nonlinear trend (ii) and after the electrical breakdown (iii), respectively to show the co-propagation characteristics.

The leakage radiation images of the wire corresponding to the three current/voltage output in Fig. 3.11(b) are shown in Fig. 3.12(a). At the beginning of the bias sweep (Fig. 3.12(a)), both the surface plasmons and its scattering at the end of the wire are readily seen. When the current evolves nonlinearly with the voltage (Fig. 3.12(b)), the plasmon scattered off the end gradually disappears and the intensity of surface plasmon leakage becomes lower. This is accompanied by a shorter spatial extension of the intensity distribution along the nanowire. After electrical failure (Fig. 3.12(c)), the leaky surface plasmon has almost vanished. A very weak residual signature can be seen at the close vicinity of the laser spot.

The corresponding Fourier images are displayed in Fig. 3.13. As previously introduced, the surface plasmon mode is recognized as the bright bar in the Fourier plane. Here, we only show an area of interest surrounding the plasmon signature. As bias increases, the intensity of surface plasmon mode gradually decreases. A very weak surface plasmon mode is observed in Fig. 3.13(c) after the electrical failure confirming the residual leakage signal observed in Fig. 3.12(c).

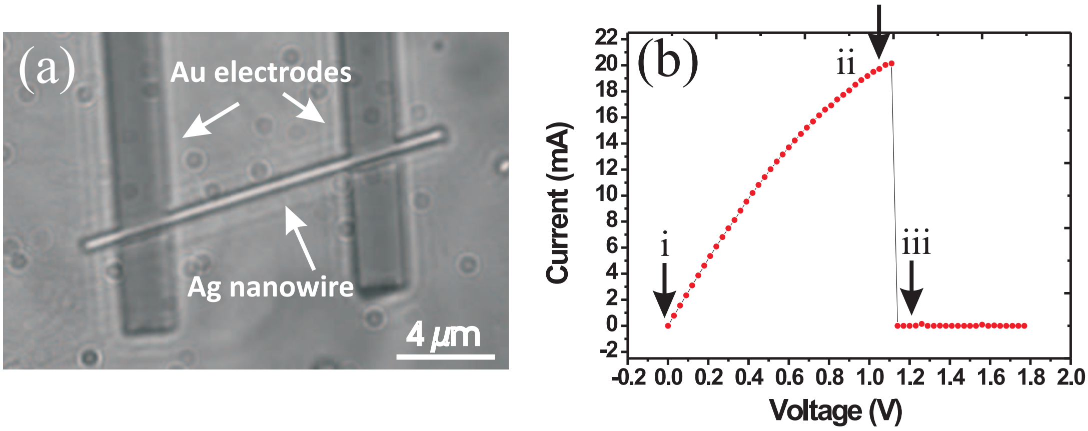

Fig 3.11: (a) Bright field image of the contacted Ag nanowire. (width 500 nm, length 26.7 $\mu$m). (b) Current-voltage output characteristics of the Ag nanowire. Three current/voltage output indicating by the arrows are at the beginning of the bias sweep (i), during the nonlinear evolution (ii) and after the electrical failure(iii), respectively.

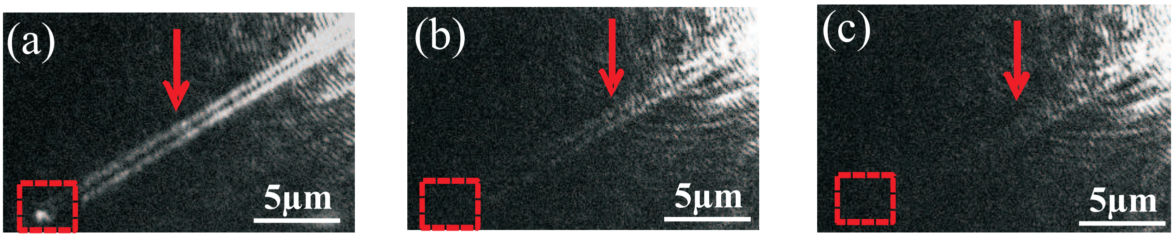

Fig 3.12: (a) Leakage radiation images a Ag nanowire corresponding to the three current/voltage output in Fig. 3.11(b). The scattering light at the end of the wire and surface plasmon propagating along the wire are indicated with the red boxes and arrows, respectively.

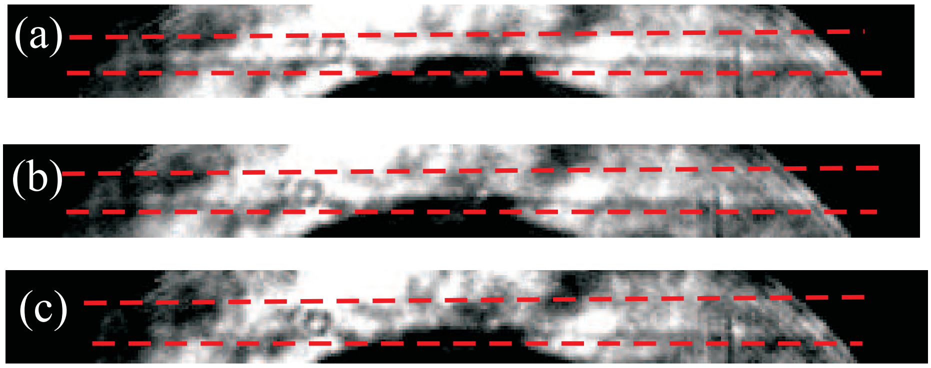

Fig 3.13: An area of interest in Fourier images corresponding to the three leakage radiation images in Fig. 3.12. As bias increases, the intensity of surface plasmon mode gradually decreases from (a) to (c).

The existence of the residual plasmon mode can be well explained from the SEM image of nanowire after electrical failure in Fig. 3.14(a). The failure position (red arrow) is very close to the plasmon launching end of the nanowire. Although damaged from an electrical standpoint, the gap produced during the failure is bridged by leftover material resulting in a weak, but finite surface plasmon transmission between the two sides. The cross-section profiles corresponding to situation (a) and (b) in Fig. 3.13 are displayed in Fig. 3.14(b). A Lorentzian fit of the two curves yields a $N_{eff}$ 1.05 for the nanowire at small bias (i) shown in Fig. 3.11(b) and $N_{eff}$ 1.03 just before failure.

To quantitatively analyze this reduction of the surface plasmon effective index with bias, we report in Fig. 3.15(a) the value of the real and imaginary part of the effective index for each biasing step. The characteristics of the mode remain almost constant within experimental measurement errors at an average $N_{eff}$ =1.058+ i0.09 until 0.87 V. In this voltage range, propagation of the plasmon mode is not affected by the flow of charges and the temperature rise of the nanowire. Above 0.87 V (shaded area), the real and imaginary part of the complex effective index are changed from the average value at lower voltages and become dependent of the biasing condition. Extrinsic propagation losses encoded in the rise of FWHM are concomitant to a measurable reduction of $N_{eff}$. The increasing propagation loss can be demonstrated by the decreasing intensity of the scattering light at the distal end of the nanowire above 0.87 V shown in Fig. 3.15(b). The change of the effective index and propagation loss is closely related to the electrical output characteristics of the nanowire reported in Fig. 3.15(c). The plasmon propagation is affected by the applied bias at the point where electromigration of the nanowire becomes

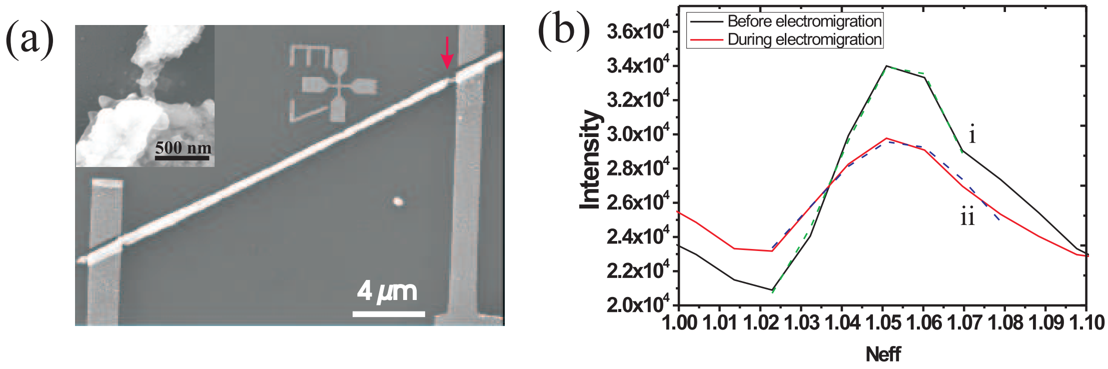

Fig 3.14: (a) SEM image of the nanowire after electrical breakdown. The red arrow indicates the failure position. The inset shows a closeup view of the electrical failure. (b) Cross-section profiles of the Fourier plane measurement before and during breakdown in Fig. 3.13.

predominant in the current/voltage characteristic (shaded area).

Electromigration is the transport of material caused by the gradual movement of the ions in a conductor due to the momentum transfer between conducting electrons and diffusing metal atoms [184, 185, 186]. The driving force for electromigration is divided into two components: wind force and direct force depicted in Fig. 3.16. The wind force is caused by the momentum transfer from the electrons to the charge carrier. The direct force is due to the bulk electric field acting on the atoms that are not completely shielded by the electrons. The mass flow caused by the direct force is in the opposite direction to that caused by wind force.

The largest variation of $N_{eff}$ and FWHM in Fig. 3.15(a) occurs when the current suddenly drops indicating electrical breakdown of the nanowire. Under such electrical stress, the morphology of the nanowire is significantly affected by the electromigrated mass transport [187] thus compromising plasmon propagation.

To confirm this drastic morphological change, we have imaged the nanowires before applying a bias and after electrical breakdown. Freshly contacted nanowires were imaged by bright-field optical microscopy in order to avoid electron-beam carbon contamination by a scanning electron microscope (SEM). After electromigration however, a thin layer of Au ( $<$ 20 nm) was sputtered on the sample for detailed SEM investigation. A representative example of a 18 $\mu$m-long 500 nm-wide Ag nanowire is shown in Fig. 3.17. The SEM image obtained after electromigrating the nanowire (Fig. 3.17(b)) confirms its the structural deformation. For all of the Ag nanowires we investigated, electrical failure

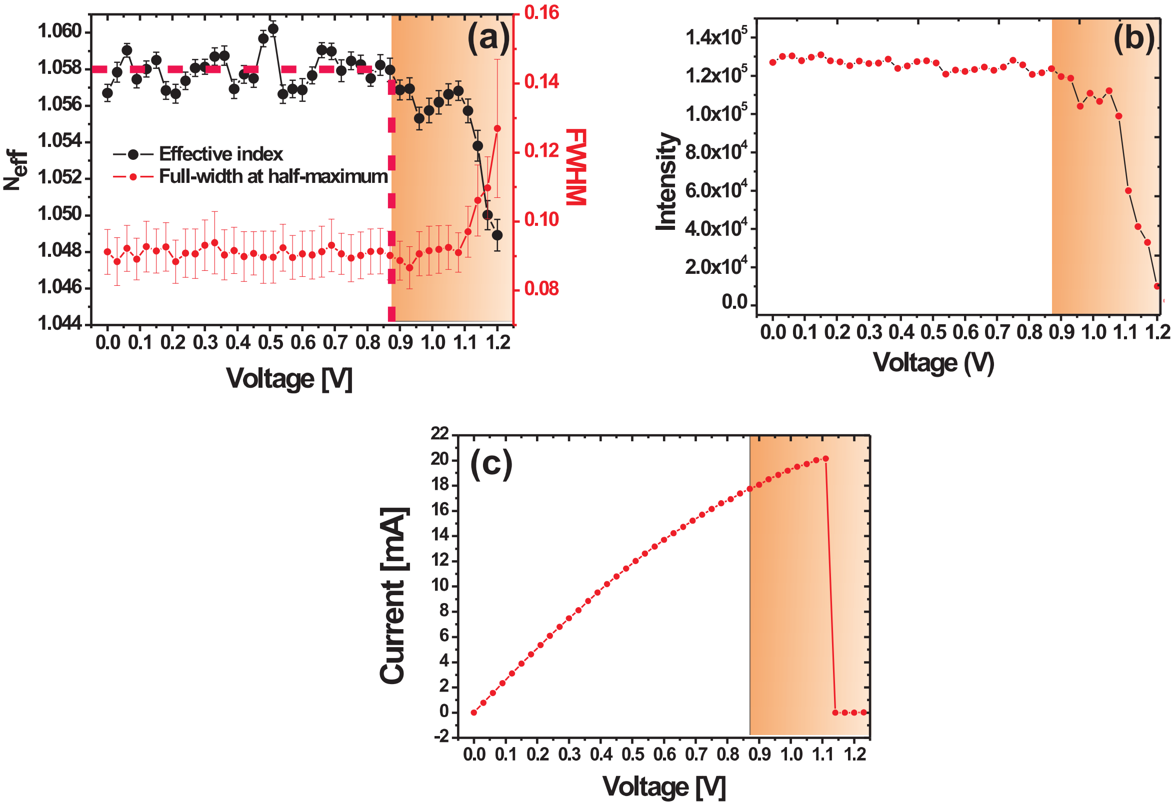

Fig 3.15: (a) Effective index and FWHM of the surface plasmon in a Ag nanowire (width 500 nm). Both parameters are obtained by Lorentzian fit of the cross-section along the reciprocal $+k_x/k_0$ axis in Fourier-plane measurements. The error bars are given by the fit process. (b) Intensity of scattering light at the end of the same wire. (c) Simultaneous current-voltage output characteristics of the Ag nanowire. The sudden current drop at 1.1 V indicates electrical breakdown of the nanowire.

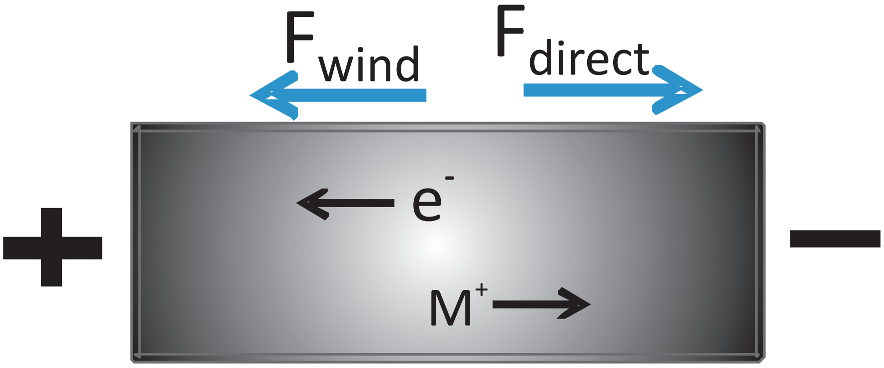

Fig 3.16: Schematic diagram of the driving force for electromigration. The wind force and direct force are in the opposite direction.

occurs at the positive electrode (point 1). This position of electrical failure in crystalline nanowires is different from the previous reports on polycrystalline gold nanowires in which electrical failure occurred at the ground electrodes [180, 188].

For single crystalline Ag nanowire, the enhanced surface diffusion plays the dominating role for electromigration process rather than the grain boundary diffusion as indicated in Ref. [184, 189]. This results in the direct force overcompensating the wind force and is thus the predominating force during the electromigration process, explaining why the electrical failure occurred near the positive electrode. This behavior has also been reported for other type of crystalline Ag nanowires [184, 189] and suggests that the breakage originates from a motion of charged atoms initiated by the electric field present across the nanowire.

Figure 3.17(b) also shows a weaker but visible mass transport along the electron flow: a thinner nanowire section near the ground electrode (point 2) is visible in the SEM image. This section is immediately followed by a wider area (point 3) indicating that Ag atoms were displaced from point 2 to point 3. This can be attributed to the high temperature gradient close to the electrode leading to the surface diffusion of melted Ag to nearby low temperature parts [187]. The original nanowire section is measured at point 4, on the right of the positive electrode. At this location, current flow did not affect the nanowire. Note that the section of the wire at point 3 is wider than the original nanowire size at point 4.

Electrical failure of Au nanowires was also systematically observed near the positive electrode in our measurements. The SEM images of two Au nanowires after electromigration are displayed in Fig. 3.18. The electrical failure occurs at point 1 close to the positive

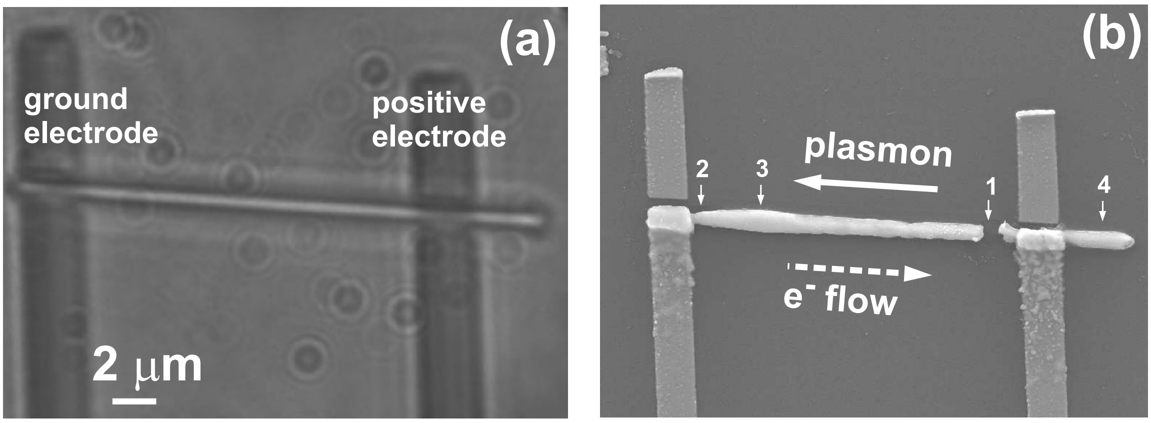

Fig 3.17: (a) Bright-field optical image and (b) scanning electron micrograph (SEM) of a 18 $\mu$m-long 500 nm-wide contacted Ag nanowire before and after electrical breakdown, respectively. The surface plasmon excited at the positive leads is propagating opposite to that of electron motion. The electromigration causes electrical failure at the positive electrode. The two gaps between the nanowire and the upper section of the electrodes are caused by the angled evaporation of the metal. Points 1 indicates the location of electrical breakdown, points 2 and 3 the morphological changes of the section due to mass transport, and point 4 the pristine nanowire.

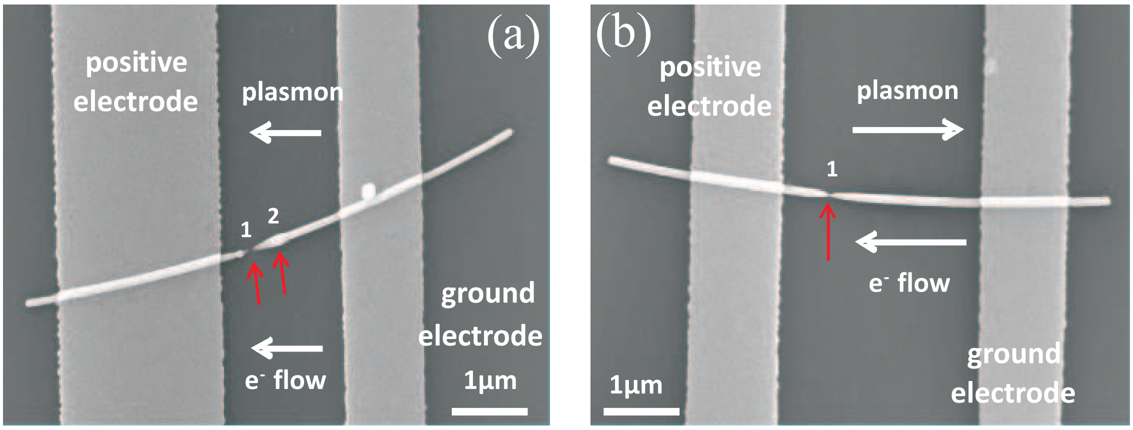

Fig 3.18: Scanning electron micrograph (SEM) of a 6.7 $\mu$m-long 70 nm-wide and 6.5 $\mu$m-long 90 nm-wide contacted Au nanowires after electrical breakdown. (a) Surface plasmon excited at the ground lead is propagating to the same direction as the electron motion. (b) Surface plasmon excited at the positive lead is propagating opposite to direction of the electron motion. The electromigration causes electrical failure near the positive electrode which is the same as Ag nanowire. Points 1 indicates the location of electrical breakdown. An obvious mass transport can be seen at point 2 in (a).

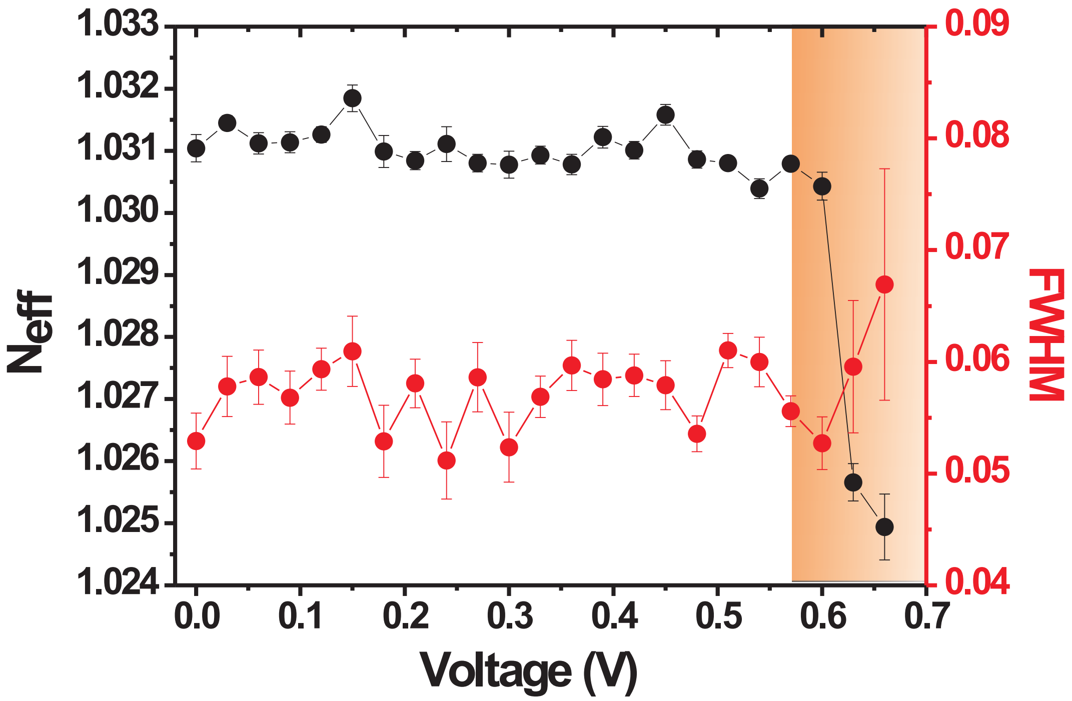

Fig 3.19: Effective index and FWHM of the surface plasmon in a Ag nanowire (width 450 nm) for a current flowing along the same direction. The error bars are given by the fit process. Electrical failure occurred after 0.6 V.

electrode. An obvious morphological change can be seen at point 2 in Fig. 3.18(a) towards the ground electrode. For the Au nanowire in Fig. 3.18(b), its section becomes thinner on both sides of the failure gap and there is no obvious morphological change at other place. This could due to the high local temperature at the failure position which melts the gold wire in very short time and resulting in the breakdown [179].

In order to see if the direction of the electron flow would influence the propagation of the surface plasmon, the polarity was reversed, *i.e.* electrons and plasmon propagating in the same direction. The surface plasmon characteristic is shown in Fig. 3.19. The effective index remains almost constant until 0.6 V and then drops dramatically. FWHM also has a slight increase during the electromigration. We did not observe significant differences from the trend displayed in Fig. 3.15 indicating that the same limitations occur regardless of the direction of the electron flow.

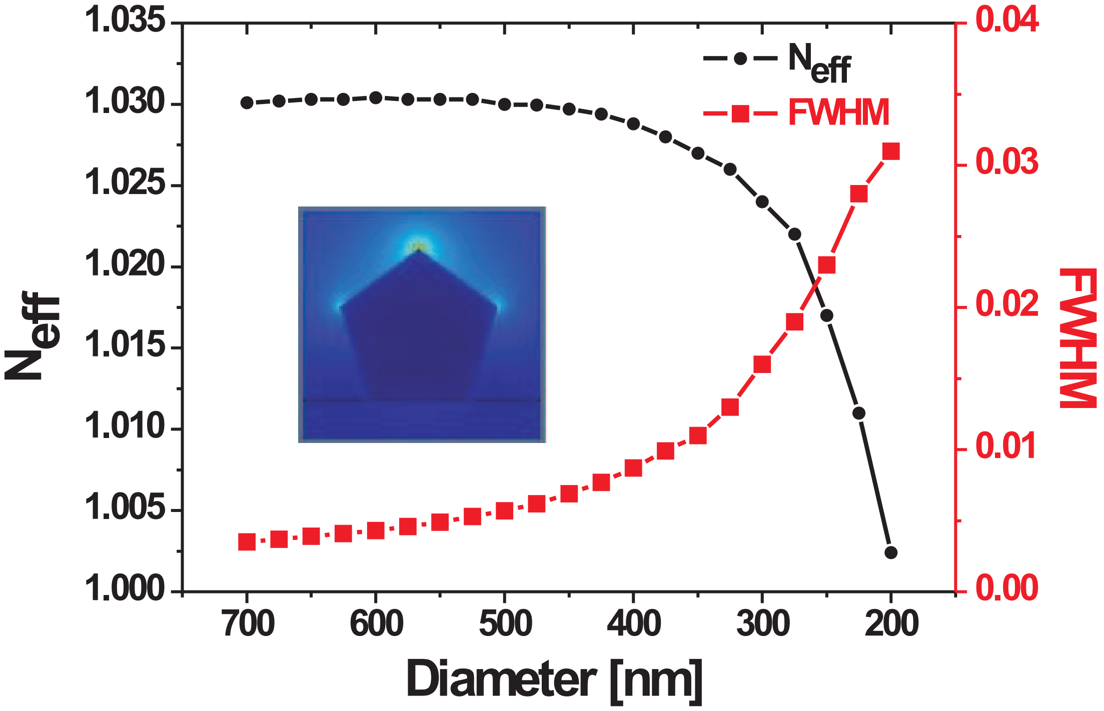

Fig 3.20: Calculated dispersion of the real and imaginary parts of the surface plasmon effective index as a function of width of the nanowire. The inset shows a cross-sectional intensity distribution of the plasmon mode for a pentagonal Ag nanowire with a section of 300 nm.

### 3.3.4 Numerical simulations

From Fig. 3.17(b), it is clear the evolution of the surface plasmon effective index and propagation loss with applied bias described in Fig. 3.15(a) can be attributed to the altered section of the nanowire and loss of crystallinity caused by the electromigration process. To test this hypothesis, we numerically investigated the effect of a varying nanowire section on the effective index and propagation loss of the surface plasmon using the finite element analysis simulation software COMSOL Multiphysics. The model is the same as the one introduced in last chapter.

We considered a single pentagonal crystalline silver on a glass substrate with an excitation wavelength $\lambda$ = 800 nm and a silver optical index $n_{Ag}$ = 0.0362+i5.4. Since the effective index of the plasmon mode is very close to 1.0, the mode can easily radiate into air. To account for this, we add perfectly-matched layers on the air side of the calculation window. The evolution of the effective index with reducing nanowire width is reported in Fig. 3.20. The cross-sectional intensity distribution of the mode displayed in the inset for a section of 300 nm shows an intensity mainly distributed in the air side. The $N_{eff}$ and FWHM are weakly depending on nanowire section until approximatively 450 nm. For width $< 400$ nm, $N_{eff}$ monotonously decreases towards the cut-off value of the mode (1.0), a condition confirmed by the associated larger losses in this section range. A small discrepancy between the experimental and calculated $N_{eff}$ ($\sim$0.02) can be attributed to same reason discussed in chapter 2. Nonetheless, according to SEM images of electromigrated nanowires, the thinnest unbroken section is around 250 nm to 300 nm. The calculated dispersion curve shows that the $N_{eff}$ of the mode is reduced from 1.034 to $\sim$ 1.020, a change of 0.014 in this section range. Although the relationship between the width of the nanowire and the applied bias is not trivial (non linear electrical characteristic and local variations along the length), the measured difference of $N_{eff}$ before and after breakdown in Fig. 3.15(a), $\sim$0.01, is comparable to our numerical simulations.

Concerning the imaginary part FWHM, the numerical trend also qualitatively reproduces the experimental measurement of Fig. 3.15(a). Amorphization of the nanowire during the electromigration process [187] and variation of the section along the length of the nanowires were omitted in the calculation. However, both effects introduce additional plasmon damping compared to pristine nanowires and accounts for the under approximation of the plasmon losses in Fig. 3.20. A comparison of SPP propagation of amorphous and cristalline Ag nanowires can be found in Ref. [88]. The scattered light spectrum corresponding to the polycrystalline Ag nanowire displayed no regular signal modulation indicating the presence of surface-induced losses for an amorphous geometry.

### 3.3.5 Limits of operation

From the above investigations, change in the morphology of the nanowire appears to be the main limitation for co-propagating plasmonic and electronic information in metal nanowires. Figure 3.21 shows the maximum current densities before electrical failure as a function of nanowire width. The data points are the measured current densities reached just before failure of Au and Ag nanowires. The dependence of failure current density on the nanowire width has been investigated for Au [178, 179] and Cu nanowires [190]. Calculations on width-dependent failure current density of Cu nanowire in Ref. [190] suggests that the width dependence is a result of the contact area between the nanowire and substrate since most of the heat transfer occurs at the nanowire substrate interface.

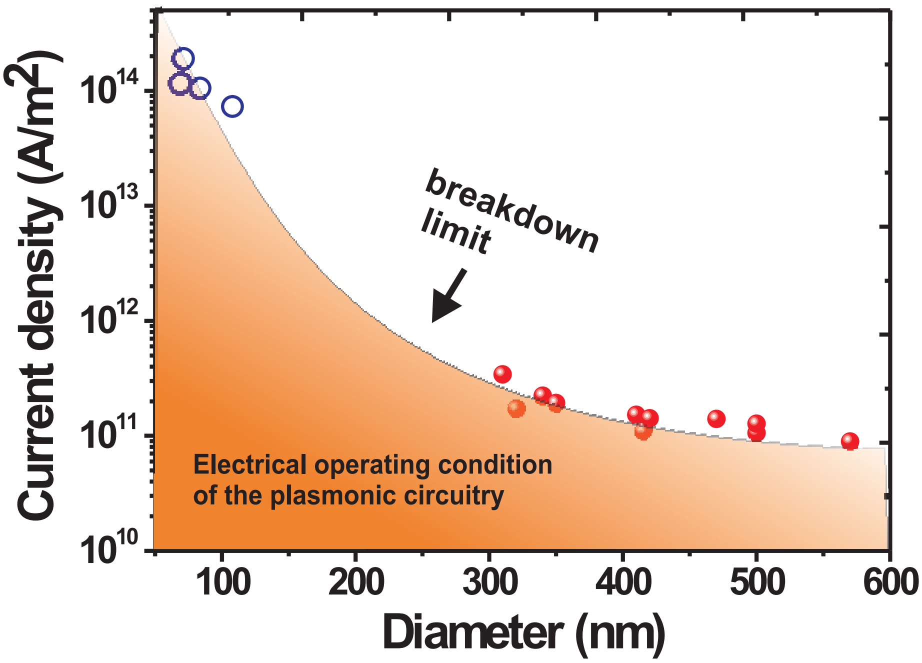

Fig 3.21: Current density leading to electrical failure of crystalline Au (○) and Ag (●) nanowires as a function of nanowire width. The shaded area indicates the safe electrical operating condition to simultaneously propagate electrons and surface plasmons in the waveguide.

The experimental data in these studies shows a higher failure current density for smaller wire width. Like Cu nanowires, the failure current densities in crystalline Au and Ag structures depends on the section as a results of a better heat dissipation in the glass substrate as shown in Fig. 3.21. The shaded area in the graph provides an upper limit on the the electrical condition under which electrons and surface plasmons can be simultaneously supported by the plasmonic platform. Thin nanowires can sustain a higher current density and, from an electrical point of view, should be favored in the circuitry. Since the plasmonic properties of thinner nanowires are generally enhanced from thicker nanowires [144], no trade off between electrical and plasmonic performances is anticipated in this regard.

## 3.4 Conclusions

In plasmonic circuitry, a key element is the shared metal network between electrical and optical information enabling an efficient heterointegration of an electronic control layer and a plasmonic data link. In this chapter, by synchronously recording surface plasmon and electrical output characteristics of single crystalline metal nanowires, we have investigated the effect of electron flow on plasmon propagation in electrically contacted single crystalline metal nanowires. We find that surface plasmon characteristics are degraded by the morphological stress of the nanowire caused at the onset of electromigration. Even if we change the bias polarity, there is no evidence of the interference between the co-propagating electrons and surface plasmon before electromigration from Fourier plane analysis. We investigate the maximum current densities before electrical failure for silver and gold nanwoires and thus determined the operating limit for simultaneously propagating electrons and surface plasmon in the same one-dimensional metallic support.

Furthermore, we have compared the I-V characteristics of Ag and Au nanowires, we find that the residual surfactant employed for nanowires synthesis can affect the electrical characteristics and can be removed by an initial "burning-off" bias sweep. The different morphological change of silver and gold nanowire caused by the electromigration are compared and the different predominant forces in the electromigration for silver and gold nanowire were indicated.

## 3.5 Research prospect

### 3.5.1 Bias Modulation on nanowires

The above discussions indicate that there is no obvious interference between the synchronous electrons transport and surface plasmon propagation observed until onset of electromigration. However, it is possible that very subtle interferences were not detected by simply characterizing the Fourier plane of nanowire under DC bias. Therefore, we further investigated the possible crosstalk between co-propagating electrons and surface plasmons by modulating the electrical characteristics at different points of the electrical characteristics.

**Measurement setup**

The measurement is based on the functionality of a lock-in amplifier which extracts signal from noisy environment. Figure 3.22 schematically illustrates the principle of the measurement. A nanowire was excited at 810 nm wavelength. Surface plasmons propagating along the contacted nanowire was recorded with in the dual-plane measurement introduced in chapter 2. Light scattered at the end of the wire was collected with an avalanche photodiode (APD) in confocal manner. While surface plasmons were propagating along the nanowire, an sinusoidal AC bias generated by a function generator was slowly applied on the contacted electrodes.

Two lock-in amplifiers were used in our setup. The first lock-in amplifier extracts the photon counts received by the APD and was referenced to the repetition rate of the pulsed laser used in this measurement (80 MHz). The digital output of the APD (TTL logic) was hence converted to an analog signal by the lock-in amplifier. After calibration, the temporal variation of the lock-in voltage output is directly proportional to the count rate measured by the APD. The output of the first lock-in, measuring the magnitude of the light scattered by the end of the nanowire, is then fed to a second lock-in amplifier referenced to the AC bias voltage. The current flow was recorded with a home-made current-to-voltage converter (I-V converter) in a two-point configuration. The gain of the I-V converter is 0.1 V/mA and the cut-off frequency is 300 KHz.

We chopped the laser at a modulation frequency of 100 Hz to calibrate the output of the first lock-in amplifier with photon rate. Figure 3.23 shows the output of lock-in amplifier as a function of different laser power expressed as count rate measured from the APD. In this calibration step, an attenuated laser beam was directly sent to the APD. The sensitivity of the lock-in detection was evaluated by introducing noise in the measurement. The noise was provided by an unmodulated light source (tungsten lamp). A noise ratio of 100% indicates that the signal measure by the APD is solely coming from the tungsten lamp. The linear fitting (dashed line) shows a linear relation between the output of the APD and the lock-in amplifier signal. A very small modulated laser signal (noise ratio $\sim$ 99.96%) could be detected by the lock-in amplifier.

### 3.5.2 Results and discussions

We simultaneously recorded the electrical outputs, the APD signal issued from plasmon scattering events and the lock-in amplifier outputs for silver nanowires biased with an AC voltage. Figure 3.24 displays the results for two Ag nanowires biased with sinusoidal AC

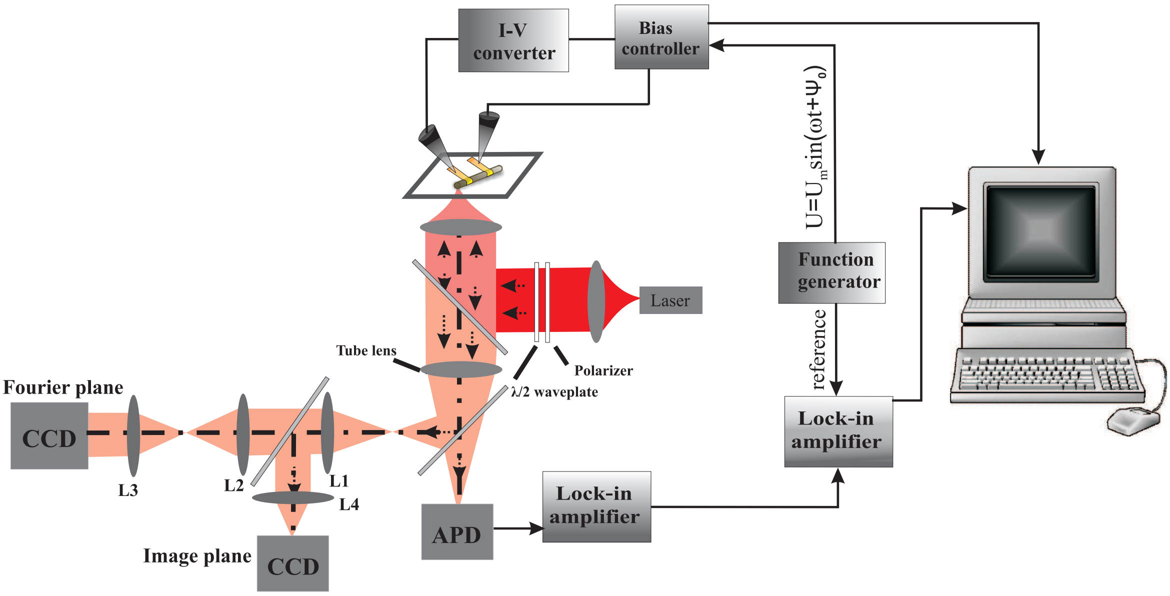

Fig 3.22: Schematic setup of AC bias modulation measurement. An AC bias is generated by the function generator. The plasmonic light signal collected by APD from the nanowire end was sent to two lock-in amplifiers. I-V characteristic is recorded by a home-made current/voltage converter.

voltage ($U = U_m \sin(2\pi\text{ft}{+}\varphi_0)$), where $U_m$=200 mV, f=120 Hz, $\varphi_0$ =0. The sensitivity range of lock-in amplifier is 10 V/50 $\mu$V. The electrical failure occurs at bias close to 2.5 V (black dashed line). An apparent drop of APD signal is observed when failure takes place. This apparent drop of APD signal has already been observed in image plane analysis displayed in Fig. 3.15(b). However, this intensity drop is not correlated to the modulated bias as indicated by the constant lock-in output.

A peak indicated with the red arrow appears in APD output right before the electrical breakdown of nanowire. Here too, there is no correlation with the referenced lock-in suggesting that morphological changes of the nanowire is likely to be responsible for a sudden increase of scattering.

In Fig. 3.24(b), the Ag nanowire electrically broke at 0.6 V. Interestingly, the output signal of the lock-in amplifier slightly drops down after the electrical breakdown. The slight drop down of lock-in signal indicates that there is a signal detected at 120 Hz. Although the APD output does not change after the electrical breakdown which may due to the alignment of APD detector, the lock-in output is very promising. Combining the results in Fig. 3.24(a), we can deduce that a crosstalk between the co-propagating electrons and surface plasmons may exist before the electrical breakdown of nanowires.

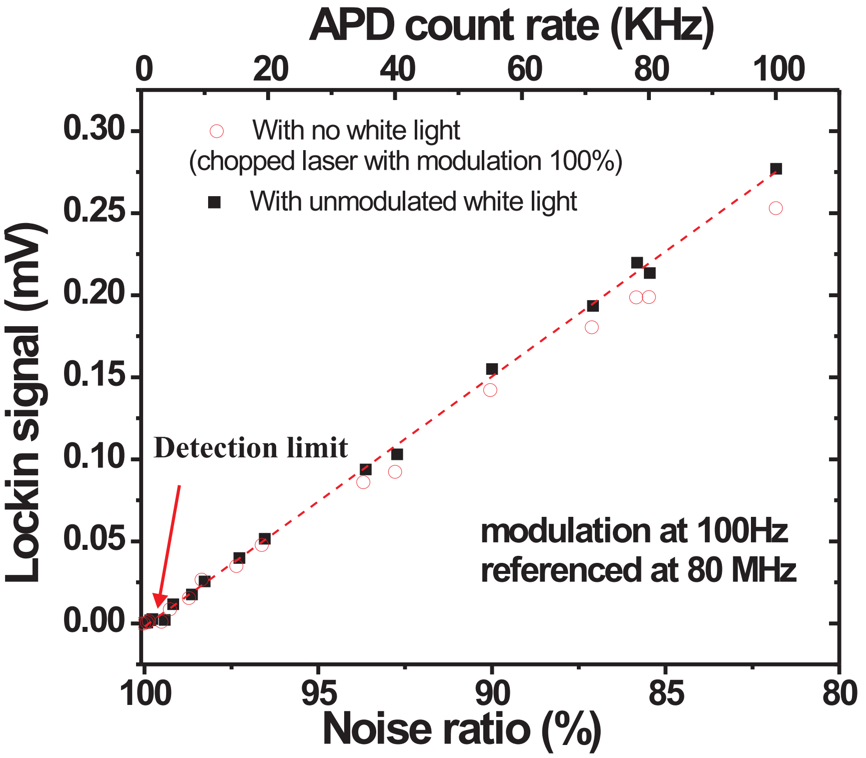

Fig 3.23: Lock-in output referenced at 80 MHz as a function of a count rate and noise ratio. The noise ratio is the ratio between the count rate of noise (only tungsten lamp) and the total count rate (count rate from laser + tungsten lamp). The chopping frequency is 100 Hz. The red arrow indicates the detection limit of the signal represented with a high noise ratio ∼ 99.96%.

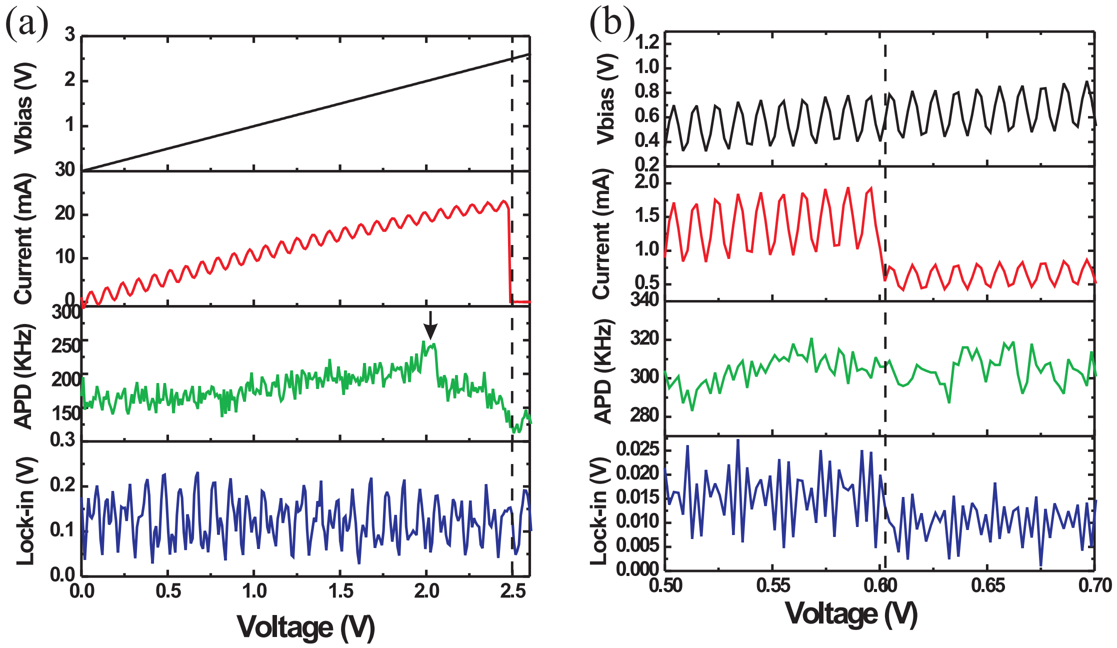

Fig 3.24: Electrical outputs, lock-in amplifier signals and APD count rate for silver nanowire under sinusoidal AC with $U_m$=200 mv, f=120 Hz, $\varphi_0$ =0. The black arrow indicates the apparent peak appearing right before the electrical breakdown of Ag nanowire. The black dashed lines mark the positions of the electrical breakdown of nanowires.

Due to the technical difficulty such as the relative larger size of APD detection window compared with the area of the nanowire distal end and the detection sensitivity of lock-in amplifier, we do not have conclusive results to indicate an interference between co-propagating electrons and surface plasmon. However, from Fig. 3.24, it is believed that the crosstalk between the co-propagation electrons and surface plasmon may be enhanced right before the electrical breakdown of nanowire during the electromigration. The mass flow during the electromigration and the stress resulting from the morphological change could be the reason for that. Then, another question arises: is it reversible? Can we modulate the effective index of surface plasmon mode by reversing the bias polarity?

According to our measurement on effective index in Fig. 3.15 and the calculations, the effective index drops during the electromigration and this drop is closely related to the morphological change. If we can stop the bias right before the electrical breakdown and switch the polarity, the morphological damage could be repaired and the effective index would go back to its normal value. Note that although we have already switched the bias polarity during our experiment and no significant difference was observed from the trend of effective index, in our measurement, bias was switched at the beginning and until the electrical breakdown occurs. We did not stop the bias and switch it before the electromigration. However, this morphology repairing by switching the bias has been investigated by Stahlmecke and his co-workers in Ref. [189]. They performed electromigration experiment on single crystalline silver nanowires using four points contact geometry. Void formation during the electromigration of nanowires with increasing current was observed using scanning electron microscope. Figure. 3.25 shows the results of a trapezoidal Ag nanowire. The current direction is indicated by the plus and minus signs. Nanowire in (a) is shown without any current applied. Nanowire in (b)-(e) was biased with increasing current 18 mA, 20 mA, 22 mA, 22 mA, respectively, and with shorter time 150 min, 120 min, 90 min and 30 min, respectively. These experimental parameters are in the consideration of overall experiment time. The enlarged images at the bottom clearly show the void formation during the different periods. The voids were formed at the positive side between the voltage and the current leads. When the current direction was reversed, the voids closed and new voids were formed at the positive side. Comparing (b) with (d) at the bottom, we can see that even within a short time, the closure is complete [189]. The shadows around the voids are due to the contamination introduced by SEM examinations. Considering this, the crosstalk between the co-propagating electrons and surface plasmons could be reduced by simply reversing the bias polarity.

Finally, the investigations on the crosstalk between co-propagating electrons and sur-

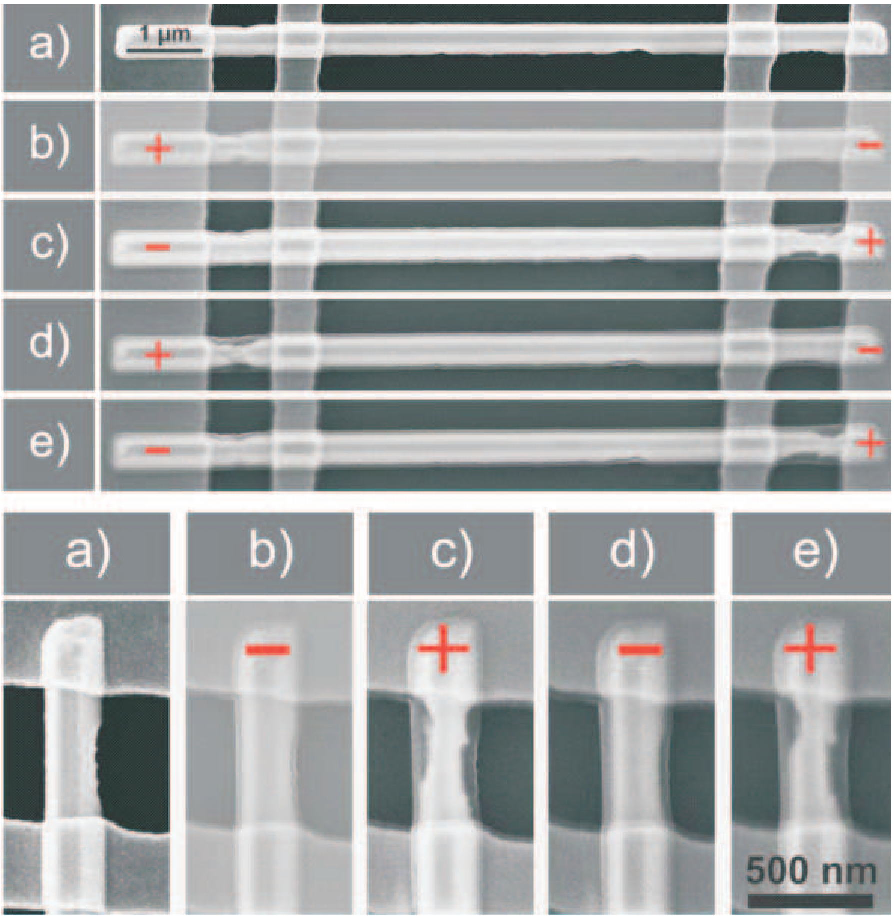

Fig 3.25: Void formation during the electromigration of a single crystalline Ag nanowire. Nanowire was applied with increasing current within decreasing time. Current direction is switched indicting by the plus and minus sign. Bottom: enlargement of the right contact area. Image extracted from Ref. [189].

face plasmons in our measurements were focused on the leaky mode. Although it is difficult to detect possible crosstalk for leaky mode, bound modes are expected to be more sensitive to surface rearrangement because their field is more confined to the metal surface. Cross-talk between current-carrying electrons and surface plasmons might therefore be more pronounced for this mode.

# Conclusions and perspectives

A plasmonic circuitry, capable of simultaneously transmitting electrons and surface plasmons shows potential for merging electronics and photonics at the nanoscale. The ability to guide surface plasmons and electrons on the same physical link provides for a seamless integration of an optical data processing level within an electronic control architecture.

As fundamental building blocks of a plasmonic circuitry, quasi-one dimensional structures like silver and gold metal nanowires are especially desirable due to their potential for realizing dense plasmonic and electronic routing networks. Metal nanowires therefore provide a platform for the development of passive and active optical components. The functionalities of these optical components and devices strongly rely on the properties of surface plasmons propagating along the nanowires.

We developed an imaging technique using dual-plane leakage radiation microscopy to directly measure the propagation properties of surface plasmons in Ag nanowires. By analyzing the wave vector distribution in Fourier plane images, we experimentally determined the effective indices and propagation losses for nanowires with diameters in the range from 120 nm to 500 nm.

Symmetry considerations derived from an analogy with the well-established molecular orbitals of cyclopentadienyl in numerical simulations allowed us to identify the modes existing in the crystalline Ag nanowires with a pentagonal cross section. The role of the substrate on the effective index values of the coupled corner plasmon modes was emphasized in the numerical simulations, and we have obtained a good agreement with the experimental values. We have also experimentally shown that distal tip scattering is introducing an additional decay channel contributing to the attenuation of the plasmon propagation. This observation suggests that a better control of the terminal facets of crystalline nanowires is desired in order to tune the tip scattering, which is a future challenge for colloidal chemists. Our investigations indicate that the precise morphological and structural features of crystalline colloidal metallic nanowires directly contribute to the design of the active plasmon modes. This opens a way to tune the optical properties of these nanostructures beyond the capabilities of lithographically fabricated devices. Relying on this unique approach, we have demonstrated that the leaky mode and bound modes can be selectively excited by the polarization inhomogeneities inside a focused laser spot. It therefore provides an easy way to tailor the plasmon mode needed for a given application.

The results obtained from our investigations on surface plasmon propagation properties in thick Ag nanowires provide the basic information for the exploitation of a plasmonic circuitry. With the improvement of the technology, another critical issue needs to be addressed concerning the properties of co-propagating electrons and surface plasmons. The interference between electrons and surface plasmons is rarely discussed. Therefore, on the basis of our experimental development, we investigated the effect of an electron flow on plasmon propagation in electrically contacted single crystalline silver nanowires. Surface plasmon characteristics and electrical output characteristics under direct current bias were synchronously recorded. We found that during electromigration, the effective index decreases and is accompanied by an increase of propagation loss. Numerical simulations showed that degraded surface plasmons characteristics are attributed to the morphological stress caused by the electromigration. We have thus determined the operating limit for simultaneously propagating electrons and surface plasmons in the same metal nanowire waveguide.

Although there was no clear-cut evidence indicating a crosstalk between co-propagating electrons and surface plasmons, we tried to modulate the current bias on contacted nanowires to detect an onset of interference. Our measurement was based on the functionality of lock-in amplifier to extract a signal at a referenced frequency from noisy background. At the current stage, we do not have enough results to determine the presence of the crosstalk. However our measurement shows some promising results. Our analysis focused on the interaction between the leaky plasmon mode and the current flow. Since we can selectively excited leaky mode and bound modes, larger coupling effect may be expected when bound modes are excited.

All the nanowires we measured were randomly deposited on the substrate. However, in a plasmonic circuitry, specifically oriented waveguide will be required. To achieve this directional distribution, we made initial steps at developing a technique to grow nanorods directly on a pre-patterned substrate by a surface-assisted growth mechanism. This work was performed in collaboration with E. Dujardin, in Toulouse. We have successfully achieved several *in-situ* growth of Au nanorods inside PMMA trenches shown in Fig. 3.26 (red circles). However, the yield of aligned nanorods is relatively low and some by-products

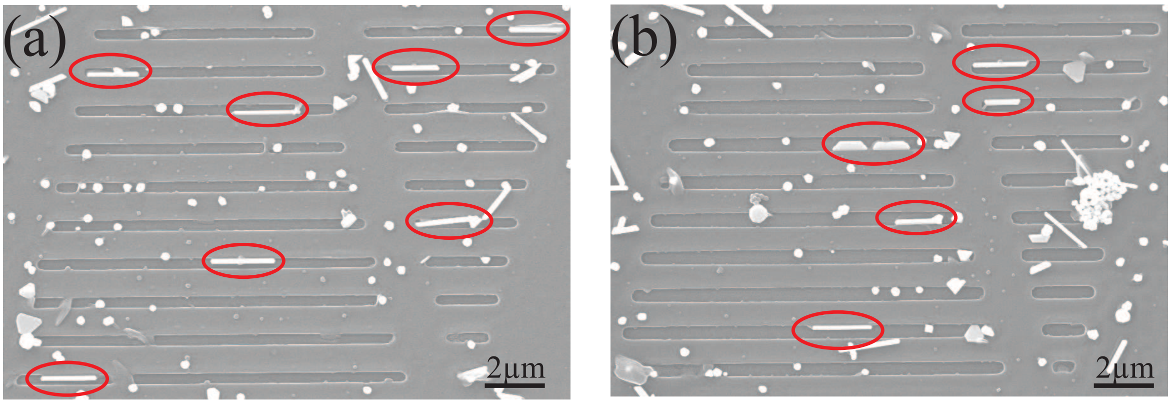

Fig 3.26: Gold nanorods synthesized directly inside the PMMA trenches. The well aligned nanorods are marked using red circles. Relatively large number of by-products were also synthesized inside and around the PMMA trenches.

also grew inside and around these PMMA trenches. Nanorods can be isolated by a simple lifting-off of the PMMA.

Convective assisted capillary force assembly (CA-CFA) technique is an alternative approach to align nanostructures at desired positions. The CA-CFA technique is based on the capability to overcome the Brownian motion in a colloidal suspension to deterministically position micro- or nanoparticles on a surface [191, 192, 193] and could be used in large-scale batch fabrication of plasmonic waveguides. The alignment of nanoparticles in well-defined patterns is obtained by a control of the evaporation of a colloidal drop in a confined medium. As a result, dimers with a wide range of interspacing distances or chains of nanoparticles or various shape may assembled on large patterns as illustrated in Fig. 3.27. In addition, CA-CFA can be used to align CdSe nanorods by applying an external electric field during the solvent evaporation after a drop-cast deposition across lithographically pre-patterned metal electrodes [194]. Both techniques provide a possible and self-assembled route to precisely deposit nanowires at desired positions.

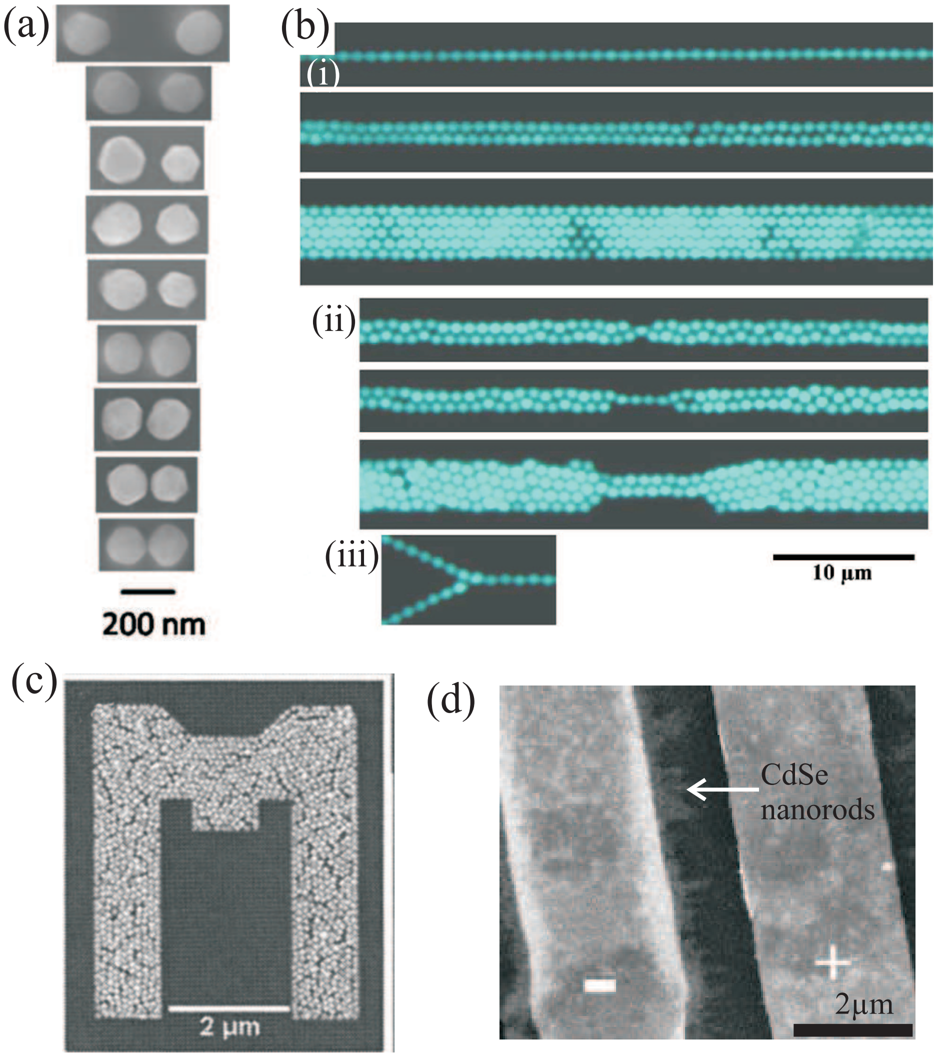

Fig 3.27: (a)-(c) Various structures assembled using CA-CFA technique: (a) SEM images of individual dimers with an interdistance $d$ =230, 70, 60, 54, 40, 30, 20, 11, 7, and 0 nm (from top to bottom). Images extracted from Ref. [195]. (b) Fluorescence micrographs of long colloidal chains with (i) variable widths, (ii) bottleneck functions, and (iii) three-arm fork function. Images extracted from Ref. [193]. (c) Large pattern assembled by Au colloids. Images extracted from Ref. [191]. (d) Micrograph of the assembly obtained after the DC electric field (E = $1.75 \times 10^7$ V/m) driven alignment of the nanorods drop-casted from a p-xylene dispersion on the 2 $\mu$m gap. Images extracted from Ref. [194].

# Annex

# Characterization of carbon contamination

## Carbon contamination

Scanning electron microscopy (SEM) is a very common technique that is used to characterize the specimen structure. It images a sample by scanning it with a beam of electrons in a raster scan pattern. The electrons interact with the atoms from the specimen producing signals that contain information about the specimen's surface topography, composition, and other properties such as electrical conductivity. However, an inevitable problem is the carbon contamination introduced during the imaging process. The presence of carbon residues in the vacuum chamber from the pump oil, inadvertent touching of the specimen and the specimen holder [196] interact with the electron beam generating hydrocarbon compounds at the surface of the specimen being imaged. Although this carbon uptake can be carefully controlled for fabricating nanotips for field emission [197, 198, 199] or as a negative resist mask [200], it will gradually reduce the imaging contrast and will causing artefacts in spectroscopy [201]. This especially important in the field of plasmonics where the optical response of nanostructures are extremely sensitive to surface adsorbate [31, 38].

In this annex, we have investigated the effect of carbon contamination introduced during SEM imaging on the resonance peak of gold nanoparticles.

## Sample fabrication

Gold nanoparticle arrays were fabricated using standard electron electron beam lithography. The design of the structure is shown in Fig. 28(a). There are 9 nanoparticles in each row. The row at the bottom without any number marked are dummy nanoparticles used to extract geometrical parameters. The first particles on the left of each row in the red

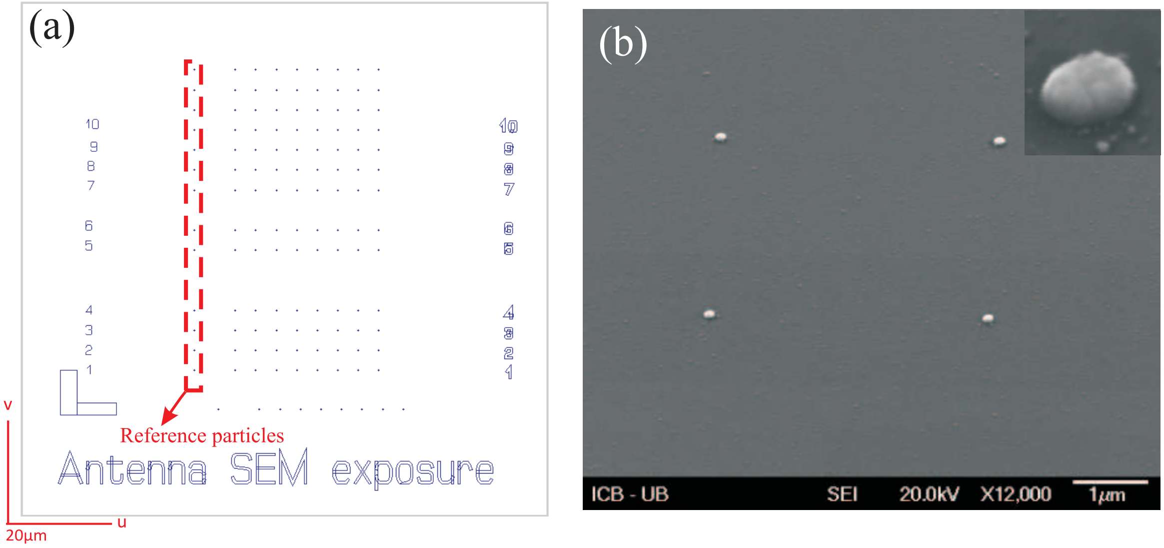

Fig 28: (a) Design of the nanoparticles array. The first nanoparticle on the left of each row is used as a reference structure. (b) SEM image of four Au particles in the array. Inset: close up image of a Au nanoparticle.

dashed box are taken as reference nanoparticles and will not be exposed to the electron beam. The spacing between nanoparticles in each row is 8 $\mu$m while the spacing between rows is 4 $\mu$m. An SEM image in Fig. 28(b) shows four Au particles in the array. The close up image of one particle is shown in the inset of Fig. 28(b). All the nanoparticles in the array have the same diameter ~125 nm and thickness ~50 nm.

## Spectrum measurement

The principle of measurement is schematically shown in Fig. 29. A white light from a tungsten lamp is passing through a dark field condenser ($0.8< N.A. <0.95$) and is focused on metal nanoparticle array. The scattered light from the particles is then collected with an objective (40×, N.A.=0.65) and then sent to an imaging spectrograph by two relay lens with same focal length 100 mm.

First, the spectrum of each nanoparticle without electron-beam irradiation was taken one by one. This can be achieved by reducing the size of the slit on the spectrograph (confocal-like detection). In our measurement, the two-dimensional CCD chip used allows us to take the spectra from a complete row of nanoparticles at a time. Once the individual spectra of the nanoparticles constituting the array were taken, the surface of each particle

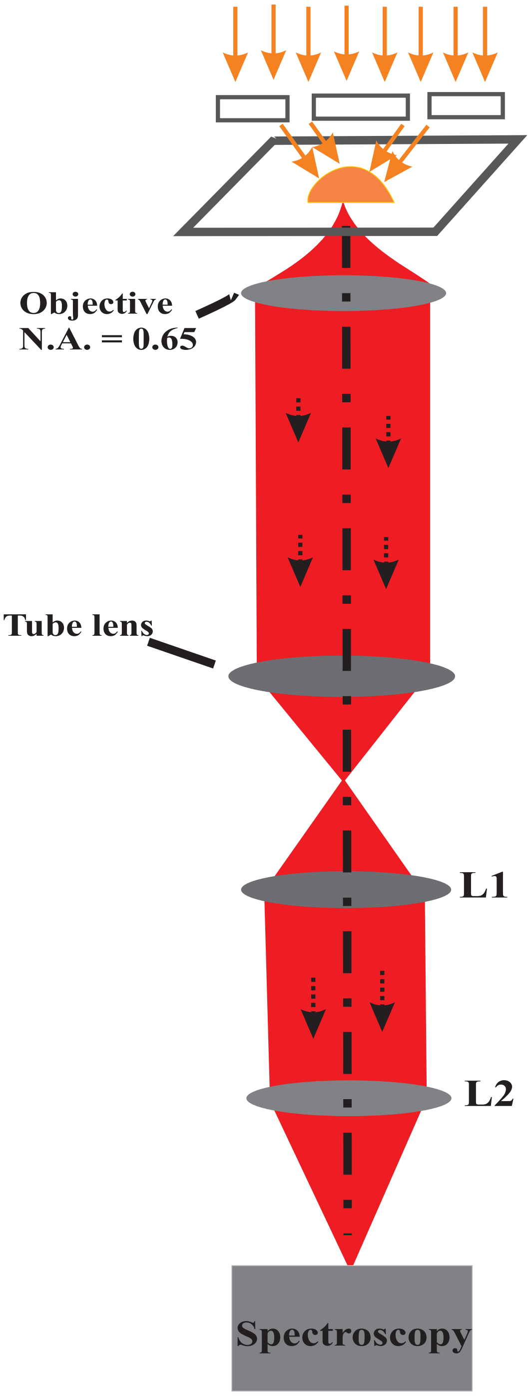

Fig 29: Setup of dark-field microscopy. Light scattered from the particles is collected with an objective (N.A.=0.65) and are focused by two relay lens (focal length 100 mm) and sent to the spectrograph.

was purposely exposed to the electron beam with different doses. In order to compare the peak wavelength of the resonance for a nanoparticle before and after exposure contamination, an area at the right end of each row was irradiated with the same dose used to irradiate the nanoparticles. The exposure dose for each row is illustrated in the following table.

Table 1: Exposure dose: Doses were increased either at constant current and increasing exposure time, or by changing the current of the electron beam.

| Row | Current (nA) | Time (s) | Dose (nA.s) |
|---|---|---|---|
| 1 | 0.885 | 5 | 4.425 |
| 2 | 0.885 | 10 | 8.85 |
| 3 | 0.885 | 15 | 13.275 |
| 4 | 0.885 | 20 | 17.7 |
| 5 | 0.229 | 5 | 1.145 |
| 6 | 0.229 | 10 | 2.29 |
| 7 | 0.229 | 15 | 3.435 |
| 8 | 0.229 | 20 | 4.58 |
| 9 | 0.089 | 5 | 0.445 |
| 10 | 0.089 | 10 | 0.89 |
| 11 | 0.089 | 15 | 1.335 |
| 12 | 0.089 | 20 | 1.78 |

Then the spectra of all nanoparticles contaminated by the electron beam were taken and compared to the original spectra of the pristine nanoparticles. The spectrum of the unexposed nanoparticle (without exposure) was measured again in order to confirm that the reference spectra before and after contamination was the same.

# Results and discussion

Figure. 30(a) and (b) display the background-corrected hyperspectral image of 9 adjacent Au nanoparticles before and after electron-beam exposure, respectively. The exposure dose is 13.275 nA.s. The first line on the left of both images is the spectrum of reference particle. Due to the resonance shift of the particle before and after exposure, the spectra were taken using a different center wavelength: 720 nm and 700 nm for the measurement before and after, respectively. The spectrum of the irradiated area (no nanoparticle)

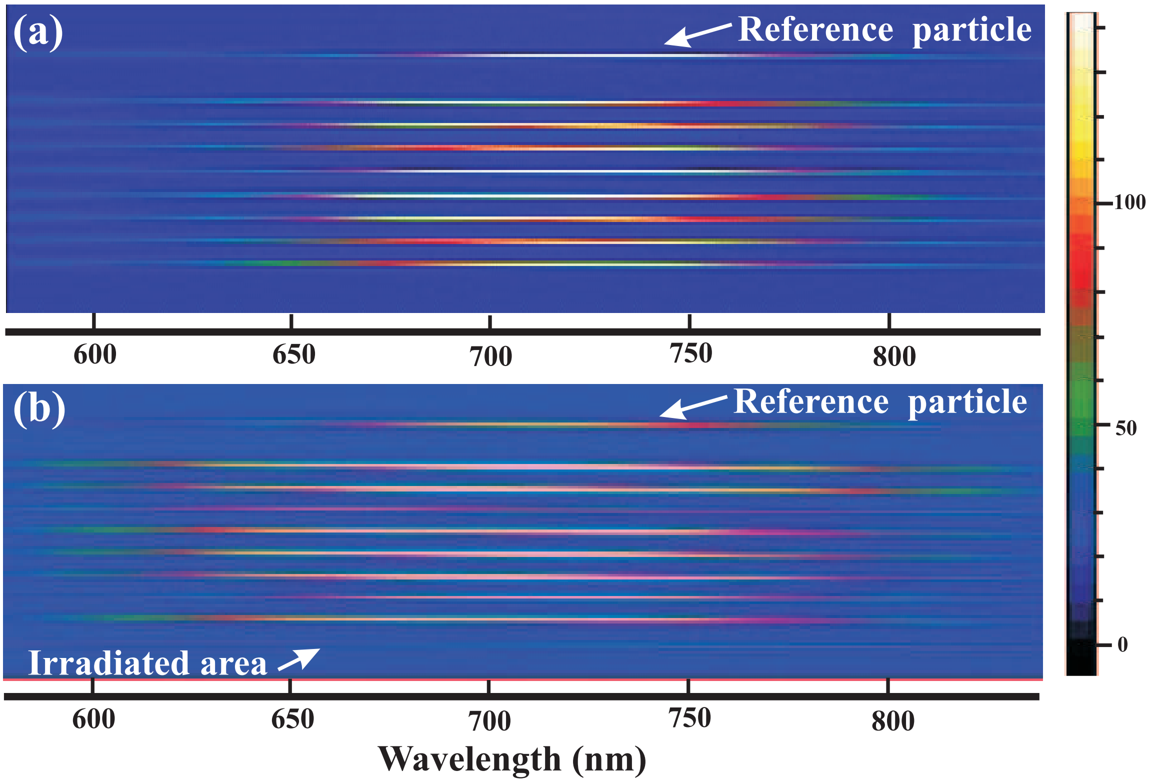

Fig 30: Measured spectra of Au particles in one row before electron exposure (a) and after exposure (b). They were taken at center wavelength 720 nm (a) and 700 nm (b), respectively.

is readily seen on the right side in Fig. 30(b). Interestingly, the light scattered off the exposure area presents a resonance-like shape with a maximum at 714 nm as inferred by the Gaussian fit in Fig. 31(a). The spectra strongly resembles to the plasmonic response of a unexposed metal nanoparticle. This implies that the spectrum measured from an irradiated nanoparticle is a linear combination of the particle' response and that of the residues.

We found that peak wavelength of the irradiated area depends of the exposure dose. Figure 31(b) suggests that the peak wavelength of the exposed surface increases with increasing dose.

The difference of the resonance wavelength for each Au particle before and after irradiation was analyzed by performing a Gaussian fitting procedure of the spectra. The resonance wavelength of the pristine particles $< \lambda_o >$ was obtained by taking the average spectra of the 9 nanoparticles forming the same row, including the reference system. The resonance wavelength of the particle after contamination $< \lambda_c >$ was obtained by taking

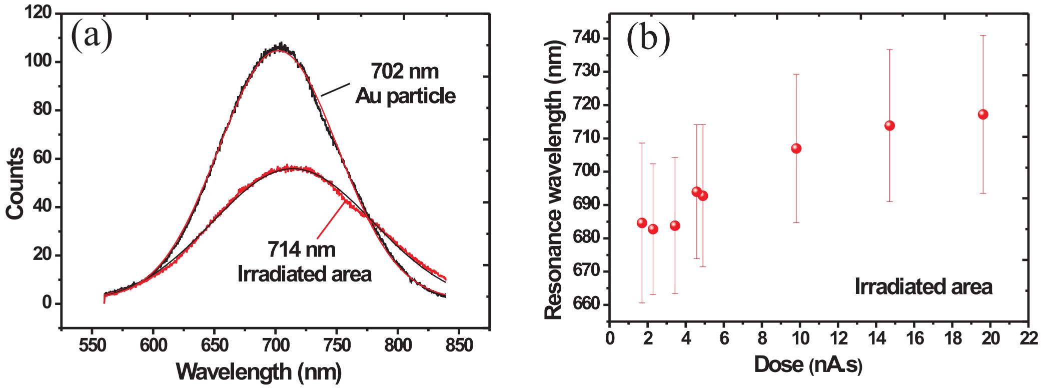

Fig 31: (a) Extracted spectra of a Au particle and a contamination dot. The spectrum of the contamination dot strongly resembles that of a metal nanoparticle. (b) Resonance wavelength of contamination carbon dot. The error bars are given by the Gaussian fit.

the average of the 8 particles that were exposed to the electron beam. The difference resonance wavelength $\lambda_D$ for Au particles without and with contamination is thus defined as $\lambda_D =< \lambda_o > - < \lambda_c >$. The results are plotted as a function of exposure dose in Fig. 32 where $\lambda_D < 0$ indicates a redshift of the resonance after exposure and $\lambda_D < 0$ a blue-shift. For the smallest exposure dose, the resonance wavelength of Au particles has redshifted compared to the pristine nanoparticle as expected from the adhesion of surface adsorbates [202, 203]. For doses up to 10 nA.s, $\lambda_D$ linearly increases with doses indicating a systematic blue-shift of the resonance to reach a plateau at a detuning $\lambda_D$=13 nm.

In order to explain this unexpected behaviour, Au particles were observed using SEM before and after electron-beam irradiation. We show in Fig. 33 SEM images of four Au particles before (a) and after electron beam exposure (b) with dose 13.275 nA.s and 17.7 nA.s, respectively. To our surprise, small depressions are appearing at the surrounding of the nanoparticles. The size of depression gets deeper with increasing dose. This concave surface is not understood at the moment but could be attributed to the deformation of the interface resulting from the electron beam. A close up view of one nanoparticle with a depression around is shown in Fig. 33(c). The surface of the particle is also slightly indented. In Fig. 33(d), the depression site is readily observed $\sim 2.5\mu$m at the right of the nanoparticle. At that location, the substrate was irradiated by the electron beam with the same exposure dose as the particle.

In order to know the exposure dose that formed the contamination dots and depres-

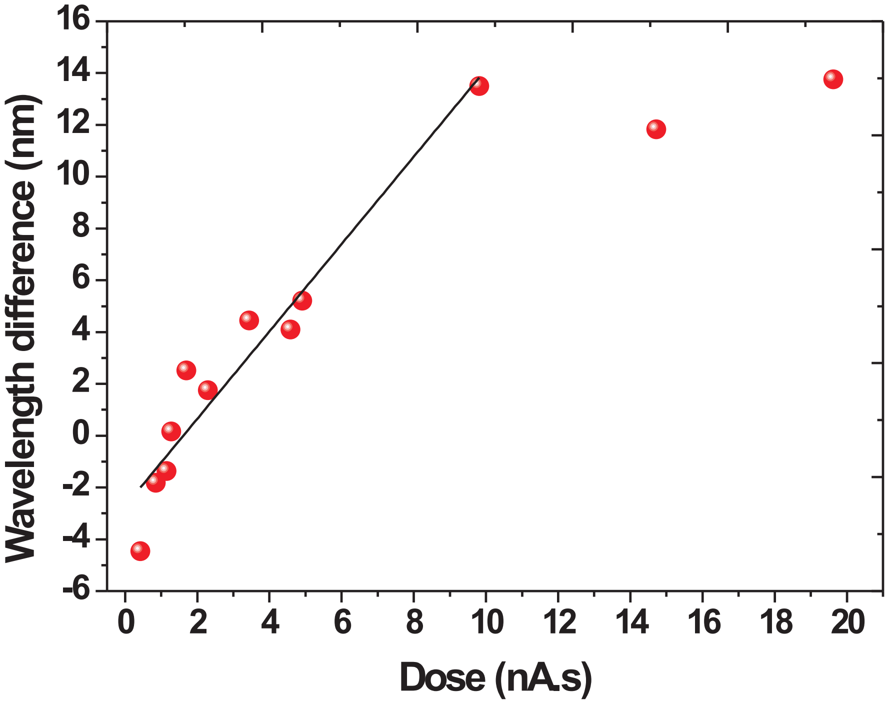

Fig 32: Difference resonance wavelength $\lambda_D$ between nanoparticles before and after electron exposure. It is obtained by using the average resonance wavelength of pristine particles subtracted from the average resonance wavelength of the same nanoparticles after irradiation. The black line is a linear fit.

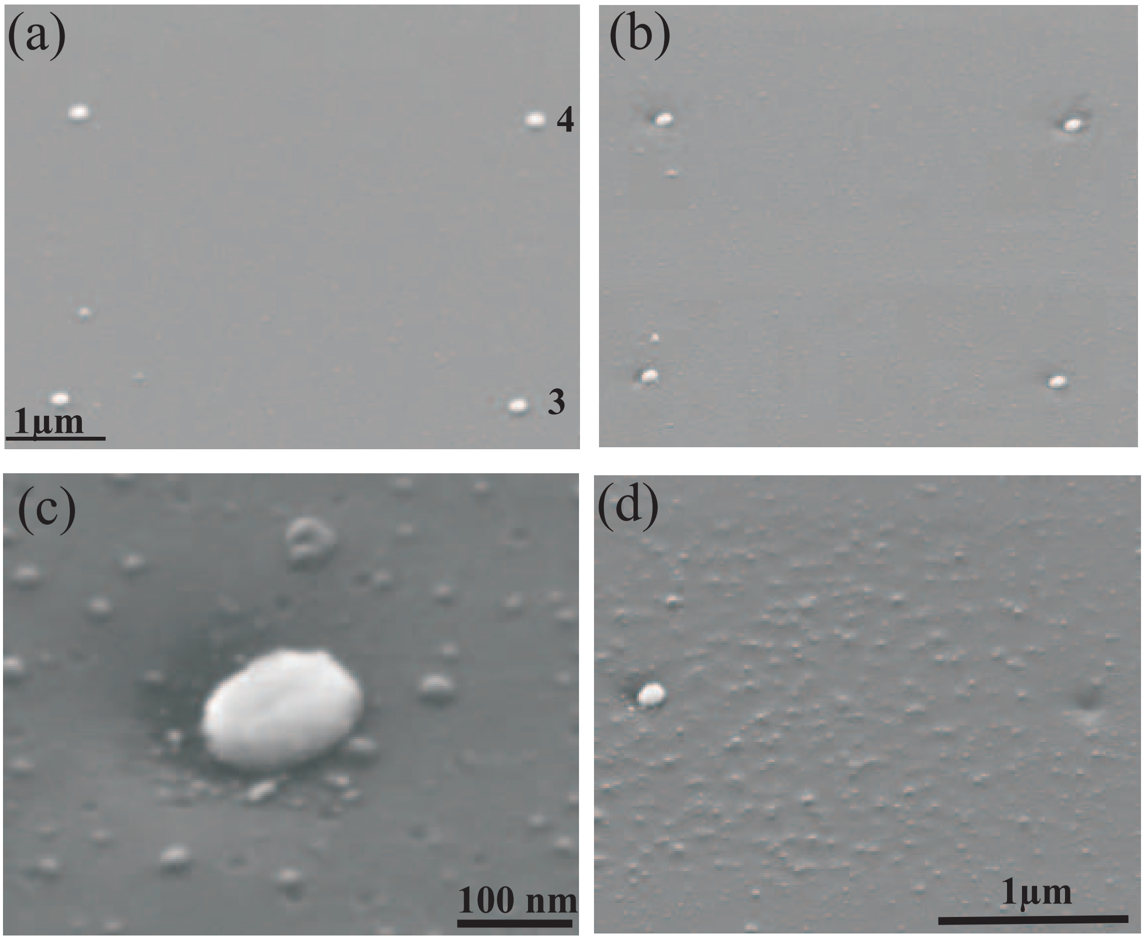

Fig 33: SEM images of four Au pristine nanoparticles (a) and after electron exposure (b). (c) The close up image of one Au particle after the irradiation showing a hollow at the surrounding of the particle. (d) SEM image of a Au particle and the hollow formed on its right side under the same exposure dose.

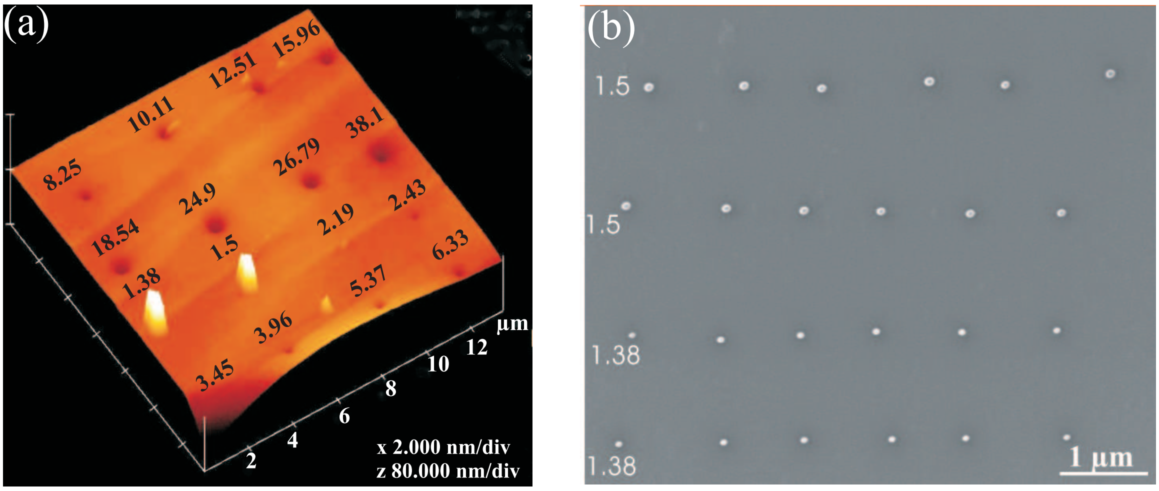

Fig 34: (a) 3D AFM image shows the formation of carbon contamination tips and depressions with different exposure dose. The numbers represent the exposure dose. (b) SEM image of contamination dots deposited on ITO with exposure dose 1.38 nA.s and 1.5 nA.s.

sions, we tried to deposit an array of contamination dots directly on the surface of indium tin oxide glass (ITO) using different exposure doses. We changed the exposure current while keeping the exposure time constant at 30 s. The exposure dose is changing from 1.38 nA.s to 38.1 nA.s. The 3D AFM image in Fig. 34(a) shows the surface morphology of the surface after exposure to the electron beam. The exposure dose is marked on the top of each position. It is clearly to see that with lower exposure dose (1.38 nA.s, 1.5 nA.s in third row of the AFM image), carbon tips are formed. When the dose increases to 2.19 nA.s, as small protrusion remains visible. A small depression was formed with exposure dose 2.43 and the depression becomes deeper and larger as the dose increases. A SEM image of the carbon contamination dots formed with exposure dose 1.38 and 1.5 nA.s on the surface of ITO is shown in Fig. 34(b) indicating the robustness of the contamination. The carbon dots formed with exposure dose 1.5 nA.s are slightly larger than those formed with exposure dose 1.38 nA.s. Figure 35 displays the height of the carbon tips and the depressions in Fig. 34(a). As the exposure dose increases, the height of contamination dots decreases and starts to form a depression at around dose of 3 nA.s. The depth of the depression becomes deeper as the exposure dose increases.

From the above considerations, we can then conclude that when the exposure dose is small, carbon contamination tips formed on the top surface of the Au particle introduce a small but measurable red-shift of the plasmon resonance. Since the resonance of metal

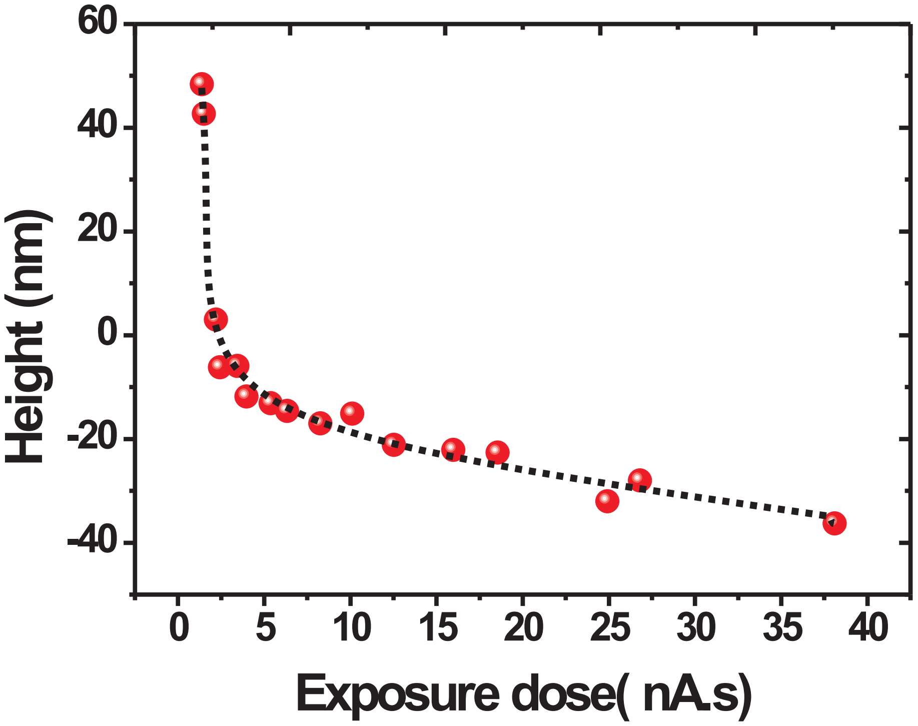

Fig 35: Height of carbon tips and depressions formed using different exposure dose on the surface of ITO.

nanostructures is affected by the dielectric environment [38, 202], this redshift is a modified electrical environment attributed to the hydrocarbon adsorbate. However, as the exposure dose increases, the electron beam is no longer depositing carbon residues and contribute to the desorption of the contamination. At approximatively 3 nA.s, the position of the resonance shows that the nanoparticle before and after electron-beam exposure is the same. This exposure dose defines the optimal imaging condition for observing plasmonic nanoparticles without altering their spectroscopic properties. For larger exposure, the geometry of the interface is changed to a concave surface. The blue-shift of the resonance is therefore understood as either a linear combination of the scattering response of the indentation convoluted with that of the nanoparticle, or a modified interface from a planar surface to a concave geometry. Numerical simulation and proper normalization of the scattered light from the irradiated surface should help at distinguishing the two effects.

## Conclusion

The effect of electron-beam exposure on the response of plasmonic nanoparticles upon imaging with SEM was investigated in this annex. The spectra obtained for Au particles before and after irradiation indicated the presence of carbon contamination on the surface of the particle for smaller exposure dose ($< 3$ nA.s). When the exposure dose increases, AFM and SEM imaging demonstrate that the surface of substrate around Au particles is deformed by the electron beam forming a depression. Under these exposure conditions, the surface plasmon resonance of the nanoparticle systematically blue-shifts. An optimum dose is therefore determined to safely image plasmonic nanostructure with SEM.

# Bibliography

[1] D.K. Gramotnev and S.I. Bozhevolnyi. Plasmonics beyond the diffraction limit. *Nat. Photonics*, 4(2):83–91, 2010.

[2] R. Zia, J.A. Schuller, A. Chandran, and M.L. Brongersma. Plasmonics: the next chip-scale technology. *Mater. Today*, 9(7):20–27, 2006.

[3] D. Peyrade, Y. Chen, L. Manin-Ferlazzo, A. Lebib, N. Grandjean, D. Coquillat, R. Legros, and J.P. Lascaray. Fabrication of gan photonic crystals for 400 nm wavelength. *Microelectron. Eng.*, 57:843–849, 2001.

[4] J.D. Joannopoulos, P.R. Villeneuve, and S. Fan. Photonic crystals: putting a new twist on light. *Nature*, 386(6621):143–149, 1997.

[5] M.P. Bernal, J. Amet, J. Safioui, F. Devaux, M. Chauvet, J. Salvi, and FI Baida. Pyroelectric control of the superprism effect in a lithium niobate photonic crystal in slow light configuration. *Appl. Phys. Lett.*, 98:071101, 2011.

[6] M. Roussey, M.P. Bernal, N. Courjal, D. Van Labeke, FI Baida, and R. Salut. Electro-optic effect exaltation on lithium niobate photonic crystals due to slow photons. *Appl. Phys. Lett.*, 89:241110, 2006.

[7] J. Amet, FI Baida, GW Burr, and M.P. Bernal. The superprism effect in lithium niobate photonic crystals for ultra-fast, ultra-compact electro-optical switching. *Photonics and Nanostructures-Fundamentals and Applications*, 6(1):47–59, 2008.

[8] M. Roussey, F.I. Baida, and M.P. Bernal. Experimental and theoretical observations of the slow-light effect on a tunable photonic crystal. *JOSA B*, 24(6):1416–1422, 2007.

[9] M. Belotti, J.F. Galisteo Lòpez, S. De Angelis, M. Galli, I. Maksymov, L.C. Andreani, D. Peyrade, and Y. Chen. All-optical switching in 2d silicon photonic crystals

with low loss waveguides and optical cavities. *Opt. Express*, 16(15):11624–11636, 2008.

[10] B.E.A. Saleh, M.C. Teich, and B.E. Saleh. *Fundamentals of photonics*, volume 22. Wiley Online Library, 1991.

[11] S.A. Maier, M.L. Brongersma, P.G. Kik, S. Meltzer, A.A.G. Requicha, B.E. Koel, and H.A. Atwater. Plasmonics-a route to nanoscale optical devices. *Adv. Mater.*, 15(7-8):1501–1505, 2001.

[12] J.R. Krenn, B. Lamprecht, H. Ditlbacher, G. Schider, M. Salerno, A. Leitner, and F.R. Aussenegg. Non-diffraction-limited light transport by gold nanowires. *Mater. Today*, 60(5):663–669, 2002.

[13] H.A. Atwater. The promise of plasmonics. *Sci. Am.*, 296(4):56–62, 2007.

[14] H. Raether. *Surface plasmons*. Springer-Verlag Berlin, 1988.

[15] M. Dragoman and D. Dragoman. Plasmonics: Applications to nanoscale terahertz and optical devices. *Prog. Quantum Electron.*, 32(1):1–41, 2008.

[16] G. Schider A. Hohenau A. Leitner F. R. Aussenegg J. R. Krenn, H. Ditlbacher. Surface plasmon micro- and nano-optics. *J. Microscopy*, 209(3):167–172, 2003.

[17] R.H. Ritchie. Plasma losses by fast electrons in thin films. *Phys. Rev.*, 106:874–881, Jun 1957.

[18] DL Mills and E. Burstein. Polaritons: the electromagnetic modes of media. *Reports on Progress in Physics*, 37:817, 1974.

[19] S.A. Maier. Plasmonics-towards subwavelength optical devices. *Current Nanoscience*, 1(1):17–22, 2005.

[20] W.L. Barnes. Surface plasmon–polariton length scales: a route to sub-wavelength optics. *Journal of Optics A: Pure and Applied Optics*, 8:S87, 2006.

[21] S.A. Maier. *Plasmonics: fundamentals and applications*. Springer Verlag, 2007.

[22] E. Ozbay. Plasmonics: Merging photonics and electronics at nanoscale dimensions. *Science*, 311(5758):189–193, 2006.

[23] W.L. Barnes, A. Dereux, and T.W. Ebbesen. Surface plasmon subwavelength optics. *Nature*, 424(14):824–830, 2003.

[24] T.W. Ebbesen, C. Genet, and S.I. Bozhevolnyi. Surface-plasmon circuitry. *Phys. Today*, 61(5):44–50, 2008.

[25] J. A. Conway, S. Sahni, and T. Szkopek. Plasmonic interconnects versus conventional interconnects: a comparison of latency, crosstalk and energy costs. *Opt. Express*, 15(8):4474–4484, 2007.

[26] A.L. Pyayt, B. Wiley, Y. Xia, A. Chen, and L. Dalton. Integration of photonic and silver nanowire plasmonic waveguides. *Nat. Nanotechnol.*, 3(11):660–665, 2008.

[27] M. Mansuripur, A.R. Zakharian, A. Lesuffleur, S.H. Oh, R.J. Jones, N.C. Lindquist, H. Im, A. Kobyakov, and J.V. Moloney. Plasmonic nano-structures for optical data storage. *Opt. Express*, 7505:14001–14014, 2009.

[28] K.P. Chiu, K.F. Lai, and D.P. Tsai. Application of surface polariton coupling between nano recording marks to optical data storage. *Opt. Express*, 16(18):13885–13892, 2008.

[29] K. Kneipp, M. Moskovits, and H. Kneipp. Surface-enhanced raman scattering. *Phys. Today*, 60(11):40–46, 2007.

[30] A. Kinkhabwala, Z. Yu, S. Fan, Y. Avlasevich, K. Müllen, and W.E. Moerner. Large single-molecule fluorescence enhancements produced by a bowtie nanoantenna. *Nat. Photonics*, 3(11):654–657, 2009.

[31] H. Portales, L. Saviot, E. Duval, M. Gaudry, E. Cottancin, M. Pellarin, J. Lermé, and M. Broyer. Resonant raman scattering by quadrupolar vibrations of ni-ag core-shell nanoparticles. *Physical Review B*, 65(16):165422, 2002.

[32] J. Margueritat, H. Gehan, J. Grand, G. Liévi, J. Aubard, N. Fiélidj, A. Bouhelier, G. Colas-Des-Francs, L. Markey, C. Marco De Lucas, et al. Influence of the number of nanoparticles on the enhancement properties of surface-enhanced raman scattering active area: sensitivity versus repeatability. *ACS nano*, 2011.

[33] J. Margueritat, J. Gonzalo, CN Afonso, U. Hörmann, G. Van Tendeloo, A. Mlayah, DB Murray, L. Saviot, Y. Zhou, MH Hong, et al. Surface enhanced raman scat-

tering of silver sensitized cobalt nanoparticles in metal–dielectric nanocomposites. *Nanotechnology*, 19:375701, 2008.

[34] G. Colas Des Francs, A. Bouhelier, E. Finot, J.C. Weeber, A. Dereux, C. Girard, E. Dujardin, et al. Fluorescence relaxation in the near-field of a mesoscopic metallic particle: distance dependence and role of plasmon modes. *Opt. Express*, 16:17654, 2008.

[35] F. Keilmann. Surface-polariton propagation for scanning near-field optical microscopyapplication. *J. Microscopy*, 194(2-3):567–570, 1999.

[36] M.I. Stockman. Nanofocusing of optical energy in tapered plasmonic waveguides. *Phys. Rev. Lett.*, 93(13):137404, 2004.

[37] J. Homola, S.S. Yee, and G. Gauglitz. Surface plasmon resonance sensors: review. *Sens. Actuators, B*, 54(1-2):3–15, 1999.

[38] G. Barbillon, J.L. Bijeon, J. Plain, M.L. de la Chapelle, P.M. Adam, and P. Royer. Biological and chemical gold nanosensors based on localized surface plasmon resonance. *Gold Bulletin*, 40(3):240–244, 2007.

[39] G. Barbillon, J.L. Bijeon, J. Plain, and P. Royer. Sensitive detection of biological species through localized surface-plasmon resonance on gold nanodisks. *Thin Solid Films*, 517(9):2997–3000, 2009.

[40] M.D. Kelzenberg, D.B. Turner-Evans, B.M. Kayes, A. Michael, M.C. Putnam, N.S. Lewis, and H.A. Atwater. Photovoltaic measurements in single-nanowire silicon solar cells. *Nano Lett.*, 8(2):710–714, 2008.

[41] H.A. Atwater and A. Polman. Plasmonics for improved photovoltaic devices. *Nat. Mater.*, 9(3):205–213, 2010.

[42] M.L. Brongersma, J.W. Hartman, and H.H. Atwater. Plasmonics: Electromagnetic energy transfer and switching in nanoparticle chain-arrays below the diffraction limit. *Mater. Res. Soc. Symp. Proc.*, 582:H10.5, 1999.

[43] J.A. Schuller, E.S. Barnard, W. Cai, Y.C. Jun, J.S. White, and M.L. Brongersma. Plasmonics for extreme light concentration and manipulation. *Nat. Mater.*, 9(3):193–204, 2010.

[44] S. Lal, S. Link, and N.J. Halas. Nano-optics from sensing to waveguiding. *Nat. Photonics*, 1(7):641–648, 2007.

[45] R.M. Dickson and L.A. Lyon. Unidirectional plasmon propagation in metallic nanowires. *J. Phys. Chem. B*, 104(26):6095–6098, 2000.

[46] S.I. Bozhevolnyi. *Plasmonic Nano-Guides and Circuits*. 2008.

[47] K. Hassan, J.C. Weeber, L. Markey, A. Dereux, A. Pitilakis, O. Tsilipakos, and E.E. Kriezis. Thermo-optic plasmo-photonic mode interference switches based on dielectric loaded waveguides. *Appl. Phys. Lett.*, 99(24):241110–241110, 2011.

[48] J.R. Salgueiro and Y.S. Kivshar. Nonlinear couplers with tapered plasmonic waveguides. *Opt. Express*, 20(9):9403–9408, 2012.

[49] E.N. Economou. Surface plasmons in thin films. *Phys. Rev.*, 182(2):539–554, 1969.

[50] J.J. Burke and G.I. Stegeman. Surface-polariton-like waves guided by thin, lossy metal films. *Phys. Rev. B*, 33(8):5186–5201, 1986.

[51] P. Berini. Plasmon-polariton waves guided by thin lossy metal films of finite width: Bound modes of asymmetric structures. *Phys. Rev. B*, 63(12):125417, 2001.

[52] J.R. Krenn and J.C. Weeber. Surface plasmon polaritons in metal stripes and wires. *Phil. Trans. R. Soc.*, 362(1817):739–756, 2004.

[53] J.C. Weeber, J.R. Krenn, A. Dereux, B. Lamprecht, Y. Lacroute, and J.P. Goudonnet. Near-field observation of surface plasmon polariton propagation on thin metal stripes. *Phys. Rev. B*, 64(4):045411, 2001.

[54] B. Lamprecht, J.R. Krenn, G. Schider, H. Ditlbacher, M. Salerno, N. Felidj, A. Leitner, F.R. Aussenegg, and J.C. Weeber. Surface plasmon propagation in microscale metal stripes. *Appl. Phys. Lett.*, 79(1):51–53, 2009.

[55] K. Leosson, T. Nikolajsen, A. Boltasseva, and S.I. Bozhevolnyi. Long-range surface plasmon polariton nanowire waveguides for device applications. *Opt. Express*, 14(1):314–319, 2006.

[56] J.P. Kottmann, O.J.F. Martin, D.R. Smith, and S. Schultz. Dramatic localized electromagnetic enhancement in plasmon resonant nanowires. *Chem. Phys. Lett.*, 341(1-2):1–6, 2001.

[57] M. Quinten, A. Leitner, J.R. Krenn, and F.R. Aussenegg. Electromagnetic energy transport via linear chains of silver nanoparticles. *Opt. Lett.*, 23(17):1331–1333, 1998.

[58] S.A. Maier and H.A. Atwater. Plasmonics: Localization and guiding of electromagnetic energy in metal / dielectric structures. *J. Appl. Phys.*, 98(1):1951057, 2005.

[59] S.A. Maier, M.D. Friedman, P.E. Barclay, and O. Painter. Experimental demonstration of fiber-accessible metal nanoparticle plasmon waveguides for planar energy guiding and sensing. *Appl. Phys. Lett.*, 86:071103, 2005.

[60] C. Sönnichsen, A.C. Duch, G. Steininger, M. Koch, G. Von Plessen, and J. Feldmann. Launching surface plasmons into nanoholes in metal films. *Appl. Phys. Lett.*, 76(2):140, 2000.

[61] H. Gao, J. Henzie, and T.W. Odom. Direct evidence for surface plasmon-mediated enhanced light transmission through metallic nanohole arrays. *Nano Lett.*, 6(9):2104–2108, 2006.

[62] H. Fujii, S. Kanemaru, H. Hiroshima, S.M. Gorwadkar, T. Matsukawa, and J. Itoh. Fabrication and characterization of a nanogap edge emitter with a silicon-on-insulator wafer. *Appl. Surf. Sci.*, 146(1-4):203–208, 1999.

[63] K. Tanaka, M. Tanaka, and T. Sugiyama. Simulations of nanometric optical circuits based on surface plasmon polariton gap waveguide. *Appl. Phys. Lett.*, 82(8):1158, 2003.

[64] D.F.P. Pile, T. Ogawa, D.K. Gramotnev, Y. Matsuzaki, K.C. Vernon, K. Yamaguchi, T. Okamoto, M. Haraguchi, and M. Fukui. Two-dimensionally localized modes of a nanoscale gap plasmon waveguide. *Appl. Phys. Lett.*, 87(26):261114, 2005.

[65] S.I. Bozhevolnyi, V.S. Volkov, E. Devaux, and T.W. Ebbesen. Channel plasmon-polariton guiding by subwavelength metal grooves. *Phys. Rev. Lett.*, 95(4):46802, 2005.

[66] D. F. P. Pile and D. K. Gramotnev. Channel plasmon-polariton in a triangular groove on a metal surface. *Opt. Lett.*, 29(10):1069–1071, 2004.

[67] J. Zhang, L. Cai, W. Bai, and G. Song. Hybrid waveguide-plasmon resonances in gold pillar arrays on top of a dielectric waveguide. *Opt. Lett.*, 35(20):3408–3410, 2010.

[68] F. Pincemin, AA Maradudin, AD Boardman, and J.J. Greffet. Scattering of a surface plasmon polariton by a surface defect. *Physical Review B*, 50(20):15261, 1994.

[69] F. Pincemin and J.J. Greffet. Propagation and localization of a surface plasmon polariton on a finite grating. *JOSA B*, 13(7):1499–1509, 1996.

[70] JA Sánchez-Gil. Surface defect scattering of surface plasmon polaritons: Mirrors and light emitters. *Appl. Phys. Lett.*, 73(24):3509–3511, 1998.

[71] P. Berini, R. Charbonneau, N. Lahoud, and G. Mattiussi. Characterization of long-range surface-plasmon-polariton waveguides. *J. Appl. Phys.*, 98:043109, 2005.

[72] R. Zia, A. Chandran, and M.L. Brongersma. Dielectric waveguide model for guided surface polaritons. *Opt. Lett.*, 30(12):1473–1475, 2005.

[73] R. Zia, J.A. Schuller, and M.L. Brongersma. Near-field characterization of guided polariton propagation and cutoff in surface plasmon waveguides. *Phys. Rev. B*, 74(16):165415, 2006.

[74] M. Hochberg, T. Baehr-Jones, C. Walker, and A. Scherer. Integrated plasmon and dielectric waveguides. *Opt. Express*, 12(22):5481–5486, 2004.

[75] A.V. Zayats, I.I. Smolyaninov, and A.A. Maradudin. Nano-optics of surface plasmon polaritons. *Phys. Rep.*, 408(3-4):131–314, 2005.

[76] J. Takahara, S. Yamagishi, H. Taki, A. Morimoto, and T. Kobayashi. Guiding of a one-dimensional optical beam with nanometer diameter. *Opt. Lett.*, 22(7):475–477, 1997.

[77] U. Schröter and A. Dereux. Surface plasmon polaritons on metal cylinders with dielectric core. *Phys. Rev. B*, 64(12):125420, 2001.

[78] J.L. Gervasoni. Dispersion relations for plasmon excitations in nanostructures of different shapes and symmetries. *Nucl. Instrum. Methods Phys. Res., Sect. B*, 267(2):235–238, 2009.

[79] J.K. Lim, K. Imura, T. Nagahara, S.K. Kim, and H. Okamoto. Imaging and dispersion relations of surface plasmon modes in silver nanorods by near-field spectroscopy. *Chem. Phys. Lett.*, 412(1-3):41–45, 2005.

[80] K. Imura, T. Nagahara, and H. Okamoto. Near-field optical imaging of plasmon modes in gold nanorods. *J. Chem. Phys.*, 122(15):154701, 2005.

[81] I. Puscasu, B. Monacelli, and G. Boreman. Plasmon dispersion relation of Au and Ag nanowires. *Phys. Rev. B*, 68(15):155427, 2003.

[82] E. Verhagen, M. Spasenović, A. Polman, and L. Kuipers. Nanowire plasmon excitation by adiabatic mode transformation. *Phys. Rev. Lett.*, 102(20):203904, 2009.

[83] M. Song, A. Bouhelier, P. Bramant, J. Sharma, E. Dujardin, D. Zhang, and G. Colas-des Francs. Imaging symmetry-selected corner plasmon modes in penta-twinned crystalline ag nanowires. *ACS Nano*, 5(7):5874–5880, 2011.

[84] J.P. Kottmann, O.J.F. Martin, D.R. Smith, and S. Schultz. Plasmon resonances of silver nanowires with a nonregular cross section. *Phys. Rev. B*, 64(23):235402, 2001.

[85] P. Bharadwaj, A. Bouhelier, and L. Novotny. Electrical excitation of surface plasmons. *Phys. Rev. Lett.*, 106(22):226802, 2011.

[86] M. Allione, V.V. Temnov, Y. Fedutik, U. Woggon, and M.V. Artemyev. Surface plasmon mediated interference phenomena in low-Q silver nanowirecavities. *Nano Lett.*, 8(1):31–35, 2008.

[87] E.J.R. Vesseur, R. De Waele, M. Kuttge, and A. Polman. Direct observation of plasmonic modes in au nanowires using high-resolution cathodoluminescence spectroscopy. *Nano Lett.*, 7(9):2843–2846, 2007.

[88] H. Ditlbacher, A. Hohenau, D. Wagner, U. Kreibig, M. Rogers, F. Hofer, F.R. Aussenegg, and J.R. Krenn. Silver nanowires as surface plasmon resonators. *Phys. Rev. Lett.*, 95(25):257403, 2005.

[89] N. Félidj, G. Laurent, J. Grand, J. Aubard, G. Lévi, A. Hohenau, F.R. Aussenegg, and J.R. Krenn. Far-field Raman imaging of short-wavelength particle plasmons on gold nanorods. *Plasmonics*, 1(1):35–39, 2006.

[90] M.W. Knight, N.K. Grady, R. Bardhan, F. Hao, P. Nordlander, and N.J. Halas. Nanoparticle-mediated coupling of light into a nanowire. *Nano Lett.*, 7(8):2346–2350, 2007.

[91] A.V. Akimov, A. Mukherjee, C.L. Yu, D.E. Chang, A.S. Zibrov, P.R. Hemmer, H. Park, and M.D. Lukin. Generation of single optical plasmons in metallic nanowires coupled to quantum dots. *Nature*, 450(7168):402–406, 2007.

[92] Z. Fang, L. Fan, C. Lin, D. Zhang, A.J. Meixner, and X. Zhu. Plasmonic coupling of bow tie antennas with ag nanowire. *Nano Lett.*, 11(4):1676–1680, 2011.

[93] G. I. Stegeman, R. F. Wallis, and A. A. Maradudin. Excitation of surface polaritons by end-fire coupling. *Opt. Lett.*, 8(7):386–388, 1983.

[94] J.C. Weeber, A. Dereux, C. Girard, J.R. Krenn, and J.P. Goudonnet. Plasmon polaritons of metallic nanowires for controlling submicron propagation of light. *Phys. Rev. B*, 60(12):9061–9068, 1999.

[95] A. Graff, D. Wagner, and U. Ditlbacher, H.and Kreibig. Silver nanowires. *Eur. Phys. J. D*, 34(1-3):263–269, 2005.

[96] A.W. Sanders, D.A. Routenberg, B.J. Wiley, Y. Xia, E.R. Dufresne, and M.A. Reed. Observation of plasmon propagation, redirection, and fan-out in silver nanowires. *Nano Lett.*, 6(8):1822–498, 2006.

[97] H. Staleva, S.E. Skrabalak, C.R. Carey, T. Kosel, Y. Xia, and G.V. Hartland. Coupling to light, and transport and dissipation of energy in silver nanowires. *Phys. Chem. Chem. Phys.*, 11(28):5889–5896, 2009.

[98] Z. Li, F. Hao, Y. Huang, Y. Fang, P. Nordlander, and H. Xu. Directional light emission from propagating surface plasmons of silver nanowires. *Nano Lett.*, 9(12):4383–4386, 2009.

[99] Q. Li, S. Wang, Y. Chen, M. Yan, L. Tong, and M. Qiu. Experimental demonstration of plasmon propagation, coupling, and splitting in silver nanowire at 1550-nm wavelength. *Selected Topics in Quantum Electronics, IEEE Journal of*, 17(4):1107–1111, 2011.

[100] D.E. Chang, A.S. Sørensen, P.R. Hemmer, and M.D. Lukin. Quantum optics with surface plasmons. *Phys. Rev. Lett.*, 97(5):053002, 2006.

[101] D.E. Chang, A.S. Sørensen, P.R. Hemmer, and M.D. Lukin. Strong coupling of single emitters to surface plasmons. *Phys. Rev. B*, 76(3):035420, 2007.

[102] Y. Fedutik, V. Temnov, U. Woggon, E. Ustinovich, and M. Artemyev. Exciton-plasmon interaction in a composite metal-insulator-semiconductor nanowire system. *J. Am. Chem. Soc.*, 129(48):14939–14945, 2007.

[103] H. Wei, D. Ratchford, X. Li, H. Xu, and C.K. Shih. Propagating surface plasmon induced photon emission from quantum dots. *Nano Lett.*, 9(12):4168–4171, 2009.

[104] Z. Fang, Y. Lu, L. Fan, C. Lin, and X. Zhu. Surface plasmon polariton enhancement in silver nanowire-nanoantenna structure. *Plasmonics*, 5(1):57–62, 2010.

[105] X. Guo, M. Qiu, J. Bao, B.J. Wiley, Q. Yang, X. Zhang, Y. Ma, H. Yu, and L. Tong. Direct coupling of plasmonic and photonic nanowires for hybrid nanophotonic components and circuits. *Nano Lett.*, 9(12):4515–4519, 2009.

[106] Y. Fang, Z. Li, Y. Huang, S. Zhang, P. Nordlander, N.J. Halas, and H. Xu. Branched silver nanowires as controllable plasmon routers. *Nano Lett.*, 10(5):1950–1954, 2010.

[107] R. Yan, P. Pausauskie, J. Huang, and P. Yang. Direct photonic-plasmonic coupling and routing in single nanowires. *PNAS.*, 106(50):21045–21050, 2009.

[108] C.H. Dong, X.F. Ren, R. Yang, J.Y. Duan, J.G. Guan, G.C. Guo, and G.P. Guo. Coupling of light from an optical fiber taper into silver nanowires. *Appl. Phys. Lett.*, 95(22):221109, 2009.

[109] R. Chikkaraddy, D. Singh, and G.V. Pavan Kumar. Plasmon assisted light propagation and raman scattering hot-spot in end-to-end coupled silver nanowire pairs. *Appl. Phys. Lett.*, 100(4):043108, 2012.

[110] T. Voss, G.T. Svacha, E. Mazur, S. Müller, C. Ronning, D. Konjhodzic, and F. Marlow. High-order waveguide modes in zno nanowires. *Nano Lett.*, 7(12):3675–3680, 2007.

[111] X.W. Chen, V. Sandoghdar, and M. Agio. Highly efficient interfacing of guided plasmons and photons in nanowires. *Nano Lett.*, 9(11):3756–3761, 2009.

[112] H. Wei, Z. Li, X. Tian, Z. Wang, F. Cong, N. Liu, S. Zhang, P. Nordlander, N.J. Halas, and H. Xu. Quantum dot-based local field imaging reveals plasmon-based interferometric logic in silver nanowire networks. *Nano Lett.*, 11(2):471–475, 2011.

[113] B. Hecht, H. Bielefeldt, L. Novotny, Y. Inouye, and D. W. Pohl. Local excitation, scattering, and interference of surface plasmons. *Phys. Rev. Lett.*, 77(9):1889–1892, 1996.

[114] A.C. Jones, R.L. Olmon, S.E. Skrabalak, B.J. Wiley, Y.N. Xia, and M.B. Raschke. Mid-IR plasmonics: Near-field imaging of coherent plasmon modes of silver nanowires. *Nano Lett.*, 9(7):2553–2558, 2009.

[115] J. Dorfmüller, R. Vogelgesang, W. Khunsin, C. Rockstuhl, C. Etrich, and K. Kern. Plasmonic nanowire antennas: Experiment, simulation, and theory. *Nano Lett.*, 10(9):3596–3603, 2010.

[116] P. Dawson, F. De Fornel, and J.P. Goudonnet. Imaging of surface plasmon propagation and edge interaction using a photon scanning tunneling microscope. *Phys. Rev. Lett.*, 72(18):2927–2930, 1994.

[117] L. Douillard, F. Charra, Z. Korczak, R. Bachelot, S. Kostcheev, G. Lerondel, P.M. Adam, and P. Royer. Short range plasmon resonators probed by photoemission electron microscopy. *Nano Lett.*, 8(3):935–940, 2008.

[118] D. Rossouw, M. Couillard, J. Vickery, E. Kumacheva, and G. A. Botton. Multipolar plasmonic resonances in silver nanowire antennas imaged with a subnanometer electron probe. *Nano Lett.*, 11(4):1499–1504, 2011.

[119] I. Alber, W. Sigle, S. Müller, R. Neumann, O. Picht, M. Rauber, P.A. van Aken, and M.E. Toimil-Molares. Visualization of multipolar longitudinal and transversal surface plasmon modes in nanowire dimers. *ACS Nano.*, 5(12):9845–9853, 2011.

[120] B. Guiton, V. Iberi, S. Li, D.N. Leonard, C.M. Parish, P.G. Kotula, M. Varela, G.C. Schatz, S.J. Pennycook, and J.P. Camden. Correlated optical measurements and plasmon mapping of silver nanorods. *Nano Lett.*, 11(8):3482–3488, 2011.

[121] B. Hecht, B. Sick, U.P. Wild, V. Deckert, R. Zenobi, O.J.F. Martin, and D.W. Pohl. Scanning near-field optical microscopy with aperture probes: Fundamentals and applications. *J. Chem. Phys.*, 112(18):7761, 2000.

[122] V.J. Sorger, Z. Ye, R.F. Oulton, Y. Wang, G. Bartal, X. Yin, and X. Zhang. Experimental demonstration of low-loss optical waveguiding at deep sub-wavelength scales. *Nat. Commun.*, 2:331, 2011.

[123] B. Wild, L. Cao, Y. Sun, B.P. Khanal, E.R. Zubarev, S.K. Gray, N.F. Scherer, and M. Pelton. Propagation lengths and group velocities of plasmons in chemically synthesized gold and silver nanowires. *ACS Nano*, 6(1):472–482, 2012.

[124] M.L. Juan, J. Plain, R. Bachelot, A. Vial, P. Royer, S.K. Gray, J.M. Montgomery, and G.P. Wiederrecht. Plasmonic electromagnetic hot spots temporally addressed by photoinduced molecular displacement. *J. Phys. Chem. A*, 113(16):4647–4651, 2009.

[125] A.L. Falk, F.H.L. Koppens, L.Y. Chun, K. Kang, N. de Leon Snapp, A.V. Akimov, M.H. Jo, M.D. Lukin, and H. Park. Near-field electrical detection of optical plasmons and single-plasmon sources. *Nat. Phys.*, 5(7):475–479, 2009.

[126] A. Merlen, F. Lagugné-Labarthet, and E. Harté. Surface-enhanced raman and fluorescence spectroscopy of dye molecules deposited on nanostructured gold surfaces. *J. Phys. Chem. C*, 2010.

[127] R. Dornhaus, R.E. Benner, R.K. Chang, and I. Chabay. Surface plasmon contribution to sers. *Sur.Sci.*, 101(1-3):367–373, 1980.

[128] X. Hong, D. Wang, and Y. Li. Kinked gold nanowires and their SPR/SERS properties. *Chem. Commun.*, 47(35):9909–9911, 2011.

[129] T. Shegai, Y. Huang, H. Xu, and M. Käll. Coloring fluorescence emission with silver nanowires. *Appl. Phys. Lett.*, 96(10):103114, 2010.

[130] H. Ditlbacher, J.R. Krenn, G. Schider, A. Leitner, and F.R. Aussenegg. Two-dimensional optics with surface plasmon polaritons. *Appl. Phys. Lett.*, 81(10):1762–1764, 2002.

[131] D. Solis Jr, W.S. Chang, B.P. Khanal, K. Bao, P. Nordlander, E.R. Zubarev, and S. Link. Bleach-imaged plasmon propagation (BlIPP) in single gold nanowires. *Nano Lett.*, 10(9):3482–3485, 2010.

[132] J.A. Hutchison, S.P. Centeno, H. Odaka, H. Fukumura, J. Hofkens, and H. Uji-i. Subdiffraction limited, remote excitation of surface enhanced raman scattering. *Nano Lett.*, 9(3):995–1001, 2009.

[133] Y. Fang, H. Wei, F. Hao, P. Nordlander, and H. Xu. Remote-excitation surface-enhanced raman scattering using propagating ag nanowire plasmons. *Nano Lett.*, 9(5):2049–2053, 2009.

[134] H. Wei and H. Xu. Nanowire-based plasmonic waveguides and devices for integrated nanophotonic circuits. *Nanophotonics*, pages 1–15, 2012.

[135] S. ENOCH and N. BONOD. *Plasmonics: from basics to advanced topics (hardback)(series: springer series in optical sciences)*. 2012.

[136] C. Deeb, X. Zhou, D. Gérard, A. Bouhelier, P.K. Jain, J. Plain, O. Soppera, P. Royer, and R. Bachelot. Off-resonant optical excitation of gold nanorods: Nanoscale imprint of polarization surface charge distribution. *J. Phys. Chem. Lett.*, 1:3539–3543, 2011.

[137] P. Neutens, P. Van Dorpe, I. De Vlaminck, L. Lagae, and G. Borghs. Electrical detection of confined gap plasmons in metal-insulator-metal waveguides. *Nat. Photonics*, 3(5):283–286, 2009.

[138] A. Drezet, A. Hohenau, D. Koller, A. Stepanov, H. Ditlbacher, B. Steinberger, F.R. Aussenegg, A. Leitner, and J.R. Krenn. Leakage radiation microscopy of surface plasmon polaritons. *Mater. Sci. Eng. B*, 149(3):220–229, 2008.

[139] A. Bouhelier, T. Huser, H. Tamaru, H.J. Güntherodt, DW Pohl, F.I. Baida, and D. Van Labeke. Plasmon optics of structured silver films. *Phys. Rev. B*, 63(15):155404, 2001.

[140] S.P. Frisbie, C.J. Regan, A. Krishnan, C. Chesnutt, J. Ajimo, A.A. Bernussi, and L. Grave de Peralta. Characterization of polarization states of surface plasmon polariton modes by fourier-plane leakage microscopy. *Opt. Commun.*, 283(24):5255–5260, 2010.

[141] C. Rewitz, T. Keitzl, P. Tuchscherer, J.S. Huang, P. Geisler, G. Razinskas, B. Hecht, and T. Brixner. Ultrafast plasmon propagation in nanowires characterized by far-field spectral interferometry. *Nano Lett.*, 12(1):45–49, 2012.

[142] Y. Fedutik, VV Temnov, O. Schöps, U. Woggon, and M.V. Artemyev. Exciton-plasmon-photon conversion in plasmonic nanostructures. *Phys. Rev. Lett.*, 99(13):136802, 2007.

[143] J. Dorfmüller, R. Vogelgesang, R.T. Weitz, C. Rockstuhl, C. Etrich, T. Pertsch, F. Lederer, and K. Kern. Fabry-pérot resonances in one-dimensional plasmonic nanostructures. *Nano Lett.*, 9(6):2372–2377, 2009.

[144] V.D. Miljković, T. Shegai, P. Johansson, and M. Käll. Simulating light scattering from supported plasmonic nanowires. *Opt. Express*, 20(10):10816–10826, 2012.

[145] T. Shegai, V.D. Miljković, K. Bao, H. Xu, P. Nordlander, P. Johansson, and M. Käll. Unidirectional broadband light emission from supported plasmonicnanowires. *Nano Lett.*, 11(2):706–711, 2011.

[146] W. Wang, Q. Yang, F. Fan, H. Xu, and Z.L. Wang. Light propagation in curved silver nanowire plasmonic waveguides. *Nano Lett.*, 11(4):1603–1608, 2011.

[147] M. Ambati, S.H. Nam, E. Ulin-Avila, D.A. Genov, G. Bartal, and X. Zhang. Observation of stimulated emission of surface plasmon polaritons. *Nano Lett.*, 8(11):3998–4001, 2008.

[148] J. Grandidier, G.C. des Francs, S. Massenot, A. Bouhelier, L. Markey, J.C. Weeber, C. Finot, and A. Dereux. Gain-assisted propagation in a plasmonic waveguide at telecom wavelength. *Nano Lett.*, 9(8):2935–2939, 2009.

[149] A. Manjavacas and F.J. García de Abajo. Robust plasmon waveguides in strongly interacting nanowire arrays. *Nano Lett.*, 9(4):1285–1289, 2009.

[150] P. Kusar, C. Gruber, A. Hohenau, and J.R. Krenn. Measurement and reduction of damping in plasmonic nanowires. *Nano Lett.*, 12(2):661–665, 2012.

[151] Z. Li, K. Bao, Y. Fang, Z. Guan, N.J. Halas, P. Nordlander, and H. Xu. Effect of a proximal substrate on plasmon propagation in silver nanowires. *Phys. Rev. B*, 82(24):241402, 2010.

[152] F.-W.; Xiao Y.-F.; Dong C.-H.; Chen X.-D.; Cui J.-M.; Gong Q.; Han Z.-F.; Guo G.-C. Zou, C.-L.; Sun. Plasmon modes of silver nanowire on a silica substrate. *Appl. Phys. Lett.*, 97(18):183102, 2010.

[153] Z. Li, K. Bao, Y. Fang, Y. Huang, P. Nordlander, and H. Xu. Correlation between incident and emission polarization in nanowire surface plasmon waveguides. *Nano Lett.*, 10(5):1831–1835, 2010.

[154] M.A. Noginov, V.A. Podolskiy, G. Zhu, M. Mayy, M. Bahoura, J.A. Adegoke, B.A. Ritzo, and K. Reynolds. Compensation of loss in propagating surface plasmon polariton by gain in adjacent dielectric medium. *Opt. Express*, 16(2):1385–1392, 2008.

[155] D. Handapangoda, M. Premaratne, I.D. Rukhlenko, and C. Jagadish. Optimal design of composite nanowires for extended reach of surface plasmon-polaritons. *Opt. Express*, 19(17):16058–16074, 2011.

[156] Z. Li, S. Zhang, N.J. Halas, P. Nordlander, and H. Xu. Coherent modulation of propagating plasmons in silver-nanowire-based structures. *Small*, 7(5):593–596, 2011.

[157] J.C. Ashley and L.C. Emerson. Dispersion relations for non-radiative surface plasmons on cylinders. *Surf. Sci.*, 41(2):615–618, 1974.

[158] J.P. Kottmann and O.J.F. Martin. Plasmon resonant coupling in metallic nanowires. *Opt. Express*, 8(12):655–663, 2001.

[159] Y. Sun, B. Mayers, T. Herricks, and Y. Xia. Polyol synthesis of uniform silver nanowires: a plausible growth mechanism and the supporting evidence. *Nano Lett.*, 3(7):955–960, 2003.

[160] J. Sharma, JP Vivek, and K.P. Vijayamohanan. Electron transfer behavior of monolayer protected nanoclusters and nanowires of silver and gold. *J. Nanosci. Nanotechnol.*, 6(11):3464–3469, 2006.

[161] A. Bouhelier, T. Huser, JM Freyland, H.J. Güntherodt, and DW Pohl. Plasmon transmissivity and reflectivity of narrow grooves in a silver film. *J. Microsc.*, 194(2-3):571–573, 1999.

[162] A. Bouhelier, R. Bachelot, G. Lerondel, S. Kostcheev, P. Royer, and G.P Wiederrecht. Surface plasmon characteristics of tunable photoluminescence in single gold nanorods. *Phys. Rev. Lett.*, 95(26):267405, 2005.

[163] S. Massenot, J. Grandidier, A. Bouhelier, G. Colas Des Francs, L. Markey, J.C. Weeber, A. Dereux, J. Renger, MU Gonzàlez, and R. Quidant. Polymer-metal waveguides characterization by fourier plane leakage radiation microscopy. *Appl. Phys. Lett.*, 91(24):243102–243102, 2007.

[164] J. Berthelot, A. Bouhelier, G.C. des Francs, J.C. Weeber, A. Dereux, et al. Excitation of a one-dimensional evanescent wave by conical edge diffraction of surface plasmon. *Opt. Express*, 19:5303–5312, 2011.

[165] E. Hecht. Optics (4th edn), 2002.

[166] J. Knopp and M.F. Becker. Virtual fourier transform as an analytical tool in fourier optics. *Appl. Opt.*, 17(11):1669–1670, 1978.

[167] L. Dai, I. Gregor, I. von der Hocht, T. Ruckstuhl, and J. Enderlein. Measuring large numerical apertures by imaging the angular distribution of radiation of fluorescing molecules. *Opt. Express*, 13:9409–9414, 2005.

[168] L. Novotny. Allowed and forbidden light in near-field optics. i. a single dipolar light source. *JOSA A*, 14(1):91–104, 1997.

[169] G.C. des Francs, J. Grandidier, S. Massenot, A. Bouhelier, J.C. Weeber, and A. Dereux. Integrated plasmonic waveguides: a mode solver based on density of states formulation. *Phys. Rev. B*, 80(11):115419, 2009.

[170] M. Burresi, RJP Engelen, A. Opheij, D. van Oosten, D. Mori, T. Baba, and L. Kuipers. Observation of polarization singularities at the nanoscale. *Phys. Rev. Lett.*, 102(3):33902, 2009.

[171] G. Colas des Francs, J.P. Hugonin, and J. Čtyrokỳ. Mode solvers for very thin long–range plasmonic waveguides. *Opt. Quantum. Electron.*, 42(8):557–570, 2011.

[172] SJ Al-Bader and HA Jamid. Diffraction of surface plasmon modes on abruptly terminated metallic nanowires. *Phys. Rev. B*, 76(23):235410, 2007.

[173] J. Gosciniak, S.I. Bozhevolnyi, T.B. Andersen, V.S. Volkov, J. Kjelstrup-Hansen, L. Markey, and A. Dereux. Thermo-optic control of dielectric-loaded plasmonic waveguide components. *Opt. Express*, 18(2):1207–1216, 2010.

[174] M.J. Dicken, L.A. Sweatlock, D. Pacifici, H.J. Lezec, K. Bhattacharya, and H.A. Atwater. Electrooptic modulation in thin film barium titanate plasmonic interferometers. *Nano Lett.*, 8(11):4048–4052, 2008.

[175] H. Dötsch, N. Bahlmann, O. Zhuromskyy, M. Hammer, L. Wilkens, R. Gerhardt, P. Hertel, and A.F. Popkov. Applications of magneto-optical waveguides in integrated optics: review. *JOSA B*, 22(1):240–253, 2005.

[176] C.X. Kan, J.J. Zhu, and X.G. Zhu. Silver nanostructures with well-controlled shapes: synthesis, characterization and growth mechanisms. *J. Phys. D: Appl. Phys.*, 41:155304, 2008.

[177] F. Kim, K. Sohn, J. Wu, and J. Huang. Chemical synthesis of gold nanowires in acidic solutions. *J. Am. Chem. Soc.*, 130(44):14442–14443, 2008.

[178] C. Durkan and ME Welland. Analysis of failure mechanisms in electrically stressed gold nanowires. *Ultramicroscopy*, 82(1):125–133, 2000.

[179] Q. Huang, C.M. Lilley, R. Divan, and M. Bode. Electrical failure analysis of Au nanowires. *Nanotechnology, IEEE Transactions on*, 7(6):688–692, 2008.

[180] B. Stahlmecke and G. Dumpich. Resistance behaviour and morphological changes during electromigration in gold wires. *Phys. Condens. Matter.*, 19:046210, 2007.

[181] R. Hoffmann, D. Weissenberger, J. Hawecker, and D. Stöffler. Conductance of gold nanojunctions thinned by electromigration. *Appl. Phys. Lett.*, 93(4):043118, 2008.

[182] J. Seidel, S. Grafström, L. Eng, and L. Bischoff. Surface plasmon transmission across narrow grooves in thin silver films. *Appl. Phys. Lett.*, 82:1368, 2003.

[183] J. Seidel, FI Baida, L. Bischoff, B. Guizal, S. Grafström, D. Van Labeke, and LM Eng. Coupling between surface plasmon modes on metal films. *Phys. Rev. B*, 69(12):121405, 2004.

[184] MR Kaspers, AM Bernhart, FJ Meyer zu Heringdorf, G. Dumpich, and R. Möller. Electromigration and potentiometry measurements of single-crystalline Ag nanowires under UHV conditions. *J. Phys. Condens. Matter*, 21:265601, 2009.

[185] KN Tu. Recent advances on electromigration in very-large-scale-integration of interconnects. *J. Appl. Phys*, 94:5451, 2003.

[186] C. Li, Y. Bando, and D. Golberg. Current imaging and electromigration-induced splitting of gan nanowires as revealed by conductive atomic force microscopy. *ACS nano*, 4(4):2422–2428, 2010.

[187] P. Xu, S.H. Jeon, H.T. Chen, H. Luo, G. Zou, Q. Jia, M. Anghel, C. Teuscher, D.J. Williams, and B. Zhang. Facile synthesis and electrical properties of silver wires through chemical reduction by polyaniline. *J. Phys. Chem. C*, 114:22147–22154, 2010.

[188] B. Stahlmecke and G. Dumpich. In situ observation of electromigration in gold nanowires. *Defect Diffus. Forum*, 1163:237–240, 2005.

[189] B. Stahlmecke, F.J.M. zu Heringdorf, LI Chelaru, M. Horn-von Hoegen, G. Dumpich, and KR Roos. Electromigration in self-organized single-crystalline silver nanowires. *Appl. Phys. Lett.*, 88:053122, 2006.

[190] Q. Huang, C.M. Lilley, M. Bode, and R. Divan. Surface and size effects on the electrical properties of Cu nanowires. *J. Appl. Phys.*, 104(2):023709–023709, 2008.

[191] T. Pinedo Rivera, O. Lecarme, J. Hartmann, E. Rossitto, K. Berton, and D. Peyrade. Assisted convective-capillary force assembly of gold colloids in a microfluidic cell: Plasmonic properties of deterministic nanostructures. *Journal of Vacuum Science & Technology B: Microelectronics and Nanometer Structures*, 26(6):2513–2519, 2008.

[192] T.P. Rivera, O. Lecarme, J. Hartmann, RL Inglebert, and D. Peyrade. Spectroscopic studies of plasmonic interactions in colloidal dimers fabricated by convective-capillary force assembly. *Microelectron. Eng.*, 86(4-6):1089–1092, 2009.

[193] O. Lecarme, T. Pinedo Rivera, L. Arbez, T. Honegger, K. Berton, and D. Peyrade. Colloidal optical waveguides with integrated local light sources built by capillary force assembly. *Journal of Vacuum Science & Technology B: Microelectronics and Nanometer Structures*, 28(6):C6O11–C6O15, 2010.

[194] E. Rossitto, O. Lecarme, L. Latu-Romain, K. Berton, T. Pinedo-Rivera, T. Jiu, P. Reiss, and D. Peyrade. Influence of optical excitation on the electric field assisted assembly of cdse nanorods. *Microelectron. Eng.*, 86(4-6):828–831, 2009.

[195] O. Lecarme, T. Pinedo-Rivera, K. Berton, J. Berthier, and D. Peyrade. Plasmonic coupling in nondipolar gold colloidal dimers. *Appl. Phys. Lett.*, 98(8):083122–083122, 2011.

[196] T.C. Isabell, P.E. Fischione, C. O'Keefe, M.U. Guruz, and V.P. Dravid. Plasma cleaning and its applications for electron microscopy. *Microsc. Microanal.*, 5(02):126–135, 1999.

[197] K.I. Schiffmann. Investigation of fabrication parameters for the electron-beam-induced deposition of contamination tips used in atomic force microscopy. *Nanotechnology*, 4:163, 1993.

[198] M. Antognozzi, A. Sentimenti, and U. Valdre. Fabrication of nano-tips by carbon contamination in a scanning electron microscope for use in scanning probe microscopy and field emission. *Microscopy Microanalysis Microstructures*, 8(6):355–368, 1997.

[199] SD Johnson, DG Hasko, KBK Teo, WI Milne, and H. Ahmed. Fabrication of carbon nanotips in a scanning electron microscope for use as electron field emission sources. *Microelectron. Eng.*, 61:665–670, 2002.

[200] T. Djenizian, L. Santinacci, H. Hildebrand, and P. Schmuki. Electron beam induced carbon deposition used as a negative resist for selective porous silicon formation. *Surf. Sci.*, 524(1):40–48, 2003.

[201] AJV Griffiths and T. Walther. Quantification of carbon contamination under electron beam irradiation in a scanning transmission electron microscope and its suppression by plasma cleaning. In *Journal of Physics: Conference Series*, volume 241, page 012017. IOP Publishing, 2010.

[202] K.L. Kelly, E. Coronado, L.L. Zhao, and G.C. Schatz. The optical properties of metal nanoparticles: The influence of size, shape, and dielectric environment. *J. Phys. Chem. B*, 107(3):668–677, 2003.

[203] A.D. McFarland and R.P. Van Duyne. Single silver nanoparticles as real-time optical sensors with zeptomole sensitivity. *Nano Lett.*, 3(8):1057–1062, 2003.

# List of publications

- *Imaging symmetry-selected corner plasmon modes in penta-twinned crystalline Ag nanowires,*
  Mingxia Song, Alexandre Bouhelier, Pierre Bramant, Jadab Sharma, Erik Dujardin, Douguo Zhang, and Gérard Colas-des-Francs. ACS Nano. 5, 5874 - 5880 (2011).

- *Silencing and enhancement of second-harmonic generation in optical gap antennas,*
  Johann Berthelot, Guillaume Bachelier, Mingxia Song, Padmnabh Rai, Gérard Colas-des-Francs, Alain Dereux, and Alexandre Bouhelier. Opt. Express 20, 10498 - 10508 (2012).

- *Limits of plasmonic circuitry: Synchronous recording of electron transport and plasmon propagation in crystalline metal nanowires,*
  Mingxia Song, Aniket Thete, Johann. Berthelot, Qiang Fu, Douguo Zhang, Gérard Colas-des-Francs, Erik Dujardin, and Alexandre Bouhelier. submitted.

  **In preparation:**

- *Selecting surface plasmon leaky and bound modes by polarization inhomogeneity,*
  Mingxia Song, Douguo Zhang, Stéphane Derom, Gérard Colas-des-Francs, Alexandre Bouhelier.

- *Effect of electron-beam exposure on surface plasmon resonance of metal nanoparticle,*
  Mingxia Song, Gérard Colas-des-Francs, Alexandre Bouhelier.